# EPITAXIAL GROWTH AND PROPERTIES OF ZNO THIN FILMS ON SI SUBSTRATES

**by**

**Wei Guo**

A dissertation submitted in partial fulfillment
of the requirements for the degree of
Doctor of Philosophy
(Materials Science and Engineering)
in The University of Michigan
2010

Doctoral Committee:

Professor Xiaoqing Pan, Chair
Associate Professor Jamie D. Phillips
Assistant Professor Anton Van der Ven
Adjunct Professor George W. Graham
Bing Liu, IMRA America, Inc.

粗茶有真味，
薄酒无醉人。
——林纾

© Wei Guo
2010

To my family with lots of Love.

# Acknowledgements

Much love to my parents **Changyu Guo** and **Jinjin Wei**, for their unconditional love and support throughout my life. My deepest love to you two!

Plenty of thanks to my advisor **Professor Xiaoqing Pan**, for his continuous support, mentoring, encouragement, and generosity. Thank you very much for a lot of critical advice and constantly reminding me to think scientifically and speak out loud.

My sincere gratitude to **Professor Jamie D. Phillips**, for being in my thesis committee, giving advice, and allowing me to use his instruments in collaborated projects.

I am also grateful to **Professor Anton Van der Ven**, for being in both of my prelim exam and thesis committee, encouraging me, and directing me.

**Dr. Bing Liu**- Thank a billion for your guidance in experiments and prudent advice to improve my understanding in a lot of scientific concepts. Thanks for the countless hours spent in reading my many drafts and reports.

**Professor George W. Graham**- Thank you for everything you did to make my graduate school experience a much better one. Thanks for your timely and critical reading of my research papers, fellowship essays, and this thesis.

**Professor Darrell G. Schlom**- Thank you for giving me the high quality bixbyite oxide films to assist my study. Also thank you for critical reading of my papers.

**Professor Wei Lu**- Thank you for giving me incisive comments on device testing experiments and a wonderful course about transistors.

**Dr. Yong Che**- Thanks a lot for your constant support and the opportunity you gave me to use some instruments at IMRA, Inc., which was critical for my research.

**Dr. Zhengdong Hu**- Thank you for your guidance and precious suggestions that helped me in many experiments.

**Dr. Arnold L. Allenic**- Tons of thanks for your guidance through a lot of experimental techniques, and you encouragement and care through all of these years. You are the best labmate and officemate I have ever had.

**Dr. Liqin Zhou**- Thanks for teaching me the techniques of powder pressing and target sintering, and being a great friend of mine.

**Dr. Yanbin Chen, Christopher T. Nelson, Michael B. Katz**, and **Yi Zhang**- Thank you all for spending countless hours preparing specimens and imaging by transmission electron microscopy. Many thanks for the beautiful images you contributed to this thesis. Special thank to Michael Katz for reading many of my drafts.

**Ying Qi, Dr. Haiping Sun, Dr. Kai Sun, Keith H. McIntyre, Justin W. Scanlon, Dr. Ovidiu F. Toader, Dr. Victor H. Rotberg**, **Dr. Fabian U. Naab,** and **John W. Mears**- Thank you all for being the greatest research specialists and/or technicians at the University of Michigan that students like me always turn for help.

**Obiefune K. Ezekoye, Kui Zhang, Xinhua Pan, Dr. Guang Ran, Dr. Hong Liu, Yanxia Liu, Tao Hang, Dr. Zhihua Li, Dr. Yingwen Duan, Baihai Li,** and **Won Woo Kim**- Thank you for doing research together with me and giving me the memorable life in and out of our labs.

**Dr. Wei Tian, Carolina Adamo**, and **Tassilo Heeg**- Thank you all for your assistance in collaborated projects with Professor Darrell G. Schlom.

**Dr. Guangyuan Zhao, Weiming Wang, Emine Cagin, Willie E. Bowen**, and **Meng Zhang**- Thank you all for sharing instruments, assisting experiments, and enjoying the journey of exploring ZnO with me.

**Dr. Qing Wan**, **Eric N. Dattoli,** and **Seok-Youl Choi**- Many thanks for your help in collaborated projects with Professor Wei Lu.

**Dr. Li Fu, Dr. Hongtao Cao, Lingyan Liang,** and **Zhimin Liu**- Thank you for all you did to assist me in the "stability of *p*-type SnO" project.

**Dr. Yuming Gao, Dr. Jose A. Azurdia, Dr. Qi Yang, Dr. Xiang Li, Dr. Qiangmin Wei, Yiying Zhao, Bingyuan Huang, Dr. Kwang-Hyup An, Abhishek Yadav,** and **Huarui Sun**- Thank you all for experimental assistance and discussions.

**Renee Hilgendorf, Jeanette L. Johnson, Debbie L. Johnson**, and **Nancy A. Polashak**- Thank you for administrative assistance though these years.

# Table of Contents

**Dedication** ..... ii

**Acknowledgements** ..... iii

**List of Tables** ..... viii

**List of Figures** ..... x

**List of Appendices** ..... xv

**Abstract** ..... xvi

**Chapter 1 Introduction** ..... 1

1.1 Advantages of ZnO ..... 1
1.2 Substrates for ZnO thin film growth ..... 2
1.3 Structures of ZnO ..... 3

**Chapter 2 Background and Literature Review** ..... 7

2.1 Direct growth of ZnO thin films on Si substrates ..... 7
2.1.1 (100) Si substrates ..... 7
2.1.2 (111) Si substrates ..... 10
2.2 ZnO growth on Si using buffer layers ..... 12
2.2.1 (100) Si with buffer layers ..... 12
2.2.2 (111) Si with buffer layers ..... 14
2.2.2.1 Single-crystalline ZnO thin films grown on (111) Si with buffer layers ..... 15
2.2.2.2 Strain and cracking of the single-crystalline ZnO thin films ..... 18
2.3 Summary and conclusions ..... 20

**Chapter 3 Experimental Techniques .................................................................. 36**

3.1 Pulsed laser deposition technique ........................................................................ 36
3.1.1 Dynamics of the PLD process ........................................................................ 36
3.1.2 The PLD systems ............................................................................................ 39
3.1.3 Substrate preparation for ZnO growth ............................................................ 41
3.1.4 Target preparation for ZnO growth ................................................................ 41
3.2 Structural characterization ................................................................................... 42
3.2.1 Film thickness measurement .......................................................................... 42
3.2.2 X-ray diffraction ............................................................................................. 43
3.2.2.1 $\theta$-$2\theta$ scan ......................................................................................... 43
3.2.2.2 $\omega$-scan ............................................................................................ 43
3.2.2.3 $\phi$-scan ............................................................................................. 44
3.2.2.4 Pole figure ...................................................................................... 45
3.2.2.5 Determination of tilt and twist angles and dislocation densities ..... 45
3.2.2.6 Determination of out-of-plane and in-plane strains ........................ 47
3.2.3 Atomic force microscopy ............................................................................... 48
3.2.4 Transmission electron microscopy ................................................................. 49
3.3 Composition characterization ............................................................................... 50
3.3.1 Secondary ion mass spectrometry .................................................................. 50
3.3.2 X-ray photoelectron spectroscopy .................................................................. 51
3.3.3 Rutherford backscattering spectrometry ........................................................ 51
3.4 Electrical characterization ..................................................................................... 52
3.4.1 Room temperature Hall effect measurement .................................................. 52
3.4.2 Temperature-dependent Hall effect measurement .......................................... 53
3.4.3 I-V characterization of junction samples ....................................................... 57
3.5 Optical characterization ........................................................................................ 57
3.5.1 Transmittance ................................................................................................. 57
3.5.2 Photoluminescence ......................................................................................... 57
3.5.3 Electroluminescence ....................................................................................... 60

**Chapter 4 Epitaxy and Properties of ZnO Thin Films Grown on (111) Si Using Bixbyite Oxide Buffer Layers ......................................................................... 72**

4.1 Properties of the bixbyite oxide buffer layers ....................................................... 72
4.2 Crystallinity of the epitaxial ZnO films grown on $M_2O_3$/Si ................................ 75
4.3 Microstructures and defects of the epitaxial ZnO films on $M_2O_3$/Si ................... 78
4.4 Surface morphologies of the epitaxial ZnO films on $M_2O_3$/Si ............................ 82
4.5 Electrical properties of the epitaxial ZnO films on $M_2O_3$/Si ............................... 84
4.6 Optical properties of the epitaxial ZnO films on $M_2O_3$/Si .................................. 88
4.6.1 Temperature-dependent PL measurements ..................................................... 88
4.6.2 Strain-related PL spectrum shift ..................................................................... 92
4.6.3 Electroluminescence from ZnO/$M_2O_3$/$p$-Si (111) heterostructures ............ 94
4.7 Summary and conclusions ...................................................................................... 96

**Chapter 5 Strain Engineering of Thick, Crack-free ZnO Films Grown on (111) Si Using Bixbyite Oxide Buffer Layers ............ 121**

5.1 Three structures of the ZnO films grown on $Gd_2O_3$/(111) Si ............ 121
5.2 Effect of the LT nucleation layer on dislocation reduction and strain relaxation ............ 122
5.3 Effect of the LT interlayer on further strain relaxation ............ 123
5.4 Defects introduced by the LT interlayer ............ 125

**Chapter 6 *P*-type Doping of ZnO Films with Antimony ............ 133**

6.1 Introduction to *p*-type doping of ZnO ............ 133
6.2 Sb-doped ZnO thin films grown on (0001) $Al_2O_3$ substrates ............ 135
6.3 Sb-doped ZnO thin films grown on Si substrates ............ 139

**Chapter 7 Thesis Conclusions ............ 152**

7.1 ZnO epitaxy on (111) Si using bixbyite oxide buffer layers ............ 152
7.2 Strain engineering of thick, crack-free ZnO films ............ 153
7.3 *P*-type doping of ZnO thin films with antimony ............ 153
7.4 Impact of this work ............ 154

**Chapter 8 Future Work Recommendations ............ 155**

8.1 Improving NBE emissions in the heterojunction devices on Si ............ 155
8.2 Exploring high quality ZnO homojunctions grown on Si ............ 156
8.3 Exploring different functionalities of the single-crystalline ZnO films on Si ... 157

**Appendix A High resolution XRD measurements and analyses ............ 158**

**Appendix B Temperature-dependent Hall effect fittings ............ 162**

**Bibliography ............ 165**

# List of Tables


Table 2.1 Buffer layers reported to yield single-crystalline ZnO growth on (111) Si, together with a comparison of lattice misfits, growth techniques employed, ZnO film thicknesses, FWHMs of $(0002)_{ZnO}$ $\omega$-rocking curves, and experimental techniques employed in proving the epitaxy........................................................................... 22

Table 2.2 Linear thermal expansion coefficients at 300 K for Si, ZnO, and some buffer layer materials, listed in increasing order. Note that the data of $\gamma$-$Al_2O_3$ is a volume expansion coefficient. ........................................................................................ 23

Table 3.1 Substrates and targets used in my study for ZnO growth. ................................ 61

Table 4.1 Enthalpy of formation ($\Delta_f H°$), lattice constants ($a_{latt}$), and internal parameters ($u$, $x$, $y$, and $z$) of the bixbyite oxides........................................................................... 98

Table 4.2 Comparison of tilt ($\alpha_\Omega$) and twist ($\alpha_\Phi$) angles and dislocation densities ($N_c$ and $N_a$) of ~1 μm thick ZnO films grown under the same growth conditions. ....................... 99

Table 4.3 Comparison of RT electrical properties of ZnO films grown at 600 °C on different buffer layers/substrates under the same growth conditions. ........................... 100

Table 4.4 Fitting parameters used in the CBE simulations and mobility fittings for the corrected electrical data in Figure 4.12......................................................................... 101

Table 4.5 Comparison of PL exciton peak energies of the ZnO films grown on $M_2O_3$/Si with the energies of a ZnO single crystal and those reported in references. .................. 102

Table 5.1 Comparison of FWHM values of the 0002 and $10\bar{1}2$ ZnO $\omega$-rocking curves, dislocation densities ($N_c$ and $N_a$), and compressive strain along $c$-axis ($\varepsilon_{zz}$) of crack-free ZnO films grown on $Gd_2O_3$/Si with the three structures. .............................................. 127

Table 6.1 Electrical properties at RT of undoped ZnO, 0.1 at.% and 1.0 at.% Sb-doped ZnO films grown on (0001) $Al_2O_3$........................................................................... 140

Table 6.2 Tilt, twist angles and calculated $c$- and $a$-type threading dislocation densities for 400 nm thick undoped, 0.1 at.% and 1.0 at.% Sb-doped ZnO films grown on (0001) $Al_2O_3$ at 600 °C.......................................................................................................... 141

Table 6.3 Comparison of electrical properties at room temperature of 0.1 at.% Sb-doped ZnO films grown on (100) Si and (111)Si with $Sc_2O_3$ buffer layer................................ 142

# List of Figures


Figure 1.1 The exciton binding energy ( $E_x^b$ ) as a function of the band gap ($E_g$) for various direct gap semiconductors (from Ref. [23 Semiconductor Optics, by Klingshirn]) .......... 5

Figure 1.2 Schematics using the ball-and-stick model show (a) the wurtzite ZnO structure (O-polar) and the construction of hcp sublattice, and the ZnO lattice viewed from directions of $[11\bar{2}0]$ (b), $[01\bar{1}0]$ (c), and [0001] (d). .......... 6

Figure 2.1 (a) Pole figure of ZnO $\{10\bar{1}1\}$ planes for the films grown on (100) Si at 500 °C. (b) Pole figure of ZnO $\{10\bar{1}2\}$ planes for the films grown on (100) Si at 750 °C. (from Han *et al*. [42] and Liu *et al*. [54]) .......... 24

Figure 2.2 Cross-sectional TEM images of ZnO directly grown on (100) Si. (from Tan *et al*. [37] and Han *et al.* [42]) .......... 25

Figure 2.3 (a) I-V characteristics and schematic diagram of the *i*-$Mg_xZn_{1-x}O$/*n*-ZnO/$SiO_x$/$n^+$-(100) Si structure. (b) RT EL spectra under different forward current injections. (from Chen *et al*. [66]) .......... 26

Figure 2.4 RT PL and EL spectra under different current injections for (a) *n*-ZnO/$SiO_x$/*n*-(100)Si, and (b) *n*-ZnO/$SiO_x$/*p*-(100) Si structures when Si is positive biased. (from Tan *et al*. [37]) .......... 27

Figure 2.5 RHEED patterns and RT PL spectra of the ZnO thin films grown at 650 °C on (111) Si substrates in vacuum ((a) and (c)) and oxygen ambient ((b) and (d)), respectively. (from Zhao *et al*. [74]) .......... 28

Figure 2.6 XRD $\theta$-$2\theta$ scans and rocking curves of ZnO films deposited on (100) Si, (a) without Zn buffer layer, (b) with Zn buffer layer, and (c) with Zn buffer layer and annealed at 800 °C for 1h. (from Fu *et al*. [78]) .......... 29

Figure 2.7 Comparison of RT cathodoluminescence spectra of annealed samples deposited on (a) (100) Si with Zn buffer layer, (b) (111) Si with Zn buffer layer, and (c) (100) Si without Zn buffer layer. (from Fu *et al*. [78]) .......... 30

Figure 2.8 RT EL spectra (a), and plane view (b) and cross-sectional (c) SEM images of ZnO *p-n* junction on MgO buffered (100) Si. (from Kong *et al*. [87]) .......... 31

Figure 2.9 (a) XRD $\theta$-$2\theta$ scan of a ZnO/AlN/(111) Si film with inset showing $\omega$-rocking curves of the $0002_{ZnO}$ and $10\bar{1}2_{ZnO}$ reflections, respectively. (b) XRD reciprocal space mapping of asymmetrical $(20\bar{2}4)$ reflection of a ZnO/GaN/(111) Si film. (from Jiang *et al*. [115] and Oleynik *et al*. [94], respectively) ... 32

Figure 2.10 (a) XRD $\theta$-$2\theta$ and $\omega$-scans of a ZnO/ZnS/(111) Si film grown by PLD. (b) $\phi$-scans showing in-plane symmetries and orientation relationship. (c) and (c') RHEED patterns of a ZnO/ZnS/(111) Si film grown by electron-beam evaporation. The RHEED beam direction is $[11\bar{2}0]$ for (c) and $[10\bar{1}0]$ for (c'), respectively. ((a) and (b) are from Yoo *et al*. [70]; (c) and (c') are from Miyake *et al*. [96]) ... 33

Figure 2.11 (a) Cross-sectional TEM image of a ZnO/$Y_2O_3$/(111) Si film. (b) HRTEM image of the ZnO/$Y_2O_3$ interface. (c) Fourier filtered image of the selected area in (b). (d) $\phi$-scans shows twin structure in the $Y_2O_3$ layer. (from Liu *et al*. [111]) ... 34

Figure 2.12 (a) Microscopic image showing cracked surface of ZnO/LT-ZnO/oxidized Zn/(111) Si grown by MBE. (b) Schematic of stress-strian relationship. (c) Relationships between the lattice and thermal mismatches, the strain in the film, and the curvature of the film surface. (from Kawamoto *et al*. [112] and Krost *et al*. [123], respectively) ... 35

Figure 3.1 Schematic of a typical PLD system ... 62

Figure 3.2 Schematics showing (a) the four dynamic processes of laser-plasma-solid interactions in PLD technique, and (b) a close look of the interactions between the plasma plume and the laser radiation. ... 63

Figure 3.3 Photographs of (a) the excimer laser, (b) the Neocera PLD system, (c) the plasma plume, and (d) the Thermionics PLD system. ... 64

Figure 3.4 Calibration of the substrate temperature vs. the heater temperature in the Thermionics system. ... 65

Figure 3.5 Schematic showing the relationship between the diffractometer axes and the substrate reference frame in XRD measurement. (modified from V. Srikant *et al.* [142]) ... 66

Figure 3.6 Schematics showing (a) symmetric, (b) skew symmetric, and (c) glancing incidence asymmetric XRD geometries used to measure the $\omega$-scans of ZnO 0002 and $10\bar{1}2$ and the $\phi$-scan of ZnO $11\bar{2}4$ reflections, respectively. ... 67

Figure 3.7 Pole figure of ZnO grown on (111) Si with bixbyite oxide buffer layer. ... 68

Figure 3.8 SIMS depth profile of impurities in a commercial ZnO target. ... 69

Figure 3.9 Commonly used Van der Pauw configurations of Hall effect measurements. (from NIST [[151]]) The configuration used in this study is (b). ... 70

Figure 3.10 Schematic of the PL system setup (not drawn to scale) ................................ 71

Figure 4.1 (a) Unit cell of the $M_2O_3$ lattice. Green spheres indicate *M* (Sc, Lu, Y, Gd) atoms, red spheres oxygen. (b) Atomic arrangements of (111) Si (i), (111) $M_2O_3$ (ii), and (0001) ZnO (iii). (from Guo *et al*. [108])........................................................... 103

Figure 4.2 XRD $\phi$-scans (on a log scale) of $Sc_2O_3$, $Lu_2O_3$, and $Gd_2O_3$ 211 peaks, and Si 220 peaks. .............................................................................................................. 104

Figure 4.3 (a) HRTEM image of $Sc_2O_3$ film grown on (111) Si. (b) The area marked in (a) under larger magnification. ................................................................................... 105

Figure 4.4 (a) XRD $\theta$-$2\theta$ scans (on a log scale) of the ZnO films grown on $Sc_2O_3$/Si (red), $Lu_2O_3$/Si (black), and $Gd_2O_3$/Si (blue). (b) Enlarged $\theta$-$2\theta$ scans show interference fringes on the $M_2O_3$ 222 peaks. (c) Representative XRD $\phi$-scans (on a log scale) of ZnO $11\bar{2}4$ (black) and Si 440 (blue) peaks from ZnO/$M_2O_3$/Si films............................................ 106

Figure 4.5 (a) XRD $\omega$-scans of ZnO 0002 and $10\bar{1}2$ reflections of a ZnO film grown on 100 nm $Sc_2O_3$/(111) Si. (b) Comparison of the $\omega$-FWHM values of ZnO 0002 and $10\bar{1}2$ reflections reported for several films in Table 2.1. The values of a ZnO/*c*-$Al_2O_3$ film grown by the same PLD system are also included. (c) Williamson-Hall plot of ZnO 0001 series of reflections measured from the ZnO/100 nm $Sc_2O_3$/Si film. (d) Plot of $\omega$-FWHM values of ZnO 0002 and off-axis reflections with Srikant method fitting.. .................. 107

Figure 4.6 (a) Typical cross-sectional TEM image of a ZnO/$M_2O_3$/(111) Si film. The $M_2O_3$ layer in this specimen is a 30 nm thick $Lu_2O_3$ layer. (b) Cross-sectional dark field image of the same area with **g**=$10\bar{1}2$. (c) SAED pattern of the interface region under the zone axis of $[1\bar{2}10]_{ZnO}$ ($[1\bar{1}0]_{Si}$). (d) Simulated SAED pattern revealing the overlapping of Si (blue dots), $M_2O_3$ (yellow dots), and ZnO (red dots) patterns. (e) HRTEM image of the ZnO/ $M_2O_3$ interface. .................................................................................. 108

Figure 4.7 (a) HRTEM image taken along zone axis $[11\bar{2}0]$ showing a pair of Frank partial dislocation surrounds a short segment of type $I_1$ stacking fault. (b) and (c) are the corresponding FFT pattern and iFFT image respectively. (d) A Burgers circuit surrounding one of the end-on Frank partial dislocations, indicating a Burgers vector of **b**=**AB**=$\frac{1}{6}\langle 20\bar{2}3\rangle$. (e) A ball-and-stick model simulation of a plane insertion. ............. 109

Figure 4.8 (a) HRTEM image (zone axis $[11\bar{2}0]$) of type $I_1$ stacking fault formed by removing one (0001) plane and displacing half crystal by $\frac{1}{3}\langle 10\bar{1}0\rangle$ in the vicinity of an APB. (b) A ball-and-stick model simulation of the stacking fault. ................................ 110

Figure 4.9 $C_S$-corrected HAADF STEM images of the $M_2O_3$/Si interface (a) after the growth and (b) before the growth of ZnO film, respectively......................................... 111

Figure 4.10 AFM images of (a) 30 nm thick $Lu_2O_3$ film grown on (111) Si, (b) 600 nm thick ZnO film grown on the $Lu_2O_3$/Si substrate without the nu-ZnO layer, (c) 800 nm thick ZnO film grow on $Lu_2O_3$/Si with the nu-ZnO layer, and (d) finer scan of the enlarged area marked in (c)........................................................................................ 112

Figure 4.11 Optical microscopic image of a 800 nm thick ZnO film grown on $Lu_2O_3$/Si, showing surface cracks along $<1\bar{2}10>_{ZnO}$ with a density of ~40 $cm^{-1}$.......................... 113

Figure 4.12 Temperature dependence of electron concentrations [(a), (b), (c)] and Hall mobilities [(d), (e), (f)] of ZnO films grown on $M_2O_3$/Si substrates.............................. 114

Figure 4.13 Schematic band diagram (drawn to scale) of the ZnO/30 nm $Sc_2O_3/(SiO_x)$Si sample, indicating band down-bending at the ZnO/$Sc_2O_3$ interface.............................. 115

Figure 4.14 (a) Comparison of 10 K PL spectra of a (0001) ZnO single crystal (black line) with those of the ZnO films grown on $M_2O_3$/(111) Si substrates (color lines). (b) Temperature-dependent NBE spectra from 10 K to 300 K of ZnO/$Sc_2O_3$/Si................ 116

Figure 4.15 Comparison of 10 K NBE spectra of the ZnO single crystal, ZnO film grown on *c*-$Al_2O_3$, and ZnO films grown on $M_2O_3$/Si [(1)-(3)]. Spectra are in log scale and vertically displaced for clarity. ........................................................................... 117

Figure 4.16 Typical SIMS depth profiles of impurities in ZnO/$M_2O_3$/Si thin films....... 118

Figure 4.17 (a) High resolution $\theta$-$2\theta$ XRD scans on a ZnO/$Sc_2O_3$/Si film of ZnO 0002 and $10\bar{1}3$ reflections with respect to Si 111 and 113 reflections, respectively. (b) Exciton energies of free A exciton ($A_L^{n=1}$) and neutral Al donor bound exciton ($I_6$) as a function of the in-plane biaxial strain in ZnO/$M_2O_3$/Si films........................................................ 119

Figure 4.18 (a) I-V characteristics of the ZnO/$Gd_2O_3$/*p*-Si heterostructure. The inset is a schematic diagram of the device under forward bias. (b) EL spectra measured at room temperature from the device operated at different forward currents, showing a weak ZnO NBE emission. ..................................................................................................... 120

Figure 5.1 Structural schematics of the three ZnO film structures studied in this chapter (not drawn to scale): (*a*) HT ZnO film, (*b*) HT ZnO film grown on a 10 nm LT nucleation ZnO layer, (*c*) HT ZnO film grown on the nucleation layer and inserted with two 10 nm LT ZnO interlayers. ................................................................................................ 128

Figure 5.2 Cross-sectional bright field TEM images of the ZnO films on $Gd_2O_3$/Si with (a) structure *b* and (b) structure *c*. ........................................................................... 129

Figure 5.3 Schematic showing the dislocations and residual strain after post-growth cooling in the three ZnO films (not drawn to scale). The tensile strain intensify is denoted by different colors from high (H, red) to low (L, blue). ............................................... 130

Figure 5.4 (a) Cross-sectional bright field TEM image of the interfacial region containing the LT nucleation layer. Cross-sectional dark field images of the film with structure *c*, with **g**=0002 in (b) and **g**= $20\bar{2}0$ in (c), respectively. .................................................... 131

Figure 5.5 Cross-sectional dark field TEM images of a local region of structure *c* using different **g** of 0002 (a), $20\bar{2}0$ (b), and $10\bar{1}2$ (c), respectively. (d) is a corresponding schematic diagram, in which the orange lines are visible in (a) and the blue lines are shown in (b). (e) is an HRTEM image showing a long segment of stacking faults in the LT interlayer. ............................................................................................................ 132

Figure 6.1 Schematic of formation energies of charged defects vs. the Fermi energy position of wide band gap semiconductors. (from Yan and Wei [217]) ........................ 143

Figure 6.2 RBS spectra of the Sb-doped ZnO films on $Al_2O_3$ substrates. The Sb concentrations are estimated about 1.0 at.% and 0.1 at.% for the films grown with 1 at.% and 0.2 at.% Sb-doped ZnO targets, respectively. ......................................................... 144

Figure 6.3 Typical XRD $\theta$-$2\theta$ (a) and $11\bar{2}4$ $\phi$ (b) scans of 1.0 at.% Sb-doped ZnO films grown at 600 °C. ............................................................................................... 145

Figure 6.4 Optical transmittance spectra and Tauc plots (inset) of undoped ZnO, 0.1 at.% and 1.0 at.% Sb-doped ZnO films. ..................................................................... 146

Figure 6.5 Temperature dependence of the hole concentration for 1.0 at.% Sb-doped ZnO films grown at 400 °C. ............................................................................................... 147

Figure 6.6 Cross-sectional TEM image of (a) undoped ZnO and (b) 1.0 at.% Sb-dope films. High resolution TEM images ((c) and (d)) of 1.0 at% Sb-ZnO film showing partial dislocations associated with stacking faults. The Burgers vector is $\frac{1}{6}[02\bar{2}\bar{3}]$. .............. 148

Figure 6.7 AFM images of 0.1 at.% Sb-doped films grown at (a) 400 °C and (b) 600 °C, and 1.0 at.% Sb-doped films grown at (c) 400 °C and (d) 600 °C. ............................... 149

Figure 6.8 Typical XPS spectrum showing Sb-O bonding in 1.0 at.% Sb-doped ZnO films on $Al_2O_3$. ............................................................................................................ 150

Figure 6.9 Typical temperature-dependent PL spectra of 0.1 at.% Sb-doped films grown at 600 °C on $Al_2O_3$. ...................................................................................................... 151

# List of Appendices

**Appendix A High resolution XRD measurements and analyses .............................. 158**

A.1 Skew symmetric $\omega$-scan ........................................................................ 158
A.2 $\phi$-scan in the glancing incidence geometry..................................................... 159
A.3 Determination of the twist angle...................................................................... 160

**Appendix B Temperature-dependent Hall effect fittings.......................................... 162**

B.1 Three-band CBE simulation of $n(T)$ ................................................................ 162
B.2 Matthiessen's rule simulation of $\mu(T)$ ............................................................. 163

# Abstract

**Epitaxial Growth and Properties of ZnO Thin Films on Si Substrates**

by

Wei Guo

Chair: Xiaoqing Pan

ZnO is an attractive material for promising applications in short wavelength optoelectronic devices because of its wide band gap and large exciton binding energy at room temperature (RT). This dissertation is devoted to the development of high quality, single-crystalline ZnO-based light-emitting devices on Si substrates, involving thin film synthesis by pulsed laser deposition, structure-property characterization, prototype device fabrication, strain engineering of thick films, and *p*-type doping with antimony (Sb).

ZnO epitaxy with exceptional quality was achieved on (111) Si substrates for the advantages of inexpensive large wafers, mature device technologies, and multifunctional device integration. Epitaxial bixbyite oxides $M_2O_3$ ($M$=Sc, Lu, Gd) were originally employed as the buffer layer between ZnO and Si. The single-crystalline ZnO films has superior structural, electrical, and optical qualities than all previous reports of ZnO on Si, such as narrow $\omega$-rocking curves, low dislocation densities, high electron mobilities at RT, and comparable photoluminescence characteristics to those of ZnO single crystal. The epitaxial orientation relationship, intrinsic donors, microstructural defects, and residual strain of the films were investigated. Prototype $n$-ZnO/$M_2O_3$/$p$-Si devices were constructed, and ZnO near-band-edge emission was observed in electroluminescence at RT. Strain engineering of thick films by insertion of low-temperature grown ZnO interlayers was performed to improve the cracking critical thickness to $\geq 2$ μm.

Reliable ZnO *p*-type doping using large-size-mismatched Sb dopant was achieved for the films grown on both (0001) $Al_2O_3$ and (100) Si substrates, with a resistivity of 4.2-60 Ω cm, a Hall mobility of 0.5-7.7 $cm^2/V$ s, and a hole concentration of $3.2\times10^{16}$-$2.2\times10^{17}$ $cm^{-3}$. The origin of *p*-type conductivity was elucidated from conjugated effects of oxygen-rich growth condition, adequate doping concentration, and dislocation-facilitated formation of complex acceptors of $Sb_{Zn}$-$2V_{Zn}$. The thermal activation energy and the optical ionization energy of the acceptor are estimated 115±5 meV and 158±7 meV, respectively.

# Chapter 1

# Introduction

## 1.1 Advantages of ZnO

Zinc oxide (ZnO) is a II-VI transparent conducting oxide that has been extensively studied for its promising applications in solar cells,[1] transducers,[2] varistors,[3] optical waveguides,[4] and gas sensors.[5] In the past decades, ZnO, with its wide band gap of 3.37 eV, was identified as an attractive competitor with GaN in short-wavelength optoelectronic devices, such as blue and ultraviolet (UV) light emitters and laser diodes,[6,7] primarily because of its larger exciton binding energy (59 meV versus 30 meV of GaN), which suggests that brighter light emission can be achieved at lower threshold at above room temperature. Figure 1.1 compares the exciton binding energies and band gaps of various direct gap semiconductors.

Besides its attractive optical properties, ZnO has notable electrical properties including high electron mobility,[8] breakdown strength, and electron drift velocity.[9] Some physical properties, such as resistance to mechanical stress and high melting temperature, make ZnO promising for the fabrication of long lifetime devices. The possibility of high quality epitaxial ZnO growth, together with the commercial availability of bulk ZnO single crystals, should substantially reduce the cost of ZnO-based optoelectronic devices relative to GaN. Furthermore, ZnO shows radiation hardness, which is required for special applications such as use in space environment.[10]

### 1.2 Substrates for ZnO thin film growth

Since most optoelectronic devices require epitaxial films, the epitaxial growth of ZnO thin films has been examined using a variety of growth techniques on many substrates. Ideally, coherent epitaxial ZnO growth would be performed on a ZnO substrate, but unfortunately, commercially available ZnO substrates are presently extremely expensive and have variable quality and impurity levels due to immature manufacturing technology.

The most widely used substrate for ZnO heteroepitaxy is (0001) $Al_2O_3$ ($c$-$Al_2O_3$). Although $Al_2O_3$ (sapphire) is available in large format wafers, it has a large lattice mismatch (18.4%) with ZnO, which induces defects such as threading dislocations and stacking faults in the ZnO film, thereby degrading the film quality. In order to reduce the defect density, a small lattice-mismatched (1.8%) buffer layer of GaN[11] has been inserted between ZnO and $Al_2O_3$, and nearly lattice-matched InGaN[12] buffer layer (0%) and $ScAlMgO_4$[6,13] substrate (0.09%) have also been developed for ZnO growth. Although exciting results of ZnO-based light emitting devices (LEDs) have been achieved on $ScAlMgO_4$,[6] neither of these lattice-matched substrates are universally accessible. Other substrates or intervening buffer layers have also been tried for ZnO heteroepitaxy, including (0001) SiC (lattice mismatch: 5%),[14] (001) $LiAlO_2$ (3%),[15] and (111)-oriented cubic materials such as YSZ (10.6%),[16] GaAs (18.7%),[17] and MgO (9%)[18] buffered $Al_2O_3$. Due to the lack of knowledge and development of these unconventional substrates/buffer layers, none of them have been widely utilized for ZnO growth.

Si is actually the second most widely used substrate for ZnO growth, in spite of a number of advantages it has over the other substrates, notably its low cost, availability as large-scale wafers, compatibility with mature device technologies, and high electrical and thermal conductivities. The most important of these is certainly that it brings the possibility of integrating ZnO-based multifunctional devices with advanced Si-based IC technology, as foreseen by K. Wasa *et al.*[19], who made the first $n$-ZnO/$p$-Si heterojunction diode in 1971. Significant obstacles exist, however, such as the difficulty of achieving reliable $p$-type doping of ZnO and the problem of large lattice and thermal mismatches between ZnO and Si. Nevertheless, research on ZnO growth on Si has continued exponentially, particularly concerning the fabrication of ZnO on (100) and

(111) Si substrates in structures such as thin films, nanorods, or quantum structures, using various buffer layers methods and doping techniques. Such work has also been demonstrated as prototype devices such as light-emitting diodes and transistors. However, most of the ZnO thin films that have been grown on Si are polycrystalline due to the lattice mismatch and the inherent reactivity between ZnO and Si.[20] Recently, there has been a surge of interest in growing high quality epitaxial ZnO thin films on Si substrates, with the hope of developing ZnO-based optoelectronic devices with Si electronics. In my PhD work, I have achieved single-crystalline ZnO films on (111) Si substrates with superior quality than all previous reports of ZnO on Si.

## 1.3 Structures of ZnO

ZnO, like most binary II-VI oxide materials, is thermodynamically stable in the wurtzite structure (space group $P6_3mc$, #186), with hexagonal close packed (hcp) double layers of Zn and O atoms, as shown in Figure 1.2(a). It can also crystallize in the cubic zincblende structure (space group $F\overline{4}3m$, #216) under high pressure or certain metastable growth conditions.[21]

In the wurtzite structure, the ideal stacking sequence repeats as AaBbAaBb…, as shown in Figure 1.2(a), where the upper and lower cases of letters denote the Zn and O layers, respectively. Figure 1.2(a) further illustrates the construction of hcp sublattice from the wurtzite structure. The wurtzite structure lacks the symmetry of center of inversion, leading to the piezoelectric property of ZnO. The lattice polarity is Zn polar when O→Zn bond is along [0001], or O-polar if it is along $[000\overline{1}]$. The lattice constants of ZnO are $c_0$=5.2042 Å and $a_0$= 3.2496 Å.[22] Figures 1.2(b)-(d) show the O-polar ZnO lattice, constructed of 18 primitive unit cells (3×3×2), from three different perspectives, along the $[11\overline{2}0]$, $[01\overline{1}0]$, and [0001] directions of ZnO.

With all this in view, the objectives of this thesis are: (1) to synthesize high quality epitaxial ZnO thin films on Si substrates, compatible with multifunctional device integration; (2) to optimize the structural and optoelectronic properties of the ZnO films through systematic studies; (3) to understand the defect mechanisms and structure-

properties relationships in ZnO films by characterizing the film microstructures; (4) to explore prototype light-emitting devices based on the heterojunction structures of ZnO films on (111) Si; and (5) to examine the feasibility of ZnO *p*-type doping through large-size-mismatched elements such as antimony.

The outline of this thesis is to first, provide a comprehensive review of all previous work of ZnO thin films grown on Si substrates, including the direct growth of ZnO on both (100) and (111) Si, and all the buffer layers, passivation layers, and/or nucleation layers that have been used to improve the ZnO film quality. In particular, a detailed citation of work on single-crystalline ZnO films achieved on (111) Si substrates with different buffer layers is summarized. This review and summary is contained in Chapter 2. Chapter 3 then deals with the experimental techniques employed in this work. Chapter 4 is focused on the synthesis of epitaxial ZnO films on (111) Si using bixbyite oxide buffer layers including $Sc_2O_3$, $Lu_2O_3$, and $Gd_2O_3$. The advantages of employing bixbyite oxide buffer layers are discussed. The structural, electrical, and optical properties of the single-crystalline ZnO films are investigated in detail. Chapter 6 presents the synthesis and properties of *p*-type epitaxial ZnO films by antimony doping. Finally, the thesis ends with a brief conclusion and summary of Chapter 7, and possible future work is proposed in Chapter 8.

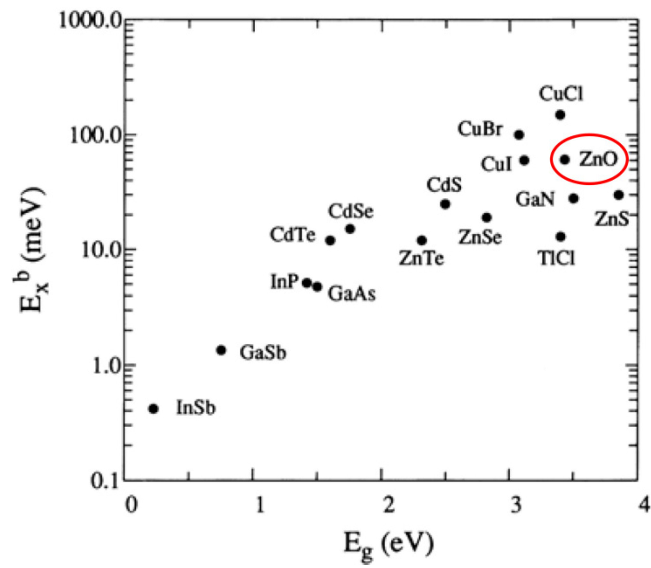


Figure 1.1 The exciton binding energy ( $E_x^b$ ) as a function of the band gap ($E_g$) for various direct gap semiconductors (from Ref. [23 Semiconductor Optics, by Klingshirn])

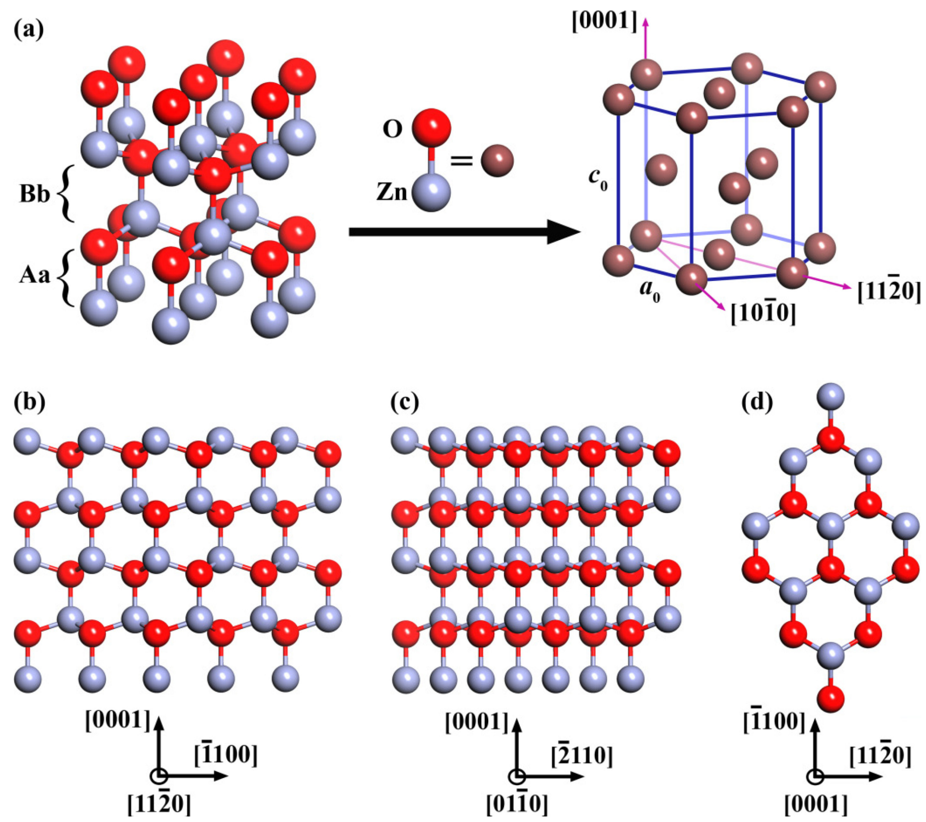


Figure 1.2 Schematics using the ball-and-stick model show (a) the wurtzite ZnO structure (O-polar) and the construction of hcp sublattice, and the ZnO lattice viewed from directions of $[11\bar{2}0]$ (b), $[01\bar{1}0]$ (c), and [0001] (d).

# Chapter 2

# Background and Literature Review

## 2.1 Direct growth of ZnO thin films on Si substrates

### 2.1.1 (100) Si substrates

For decades, (100) Si has been the dominate substrate utilized in IC industry. It has also been explored as a substrate for ZnO growth, beginning in the 1980s. Many growth techniques have been employed for the growth of ZnO on Si, including metal organic chemical vapor deposition (MOCVD),[24-37] pulsed laser deposition (PLD),[38-46] reactive radio-frequency (RF) magnetron sputtering,[47-56] reactive direct current (DC) sputtering,[57-60] electron-beam evaporation,[61] molecular bean epitaxy,[62,63] plasma immersion ion implantation,[64] and thermal oxidation.[65] Early work in the 1980s-1990s was mainly focused on fundamental studies of film structure and the dependence of growth rate on substrate temperature.[24-26,47] The ZnO films grown on (100) Si were of poor quality at that time and were used in surface acoustic wave devices and piezoelectric devices, where there was no strict requirement on the film crystallinity. Later, ZnO was recognized as a new transparent conducting oxide (TCO) with potential for UV optoelectronic applications. Thus far, researchers have performed systematic studies on structural, morphological, electrical, and optical properties of the films. In addition, improvement of the film quality has been attempted through optimization of the growth temperature and ambient,[35,38,43,51,52] post-growth annealing,[30,43,49] and modification of the growth techniques, such as introducing RF plasma[26,28,29] and light irradiation[33] during CVD growth. In recent years, there has been a surge of interest in fabricating heterojunction devices based on polycrystalline ZnO films,[34,37,57-59,60,62,66-68] most of which were manufactured directly on (100) Si.

Because of the large lattice mismatch of 40.2% and different structural symmetry between the basal plane of wurtzite ZnO ($a_{ZnO}$=3.2498Å) and the cubic Si (100) plane ($a_{Si}$=5.4309Å), the direct growth of ZnO on (100) Si is not epitaxial. As the growth temperature increases, the structure of the ZnO films evolves from amorphous to polycrystalline, then into a c-axis orientated (textured) structure with an out-of-plane orientation relationship of $(0001)_{ZnO}||(001)_{Si}$. The films prefer to grow along the [0001] direction because (0001) ZnO has a minimum surface free energy. Sometimes the orientation of (0001) ZnO has a deviation angle of 3-4.5 °C compared to that of (100) Si, depending on growth conditions and film thicknesses.[40,54] The degree of the out-of-plane orientation is characterized by full width at half maximum (FWHM) values of the 0002 ZnO $\omega$-rocking curves as measured by x-ray diffraction (XRD). For example, FWHM values of 1.44°-3.25° were reported by Jeong *et al.*[51] for ZnO films grown on (100) Si at 400 °C by RF magnetron sputtering. Han *et al.*[42] reported a smaller value of 1.01° for the films grown at 500 °C by PLD, however, the ZnO crystallites grow in the format of rotation domains with no preferable in-plane orientation, as shown by the cyclic shape in the in-plane XRD pole figure[40,42,54] in Figure 2.1(a) and the plan-view transmission electron microscopy (TEM) images in Ref. 53.

In 2006, Liu *et al*.[54] increased the growth temperature to 750 °C, while Shin *et al*.[53] increased it to 600 °C and annealed the films after growth. The high temperature growth and the post-growth annealing helped to improve the film crystallinity. As shown in Figure 2.1(b), the ZnO $\{10\bar{1}2\}$ pole figure shows four-fold symmetry of the in-plane orientation of the film, which is consistent with the in-plane symmetry of the (100) Si substrate.

Unfortunately, the high temperature growth and annealing also induce the formation of interfacial silicon oxide ($SiO_x$), which impedes the ability of the ZnO films to grow epitaxially. Choi *et al*.,[40] Zhang *et al*.,[41] and Tan *et al*.[37] all observed an amorphous $SiO_2$ layer of 2.5-4 nm thick between ZnO and Si, as shown in the high resolution TEM (HRTEM) images in Figure 2.2(a). Liu *et al*.,[54] Yuk *et al*.,[63] and Han *et al*.[42] also reported the amorphous-like interfacial layer (Figure 2.2(b)), even though the Si substrates were deoxidized by hydrofluoric acid prior to ZnO growth. Although the latter claimed this layer is amorphous ZnO, their interpretation of the HRTEM results may be

flawed due to possible ion beam damage imparted during TEM specimen preparation. In fact, the ambiguity about whether the amorphous layer is ZnO or Si phase was clarified by Choi *et al*.[40] in 2001. Their conclusion was drawn on the basis of indirect evidence of ZnO grown on glass, suggesting that the amorphous-like interface layer between ZnO film and Si substrate should be $SiO_x$ ($x$ is close to 2). This amorphous $SiO_x$ layer continues to draw attention from researchers because it is critical for device performance and reliability. However, there has been no indication that this $SiO_x$ layer can be completed prevented during the ZnO growth. Later in this paper (Section 4.3), we will present direct evidence to prove that this amorphous layer is $SiO_x$, and that it is generated during the ZnO growth.

Due to the poor polycrystallinity of the ZnO films grown on (100) Si substrates, optoelectronic applications of these films were not explored in homojunction structures consisting of both *n*- and *p*-type ZnO epilayers (as in the case of those constructed on sapphire substrates), but instead, attention was exclusively focused on heterojunction devices of photodiodes,[62] light emitters,[34,37,57,58,60,66,67] and laser diodes,[59,68] in which the Si substrate plays an important role. Taking advantage of the fact that both the conductivity and the Fermi level of Si can be adjusted over a wide range by boron or phosphorus doping, it is fairly easy and exciting to observe room-temperature (RT) electroluminescence (EL) from the ZnO films grown on resistive or conductive, *n*- or *p*-type (100) Si substrates, thus demonstrating different device concepts. In recent years, the research emphasis of ZnO on (100) Si has shifted from physical properties to device fabrication. Mandalapu *et al*.[62] incorporated *p*-type doping of Sb into ZnO and fabricated a *p*-ZnO/*n*-Si photodiode. Researchers led by D. R. Yang[57-60,66] demonstrated UV, visible, and even lasing EL from metal-insulator-semiconductor (MIS) structures of Au/$SiO_x$/ZnO, heterojunctions of $Mg_xZn_{1-x}O/n^+$-Si and ZnO/($p^-$, $p^+$)-Si, and a multi-layer structure of $Mg_xZn_{1-x}O$/ZnO/$SiO_x/n^+$-Si (Figure 2.3). Similar work has been done in the research group of X. W. Sun,[37,67] where EL from ZnO/$SiO_x$/($n$, $p$)-Si structures was observed (Figure 2.4). Usually, the carrier transport mechanisms of the junctions were discussed in terms of the Anderson model of energy-band diagrams, though with the effects of the $SiO_x$ layer and the interfacial dipoles and defect states often omitted. Recently, Song and Guo[56] looked into details of the carrier transport in *n*-ZnO/$SiO_x$/*n*-Si,

including the effects of surface states. They concluded that trap-assisted multistep tunneling was the dominant mechanism in the heterojunction.

There are some reports of the photoluminescence (PL) characteristics of ZnO on (100) Si, discussing native defects, such as oxygen vacancies and zinc interstitials, which may induce deep level emissions in PL spectra.[36,51,52,61,65] Dopants like Ge and Er were reported to change the PL emission properties.[55,44] In other instances of ZnO grown (100) Si, since polycrystalline ZnO exhibits good *n*-type conductivity, it can be used as a wide band-gap channel material in transparent thin-film transistor (TFT) devices. ZnO-based TFTs have been fabricated on (100) Si substrates with native $SiO_2$ >100 nm thick serving as the gate insulator.[45,50,69] The electron conductivity can be further enhanced by Al-doping.[27] For ferroelectric or ferromagnetic applications, ZnO thin films doped with Li or Co have also been fabricated on (100) Si.[39,41]

In short, polycrystalline ZnO thin films have been extensively grown on (100) Si for 30 years because of the availability of substrate and convenient processes. Although the polycrystalline quality of the thin films is limited because of the large lattice mismatch and interfacial $SiO_x$ layer, the ZnO/(100) Si heterojunctions were explored as a demonstration of optoelectronic device concepts and other applications that do not require highly crystalline ZnO films.

### 2.1.2 (111) Si substrates

In fact, ZnO thin films were grown on (111) Si substrates earlier than on (100) Si substrates. In 1971, Wasa *et al.*[19] reported an Al doped polycrystalline ZnO thin film grown on *p*-type (111) Si substrate by magnetron sputtering. The *n-p* resulting heterojunction showed a rectifying I-V characteristic dominated by tunneling-type current, indicating numerous trapping centers in the ZnO film. Since then, there have been no reports of ZnO growth on (111) Si (for almost 30 years), probably because of the more intensive exploration of ZnO on sapphire and (100) Si.

Since ZnO has six-fold symmetry in the (0001) basal plane, domain matching epitaxial growth[70] is actually more feasible on the threefold symmetric (111) Si substrate than on the fourfold symmetric (100) Si. In addition, the lattice mismatch between (0001) ZnO and (111) Si (15.4%) is much smaller than that between (0001) ZnO and (100) Si

(40.2%). Therefore, (111) Si should be a more practical substrate than (100) Si for the epitaxial growth of single-crystalline ZnO films. However, Fan *et al*.[71] reported polycrystalline ZnO films grown by PLD on (111) Si. Moreover, Choi *et al*.[40] compared the microstructures of the films grown on (111) Si with those on (100) Si and glass and concluded that no clear difference exists in the film crystallinity. The fact that (111) Si substrate does not yield better crystallinity for ZnO growth in these studies is most likely due to the native $SiO_x$ layer generated at the interface, which impedes the epitaxial growth of the ZnO film. On the other hand, Khranovskyy *et al*.[35] found a difference in the film conductivity and surface morphology between the ZnO films on (111) Si and those on (100) Si. They concluded that the films grown on (111) Si are usually smoother and more conductive than those on (100) Si due to a larger number of oxygen vacancies in the films induced by the oxidation of the ZnO/Si interface.

It seems the oxidation of the ZnO/Si interface during growth is a persistent obstacle to the growth of high quality epitaxial ZnO films directly on Si substrates with either (111) or (100) orientation. Formation of voids and severe lattice distortion at the ZnO/(111)Si interface have been reported by Miyake *et al*.[72] for growth under excess oxygen conditions. Wang *et al*.[73] reported that X-ray photoelectron spectroscopy detected O-Si bonding at the ZnO/(111) Si interface, even though the Si substrate was pre-cleaned in Argon plasma and nitrigenized in highly pure nitrogen plasma at 600 °C. In an attempt to prevent interfacial oxidation, Zhao *et al*.[74] have grown ZnO on (111) Si at 650 °C in vacuum ($2\times10^{-3}$ Pa). In a comparison with similar films grown in oxygen (50 Pa), reflection high-energy electron diffraction (RHEED) results, shown in Figures 2.5(a) and (b), suggests the films grown in vacuum are epitaxial while those grown in oxygen are polycrystalline. Unfortunately, the vacuum grown epitaxial ZnO films show poor optical quality in RT PL spectra (Figure 2.5(c)) compared to the polycrystalline films grown in oxygen (Figure 2.5(d)). The near-band-edge (NBE) emission at around 380 nm from the vacuum grown film is very weak, while the deep-level emission at around 520 nm is relatively more intense. The deep-level emission is correlated with structural defects such as oxygen vacancies or zinc interstitials, whose formation is favorable under vacuum growth condition.[51,75] Since optoelectronic devices require not only single crystallinity of

the film, but also a smooth surface and high optical quality, the growth of ZnO films in vacuum is not an appropriate method to alleviate the interface oxidation problem.

There are only a few research papers devoted to heterojunction devices of the ZnO thin films directly grown on (111) Si. *P*-type ZnO films were reported by intentional phosphorous doping[76] or diffusion from the phosphorous-doped $n^+$-(111) Si substrates.[77] However, the observed RT EL from the ZnO/P-ZnO/$n^+$-Si junction did not show UV emission but a rather weak visible deep-level emission.[77] Undoubtedly, although the ZnO films grown on (111) Si substrates have better crystallinity than those on (100) Si, the optical quality of the films needs to be improved, and the interfacial oxidation problem has to be conquered in order to realize potential optoelectronic applications. In the following part of this chapter, we describe an effective method for overcoming these problems, namely the introduction of an intervening homo- or hetero-buffer layer prior to the ZnO growth.

## 2.2 ZnO growth on Si using buffer layers

### 2.2.1 (100) Si with buffer layers

Inspired by the method of using intervening buffer layers during GaN thin film growth to improve the film crystallinity, researchers have recently employed different buffer layers prior to ZnO growth on (100) Si, effectively improving the film crystallinity from polycrystalline to highly textured structure. Fu *et al.*[78] were the first to introduce Zn buffer layers for the ZnO growth on (100) Si substrates, Zn being easy to deposit by reactive DC sputtering and oxidize by annealing. Indeed, the degree of the out-of-plane mis-orientation of the resulting ZnO films were improved by the Zn buffer layer and post-growth annealing, as seen in Figure 2.6, where the FWHM values of the 0002 ZnO $\omega$-rocking curves ($\omega$-FWHM) are reduced from 4.5° to 2.5°. Unfortunately, the reduced $\omega$-FWHM value is still large, suggesting the films may not be epitaxial but textured with no preferred in-plane orientation. The authors proposed a growth model, in which $(0001)[2\bar{1}\bar{1}0]_{ZnO}||(10\bar{1}0)[0001]_{Zn}||(100)[001]_{Si}$, to address how the Zn buffer layer modulates the lattice mismatch between ZnO and Si, though no experimental proof were provided. They also found that in PL measurements, the Zn buffer layer significantly enhanced the NBE emission at 392 nm from the films on (100) Si but had no impact on

the films grown on (111) Si (Figure 2.7). The enhanced NBE emission of ZnO/Zn/(100) Si was in agreement with the improvement of the degree of the out-of-plane mis-orientation. However, the films always exhibited strong deep level emissions, implying a high density of intrinsic defects such as oxygen antisite defect ($O_{Zn}$).[79]

The most popular buffer layer that has been pursued is the low temperature grown ZnO buffer layer (LT-ZnO).[80-83] Unlike the subsequent grown ZnO main film, this homo-buffer layer is directly grown on Si at a much lower temperature and with a smaller thickness, which enriches the LT-ZnO layer with misfit dislocations and point defects that yield an inferior film quality. However, this LT-ZnO buffer layer serves as a zero-mismatch template for the subsequent ZnO growth, while at the same time, the point defects migrate, interact with threading dislocations, and cause dislocation climbing and gliding, resulting in dislocation annihilation in the LT-ZnO layer vincinity.[80,84] Consequently, most of the threading dislocations do not penetrate the LT-ZnO layer, and thus the crystallinity of the top ZnO main film can be effectively improved. In addition, Zheng *et al*.[81] reported that this defective LT-ZnO buffer layer helps to provide relaxation of the built-in in-plane tensile strain, leading to nearly strain-free ZnO films grown on the LT-ZnO buffered (100) Si substrate. However, although the LT-ZnO buffer layer has the advantages of impeding dislocation propagation and relaxing the strain, the crystallinity of the top ZnO main film is still textured due to the large lattice mismatch and different structural symmetry between ZnO and (100) Si. Moreover, the problem of the interfacial oxidation layer remains.[83]

Some other buffer layers, such as GaN[85] and MgO[86-88] have also been tried for ZnO growth on (100) Si. However, the GaN and MgO buffer layers on Si have hexagonal structures which do not match the square (100) Si surface, and rotation domains often occur during the growth of the buffer layers and the ZnO films, resulting in textured ZnO films.[86] The only case reported of a single-crystalline thin film related to ZnO that was grown on (100) Si was one heavily alloyed with MgO, since $Zn_xMg_{1-x}O$ ($x \leq 0.18$) has a stable cubic structure and relatively small lattice mismatch (~22.1%) with (100) Si.[89,90] Cube-on-cube epitaxial structure of $Zn_xMg_{1-x}O$ grown on (100) Si was confirmed by TEM studies.[89]

Work on optoelectronic applications of ZnO films grown on (100) Si substrates with buffer layers was mostly reported by the research group of J. L. Liu.[82,87,88] They observed UV emission in RT EL from the heterojunction diode of Sb-ZnO/LT-ZnO/(100) Si,[82] and they also demonstrated UV NBE emission with almost no deep-level emission from the homojunction diodes of Sb-ZnO/Ga-ZnO/MgO/(100) Si, as shown in Figure 2.8(a).[87] Random UV lasing at RT was also achieved when MgZnO/ZnO/MgZnO quantum wells were incorporated into the homojunction structure.[88] These enhanced UV EL properties were attributed to the nanocolumnar structures in the textured films (Figures 2.8(a) and (b)), by assuming the center region of the columns was highly crystalline with low stress and dislocation density. These results indicate promising UV LED applications based on ZnO homojunction structures on (100) Si.

To summarize the effect of buffer layers in the growth of ZnO thin films on (100) Si, none of the buffer layers can provide epitaxial growth of single-crystalline ZnO, due to the large lattice mismatch and different symmetry between ZnO and (100) Si, but these buffer layers do improve the crystallinity and optical properties of the ZnO films and have positive effects on strain relaxation and dislocation suppression. There are promising results showing the possibility of achieving ZnO-based UV LED applications on (100) Si substrates with proper buffer layers.

### 2.2.2 (111) Si with buffer layers

As mentioned earlier in Section 2.1.2, domain matching epitaxy of ZnO growth on (111) Si is attainable because of the compatibility of the symmetries of (0001) ZnO and (111) Si. Enhanced crystallinity of the ZnO films on (111) Si is of great interest in long-lifetime optoelectronic applications under two conditions: (1) if the films could provide good optical quality, and (2) if the interface oxidation problem can be alleviated. To achieve these goals, researchers have grown many single-layer or multilayer buffer materials by different techniques prior to the ZnO growth on (111) Si. The list includes Zn,[78,91] AlN,[92] GaN,[92-94] $\gamma$-$Al_2O_3$,[95] wurtzite ZnS (wz-ZnS),[96-97] LT-ZnO,[98-104] $Si_3N_4$,[105] SiC,[106,107] MgO,[86] $Lu_2O_3$,[108] $Sc_2O_3$,[109] $Gd_2O_3$,[110] $Y_2O_3$,[111] LT-ZnO/Zn,[112] LT-ZnO/Al,[113] LT-ZnO/AlN,[114,115] MgO/Mg,[116] MgO/TiN,[117] LT-ZnO/MgO/TiN[118] etc. Consistently, it has been concluded that with the assistance of these intervening buffer layers, the

crystallinity, surface smoothness, and optical quality of the ZnO films grown on (111) Si can be significantly improved.

However, not all of these buffer layers yielded single-crystalline ZnO films. Textured ZnO films with hexagonal column structure[100,101] and random in-plane orientation[98] were usually produced under most growth conditions. Moreover, the ZnO film crystallinity is primarily affected by the buffer layer quality. Depending on the chemical reactivity, lattice mismatch, and interdiffusion between the buffer materials and Si, some buffer layers were amorphous, polycrystalline, or has defective interface with ZnO, all of which may severely degrade the quality of the subsequent ZnO film.[91,98,100,102,107]

#### 2.2.2.1 Single-crystalline ZnO thin films grown on (111) Si with buffer layers

All of the buffer layers that have been reported to enable single-crystalline ZnO growth are summarized in Table 2.1, which contains a comparison of lattice mismatches (misfits), growth techniques, experiments confirming the ZnO epitaxy, etc. It is apparent that among the buffer layers adopted in early years, AlN, GaN, and wz-ZnS are repeatedly able to produce good ZnO epitaxy. The major advantage of using these buffer layers is that they have the same wurtzite structure as ZnO, so that heteroepitaxy of ZnO on AlN, GaN, or wz-ZnS is highly feasible.

Inspired by the importance of epitaxial AlN and GaN buffer layers in successful fabrication of GaN-based LED, Tiwari *et al.*[92] and Nahhas *et al.*[93] were the first to explore AlN and GaN buffer layers for ZnO growth on (111) Si. During the growth of these nitride buffer layers, the growth ambient was either vacuum or nitrogen. It was suggested that the Si surface was nitridized rather than oxidized. Therefore the interface oxidation problem was effectively controlled, i.e. the buffer layers were supposed to be epitaxial on Si.[93] Furthermore, both AlN and GaN are relatively stable in oxygen ambient during the ZnO growth, and their lattice mismatches to ZnO are small (4.3% and 1.8%, respectively). Therefore, the ZnO films grown on AlN or GaN buffer layers are supposed to be highly crystalline. However, the TEM diffraction pattern in the report of Tiwari *et al.*[92] implies there was a small amount of polycrystalline AlN and ZnO embedded in the single crystalline films, which could be due to uncontrollable energetic clusters deposited

by PLD. ZnO films with better crystallinity were grown by MOCVD, according to Oleynik *et al*.[94] who reported FWHM values for 0002 ZnO $\omega$-rocking curves as small as 720″ (0.2°) for a 500 nm thick ZnO film grown on 1.3 μm GaN buffered (111) Si. Jiang *et al*.[114,115] reported even smaller 0002 $\omega$-FWHM values of 410″~460″ (0.114°~0.128°) for a 2.1 μm thick ZnO film grown on 20 nm AlN buffered (111) Si. Note that a 40-60 nm thick LT-ZnO buffer layer was also inserted between the ZnO film and the AlN buffer layer to improve the nucleation of ZnO in the initial stage of the growth. These small $\omega$-FWHM values and the XRD reciprocal space mapping in Figure 2.9 indicate good epitaxial quality of the ZnO films on AlN and GaN buffer layers.

Compared with AlN and GaN, wz-ZnS has a larger lattice mismatch (14.8%) to ZnO. However, (0001) ZnS has a very small lattice mismatch (0.52%) to (111) Si, which enables an easy epitaxial growth of ZnS on the (111) Si surface. Miyake *et al*.[96] and Yoo *et al*.[70] have proven from RHEED and XRD studies (Figure 2.10) that the wz-ZnS epilayer serves as a good buffer layer for ZnO growth by domain matching epitaxy. The XRD $\phi$-scans in Figure 2.10(b) indicate not only the in-plane six-fold symmetry of the ZnO films and the wz-ZnS films but also their epitaxial orientation relationship of $(0001)[10\bar{1}0]_{ZnO}||(0001)[10\bar{1}0]_{ZnS}||(111)[1\bar{2}1]_{Si}$. Yoo *et al*.[70] quoted the domain matching epitaxy of ZnO/ZnS as “five ZnS lattices fit six ZnO lattices and thus yields a small domain mismatch of 2.1%”. Here the concept of “domain matching epitaxy” is in accord with the concept of heteroepitaxy, that large lattice mismatch can be accommodated by interfacial misfit dislocations.

Similar RHEED or XRD features, such as those shown in Figure 2.10, have also been observed in ZnO films grown on (111) Si with buffer layers of metal epilayer (Zn[112] or Al[113]) or $\gamma$-$Al_2O_3$ epilayer.[95] Usually, the Si substrate surface is passivated by ZnS or the metal layers from oxidation, however, the epitaxial Al-doped ZnO film achieved on $\gamma$-$Al_2O_3$ buffer layer implies that it is unnecessary to protect the Si surface with nitride or sulfide. As long as the buffer material has thermodynamic stability when in contact with Si,[20] and the oxygen species around the Si surface are properly controlled, even oxide films can be epitaxially grown on Si and used as buffer layers for ZnO growth. The $\gamma$-$Al_2O_3$ epilayer with the structure of hausmannite is a good example. It is reported that the

$\gamma$-$Al_2O_3$ buffer layer has a low interfacial defect state density of $1.7\times10^{11}$ $cm^{-1}ev^{-1}$ on (111) Si.[95]

In recent years, more and more oxide epilayers have been adopted as buffer layers on (111) Si for ZnO epitaxy. Most of them have cubic structures and high dielectric-constants, including MgO and certain binary rare earth oxides with cubic bixbyite structure, such as $Y_2O_3$ and the oxides I used in this work: $Sc_2O_3$, $Lu_2O_3$, and $Gd_2O_3$. The bixbyite oxides generally have enthalpies of formation (Table 4.1) much larger than that of $SiO_2$ ($\Delta H_{SiO_2}$ = -910.7 KJ/mol),[119] and they are supposed to be thermodynamically stable when in contact with Si.[20] Therefore, it is expected that the growth of bixbyite oxides can impede the Si surface oxidation. In addition, bixbyite oxides have relatively smaller lattice mismatches to ZnO and Si compared with other buffer layer materials. Table 2.1 shows that the 1 μm thick ZnO films (with thin ZnO nucleation layer) I grew on (111) Si with epitaxial $Lu_2O_3$ (30 nm), $Sc_2O_3$ (100 nm), and $Gd_2O_3$ (60 nm) buffer layers, have smaller 0002 $\omega$-FWHM values, of only 0.08°~0.11°, than all others reported for ZnO growth on Si. This indicates our ZnO films are of high single-crystalline quality. The detailed structures and properties of these films will be discussed in Chapter 4. Figures 2.11(a)-(c) show the TEM results reported for ZnO epilayers grown on (111) Si with epitaxial $Y_2O_3$ buffer layers.[111] The Fourier filtered image of Figure 2.11(c) shows the periodic misfit dislocations at the ZnO/$Y_2O_3$ interface, which accommodated the lattice mismatch between ZnO and $Y_2O_3$. The ZnO film is single-crystalline though the $\phi$-scan in Figure 2.11(d) shows a small amount of twin structures with 180° in-plane rotation in the $Y_2O_3$ layer.[111]

Although MgO also has good thermodynamic stability when in contact with Si,[20] its enthalpy of formation ($\Delta H_{MgO}$ = - 601.6 KJ/mol)[119] has a smaller magnitude than that of $SiO_2$. Since the reported MgO buffer layer was fabricated by oxidation of Mg,[116] formation of silica is possible at the same time. Passivation layers such as TiN[117,118] and ultra low growth temperature[116] (-10 °C) were adopted to protect the Si surface. Nevertheless, all the reports of ZnO growth using MgO buffer layers show (in TEM studies) that the interface of MgO/Si contains a defective amorphous layer of either MgO or TiN. This defective interfacial layer, together with the large lattice mismatch (22.5%) between MgO and Si, may degrade the ZnO epitaxy. ZnO/MgO/TiN/$n^+$-Si heterojunction

structures have been fabricated, but only emission from defects level was observed in EL measurements.[117,118]

#### 2.2.2.2 Strain and cracking of the single-crystalline ZnO thin films

It is known that epitaxial thick ZnO films with high crystalline quality are desirable in many optoelectronic applications. However, since single-crystalline ZnO films have been achieved on (111) Si substrates with the buffer layers, as listed in Table 2.1, a new issue, cracking, has been encountered, and this may prevent the wide application of these high quality films.

Cracking was reported as a common problem in GaN epitaxy on Si,[120,121] as well as in other heteroepitaxy growth systems. In ZnO epitaxy on Si, cracking was observed in most of the high quality films with relatively larger thickness (≥500 nm) and smaller 0002 $\omega$-FWHM values (≤0.35°),[94,108-110,112-115] but it was not seen in amorphous or polycrystalline ZnO films. Figure 2.12 (a) shows a microscopic image of these cracks along the cleavage directions of $<1\bar{2}10>$ on the ZnO film surface. The reported crack density in ZnO films varies from 20 $cm^{-1}$ to $7\times10^2$ $cm^{-1}$.[113,115]

Possible reasons of the crack generation in epitaxial ZnO films were proposed by Tiwari *et al*.[92] Similar to the case in epitaxial GaN films, cracking is induced from large anisotropic tensile stress built in the film along the in-plane direction of $<10\bar{1}0>$. The existence of the tensile strain has been proven by the observation of spectra shifts in PL and Raman experiments.[92] Figure 2.12 (b) shows a schematic stress-strain relationship for brittle materials such as ZnO. The maximum stress at fracture point is the tensile strength. Direct measurement of the tensile strength of free-standing ZnO film is almost impossible, but it can be estimated from data fitting of measurement made on a double-layer structure including both the ZnO film and a substrate.[122]

Possible origins of the tensile strain in the films are (1) the lattice mismatch and (2) the mismatch of thermal expansion coefficients between the film and the substrate.[123] If the film has a smaller in-plane lattice parameter ($a^f$) than that of the substrate ($a^s$), the film is under in-plane tensile strain and bent concavely during the epitaxial growth; on the contrary, if $a^f$ is larger than $a^s$, then the film surface is under compressive strain and convexly bent during the growth. On the other hand, during post-growth cooling, thermal

strain is inevitably created in the film if the thermal expansion coefficients of the film and the substrate are different. If the thermal expansion coefficient of the film ($\alpha_{th}^{f}$) is larger than that of the substrate ($\alpha_{th}^{s}$), the film shrinks more than the substrate during cooling and is bent concavely under tensile strain; on the contrary, if $\alpha_{th}^{f}$ is smaller than $\alpha_{th}^{s}$, then the substrate shrinks more and the film is bent convexly with compressive strain. The relationships between the mismatches and the strain are illustrated in Figure 2.12 (c). The strain status of the film during growth can be obtained by *in situ* curvature measurements using an optical reflection sensor.[123] The final residual strain in the film after growth can also be estimated from *ex situ* asymmetric XRD measurements.[109]

The strain induced by lattice mismatch is usually fully relaxed by the formation of defects such as vacancies, interstitials, and dislocations after the film is grown beyond a critical thickness (usually several nanometers). It has been suggested that employing a low temperature grown nucleation layer (such as LT-ZnO) also benefits the accommodation of the lattice strain during the initial stage of the growth.[112] Therefore, the major origin of the residual strain in the film should be the mismatch of thermal expansion coefficients during the post-growth cooling process.

There is a large range in reported values of linear thermal expansion coefficients of ZnO and Si. It is critical that correct values be used since wrong conclusions, such as "compressive thermal strain in ZnO on Si",[92] are otherwise easily drawn. Table 2.2 is a list of generally accepted thermal expansion coefficients of Si, ZnO, and the buffer layers listed in Table 2.1. Note that for wurtzite materials, the linear thermal expansion coefficient in the basal plane ($\alpha_a$) is the ones to be considered in mismatch with that of (111) Si. Since the thermal expansion coefficient of ZnO in the basal plane ($6.51\times10^{-6}$ $K^{-1}$) is much larger than that of (111) Si ($2.6\times10^{-6}$ $K^{-1}$), tensile strain is inevitably built in the ZnO films on Si during post-growth cooling, regardless of whether buffer layers are employed or not. The higher the ZnO growth temperature, the more significant is the tensile strain developed during cooling. Cracking is often observed in thick ZnO films grown with buffer layers of AlN, $Sc_2O_3$, GaN, $Lu_2O_3$, and LT-ZnO, which have smaller thermal expansion coefficients than that of ZnO but larger than that of Si. On the contrary, no significant cracking has been reported for the films grown on buffer layers with larger

thermal expansion coefficients, for example, $Gd_2O_3$, ZnS, $\gamma$-$Al_2O_3$, and MgO. This phenomenon indicates the buffer layers with larger thermal expansion coefficients than ZnO may serve as a source of compressive thermal strain, partially compensating the tensile thermal strain and increasing the cracking critical thickness.

To summarize this section, it has been experimentally proven that domain matching epitaxy with proper buffer layers allows single-crystalline ZnO films to be epitaxially grown on (111) Si substrates. These films are of high crystalline quality as compared with those grown on (100) Si substrates and those grown without buffer layers on (111) Si. However, cracking occurs in thick films due to large in-plane tensile stress induced from thermal expansion mismatch between ZnO and Si. Cracking in the epitaxial ZnO films can severely damage device performance, and thus the fabrication of thick, crack-free ZnO epilayers is a challenging issue for building ZnO-based devices on Si substrates. It is necessary to obtain detailed information about the residual strain.

### 2.3 Summary and conclusions

ZnO thin films grown directly on (100) and (111) Si substrates have poor structural quality (i.e. polycrystalline or textured), limiting their use in optoelectronics and other applications that require crystalline ZnO films. Key issues that impede the ZnO epitaxy on Si have been addressed, including: (1) symmetry differences between the (0001) plane of wurtzite ZnO and the (100) plane of cubic Si; (2) large lattice mismatches between (0001) ZnO and (100) Si (40.2%) or (111) Si (15.4%); (3) the inherent reactivity between ZnO and Si which induces an interfacial amorphous $SiO_x$ layer.

Buffer layers have been employed in the growth of ZnO on (100) Si. Although they do not produce crystalline ZnO films, enhanced film texture, relatively good optical properties, and strain relaxation effect have been achieved. The highly textured ZnO films are capable of demonstrating device concepts in UV LEDs or other optoelectronic applications.

Remarkable progress in the growth of single-crystalline ZnO films on Si has been achieved on (111) Si substrates using epitaxial buffer layers of AlN, GaN, wz-ZnS, Al, Zn, $\gamma$-$Al_2O_3$, MgO, $Sc_2O_3$, $Lu_2O_3$, $Gd_2O_3$, and $Y_2O_3$. These epitaxial buffer layers have either wurzite structures or in-plane three-fold symmetries, and they exhibit good

thermodynamic stability in contact with Si. Therefore, employing these epitaxial buffer layers can effectively alleviate the problems of lattice mismatch and interface oxidation, allowing ZnO epitaxy on Si substrates. As a tradeoff, however, cracking usually occurs in thick epitaxial ZnO films due to thermal expansion mismatches between ZnO and Si during post growth cooling.

These single-crystalline ZnO films grown on (111) Si with buffer layers have great potential for optoelectronic applications and are essential to achieving the integration of multifunctional ZnO-based devices with Si electronics. Further optimization of the film structural, electrical, and optical qualities, acquisition of the information of the residual strain, and fabrication of thick and crack-free epitaxial ZnO films are the immediate tasks for building ZnO-based optoelectronic devices on Si.

Table 2.1 Buffer layers reported to yield single-crystalline ZnO growth on (111) Si, together with a comparison of lattice misfits, growth techniques employed, ZnO film thicknesses, FWHMs of $(0002)_{ZnO}$ $\omega$-rocking curves, and experimental techniques employed in proving the epitaxy.

| Buffer layer(s) | Misfit to $(111)_{Si}$ (%) | Misfit to $(0001)_{ZnO}$ (%) | Reference | Growth tech. | ZnO thickness (nm) | $(0002)_{ZnO}$ $\omega$FWHM (°) | Proof of epitaxy |
|---|---|---|---|---|---|---|---|
| AlN | 19.0 | -4.3 | Tiwari[92] | PLD | 500 | | TEM |
| | | | Jiang[114,115] | MOCVD | 2100 | 0.114~ 0.128 | $\omega$-rocking curve, optical reflectance |
| GaN | 16.9 | -1.8 | Tiwari[92] | PLD | 500 | | TEM |
| | | | Nahhas[93] | RF | 500 | | $\phi$-scan |
| | | | Oleyhik[94] | MOCVD | 500 | 0.2 | Reciprocal space mapping |
| wz-ZnS | 0.52 | 14.8 | Miyake[96] | e-beam | | | RHEED |
| | | | Yoo[70] & Onuma[97] | PLD | | 0.25 | $\omega$-rocking curve, $\phi$-scan |
| $\gamma$-$Al_2O_3$ | 2.4 | 13.3 | Kumar[95] | RF, PLD, MOCVD | 560 | | RHEED |
| LT-ZnO/ oxidized Zn | 15.4 | 0 | Kawamo-to[112] | MBE | 1000 | 0.23 | $\omega$-rocking curve, $\phi$-scan |
| LT-ZnO/ Al | 15.4 | 0 | Chen[113] | e-beam, MOCVD | 3000 | 0.35 | $\omega$-rocking curve |
| LT-ZnO/ $Lu_2O_3$ | 4.4 | 11.5 | Guo[108] (this work) | MBE, PLD | 1000 | 0.104 | $\omega$-rocking curve, $\phi$-scan, TEM |
| LT-ZnO/ $Sc_2O_3$ | 9.4 | 6.6 | Guo[109] (this work) | MBE, PLD | 1000 | 0.084 | $\omega$-rocking curve, $\phi$-scan, TEM |
| LT-ZnO/ $Gd_2O_3$ | 0.4 | 15.0 | Guo[110] (this work) | MBE, PLD | 1000 | 0.109 | $\omega$-rocking curve, $\phi$-scan, TEM |
| $Y_2O_3$ | 2.3 | 13.5 | Liu[111] | e-beam, PLD | 210 | | $\phi$-scan, TEM |
| MgO/ oxidized Mg | 22.5 | -8.4 | Wang[116] | MBE | 1000 | | RHEED, TEM, $\phi$-scan |
| MgO/TiN | 22.5 | -8.4 | Sun[117] | PLD, MOCVD | 900 | 0.8 | $\omega$-rocking curve, $\phi$-scan |
| LT-ZnO/ MgO/TiN | 22.5 | -8.4 | Zhang[118] | PLD | 160 | 1.0 | RHEED, $\phi$-scan, $\omega$-rocking curve |

Table 2.2 Linear thermal expansion coefficients at 300 K for Si, ZnO, and some buffer layer materials, listed in increasing order. Note that the data of $\gamma$-$Al_2O_3$ is a volume expansion coefficient.

| Material | Structure | Linear thermal expansion coefficient ($\alpha$) at 300 K ($\times 10^{-6}$ $K^{-1}$) | Ref. # |
|---|---|---|---|
| Si | diamond | 2.6 | 124 |
| AlN | wurtzite | 4.2 ($\alpha_a$); 5.3 ($\alpha_c$) | 125 |
| $Sc_2O_3$ | bixbyite | 5.2 | 126 |
| GaN | wurtzite | 5.6 ($\alpha_a$); 3.2 ($\alpha_c$) | 127 |
| $Lu_2O_3$ | bixbyite | 5.9 | 126 |
| ZnO | wurtzite | 6.5 ($\alpha_a$); 3.0 ($\alpha_c$) | 128 |
| $Y_2O_3$ | bixbyite | 6.5 | 126 |
| $Gd_2O_3$ | bixbyite | 6.8 | 126 |
| ws-ZnS | wurtzite | 8.4 ($\alpha_a$) | 129 |
| $\gamma$-$Al_2O_3$ | hausmannite | * $\alpha_V$=13.62 (volume) | 130 |
| MgO | rocksalt | 10.4 | 131 |

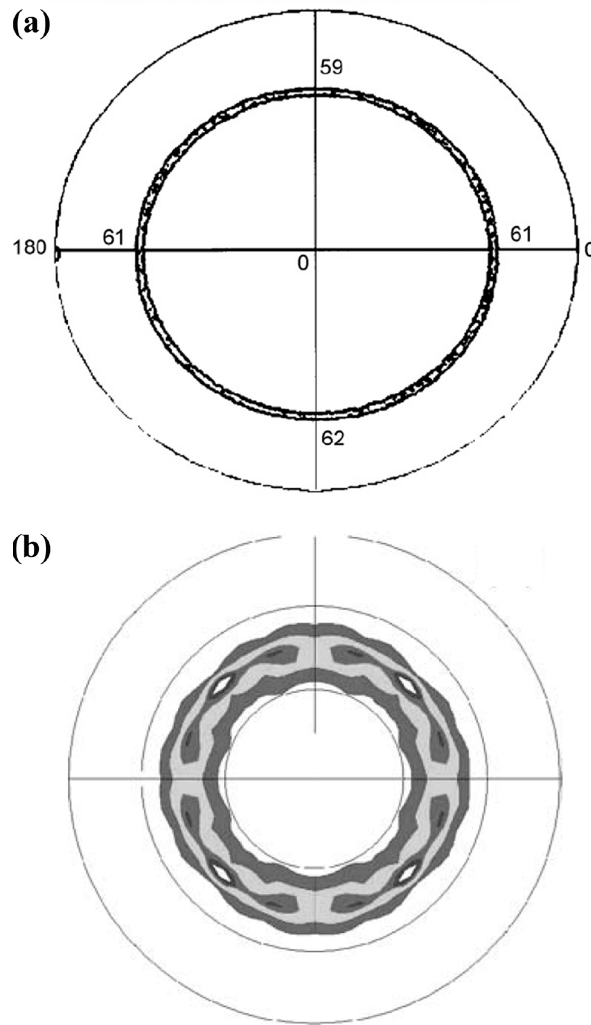


Figure 2.1 (a) Pole figure of ZnO $\{10\bar{1}1\}$ planes for the films grown on (100) Si at 500 °C. (b) Pole figure of ZnO $\{10\bar{1}2\}$ planes for the films grown on (100) Si at 750 °C. (from Han *et al*. [42] and Liu *et al*. [54])

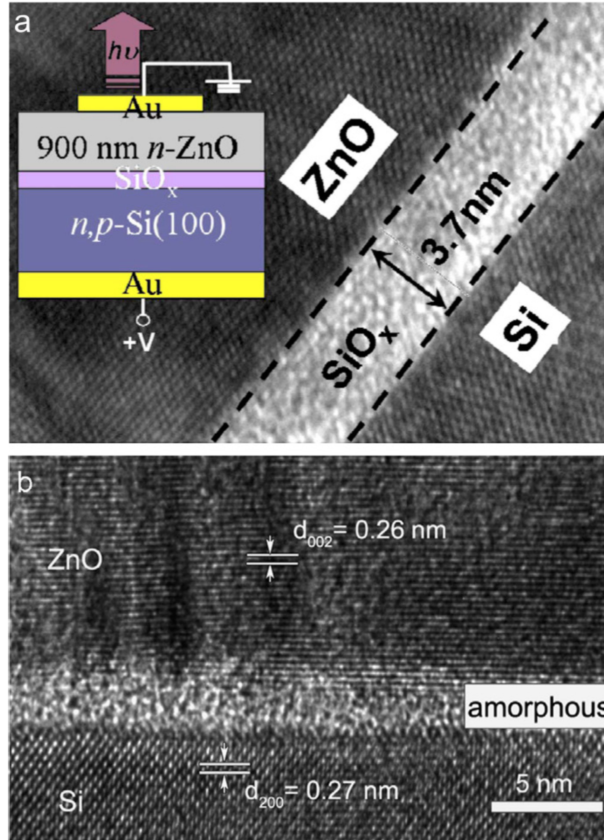


Figure 2.2 Cross-sectional TEM images of ZnO directly grown on (100) Si. (from Tan *et al*. [37] and Han *et al.* [42])

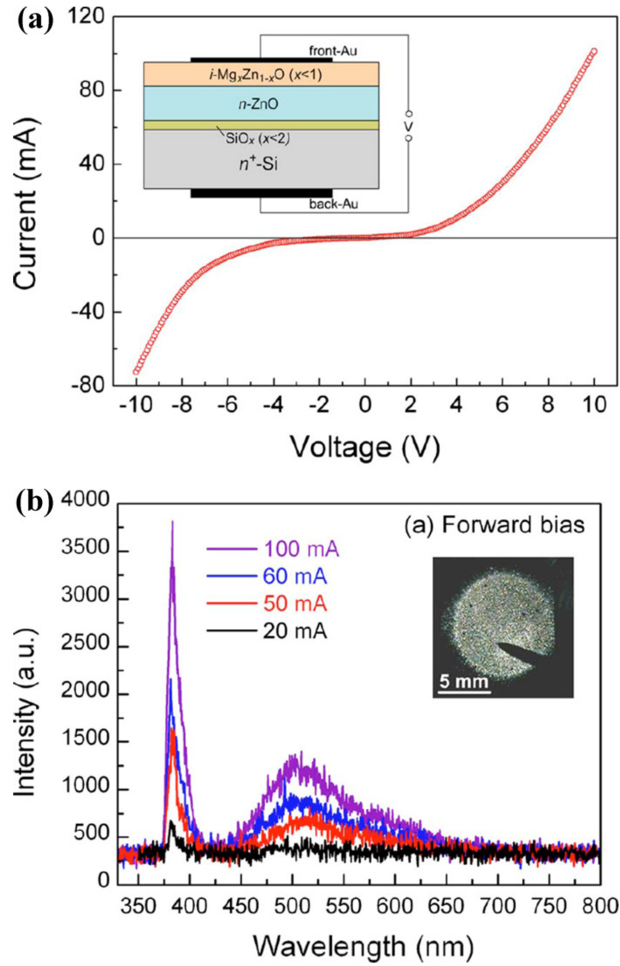


Figure 2.3 (a) I-V characteristics and schematic diagram of the *i*-$Mg_xZn_{1-x}O$/*n*-ZnO/$SiO_x$/$n^+$-(100) Si structure. (b) RT EL spectra under different forward current injections. The inset is a CCD camera image of the LED operating at a forward current of 100 mA. (from Chen *et al*. [66])

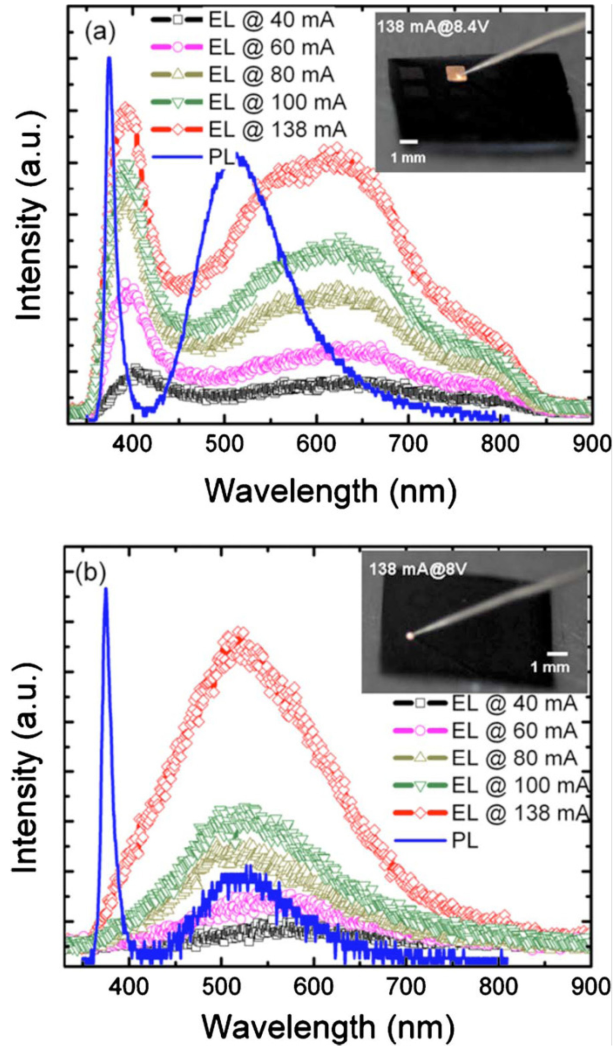


Figure 2.4 RT PL and EL spectra under different current injections for (a) *n*-ZnO/$SiO_x$/*n*-(100)Si, and (b) *n*-ZnO/$SiO_x$/*p*-(100) Si structures when Si is positive biased. Corresponding schematic is shown in Fig. 2.2(a). The insets are photographs of the LED devices operating at 138 mA. (from Tan *et al*. [37])

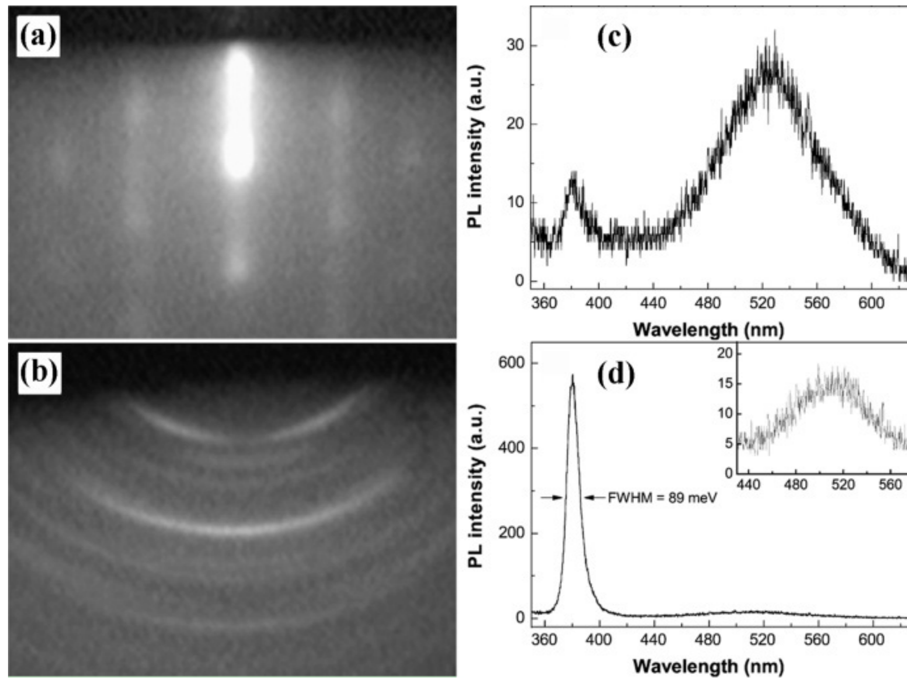


Figure 2.5 RHEED patterns and RT PL spectra of the ZnO thin films grown at 650 °C on (111) Si substrates in vacuum ((a) and (c)) and oxygen ambient ((b) and (d)), respectively. (from Zhao *et al*. [74])

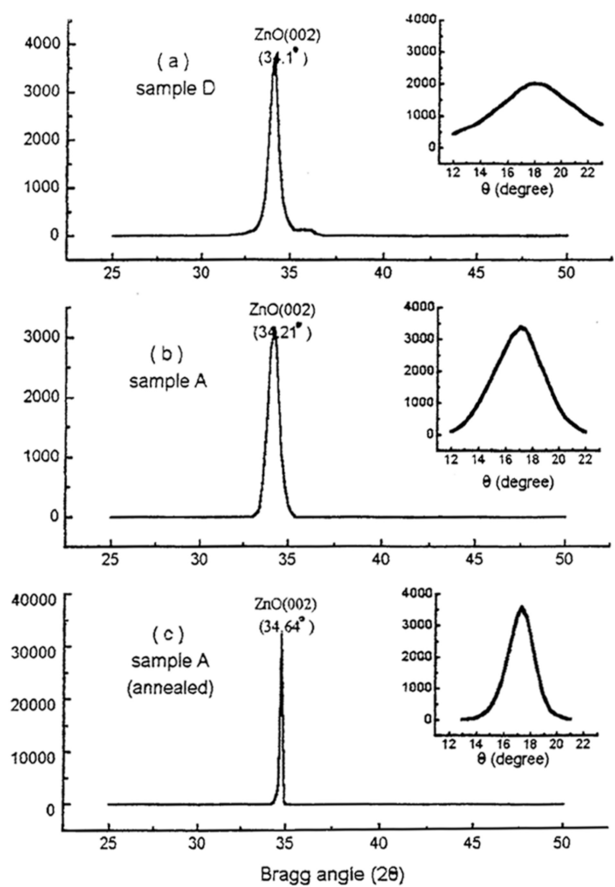


Figure 2.6 XRD $\theta$-$2\theta$ scans and rocking curves of ZnO films deposited on (100) Si, (a) without Zn buffer layer, (b) with Zn buffer layer, and (c) with Zn buffer layer and annealed at 800 °C for 1h. (from Fu *et al*. [78])

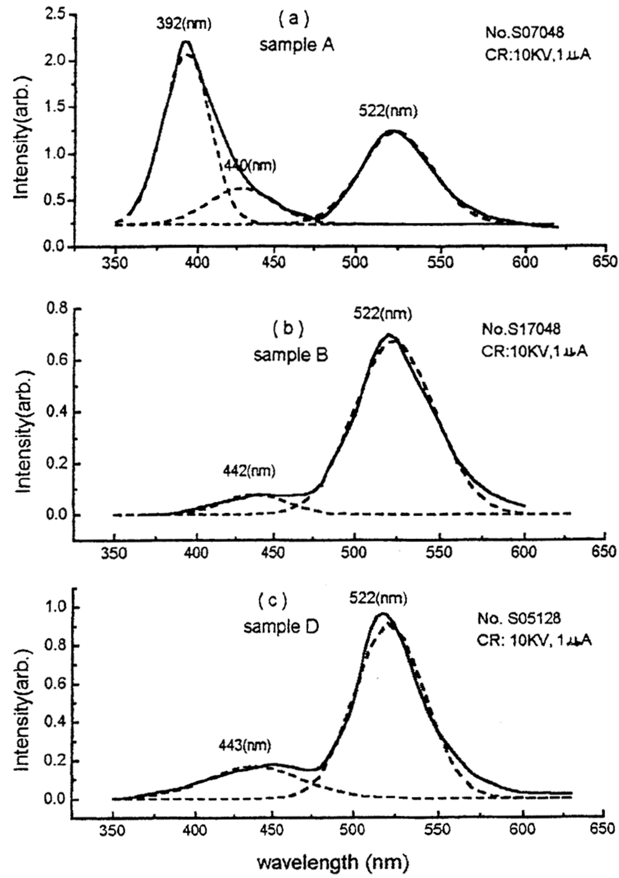


Figure 2.7 Comparison of RT cathodoluminescence spectra of annealed samples deposited on (a) (100) Si with Zn buffer layer, (b) (111) Si with Zn buffer layer, and (c) (100) Si without Zn buffer layer. (from Fu *et al*. [78])

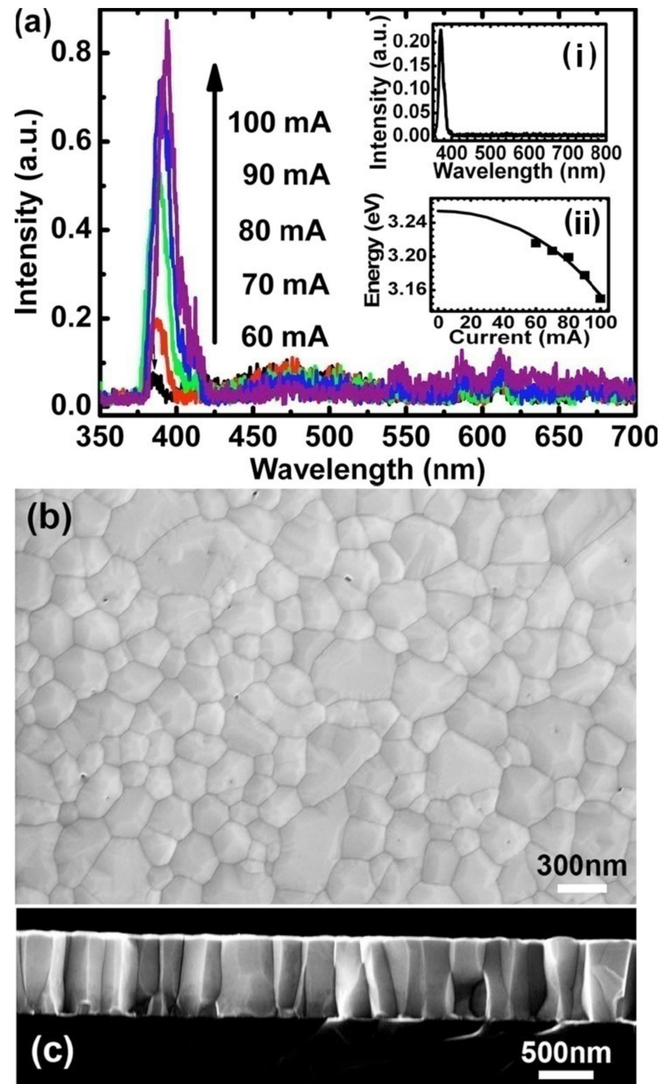


Figure 2.8 RT EL spectra (a), and plane view (b) and cross-sectional (c) SEM images of ZnO *p-n* junction on MgO buffered (100) Si. The insets are (i) RT PL spectrum and (ii) NBE energy fitting, respectively. (from Kong *et al*. [87])

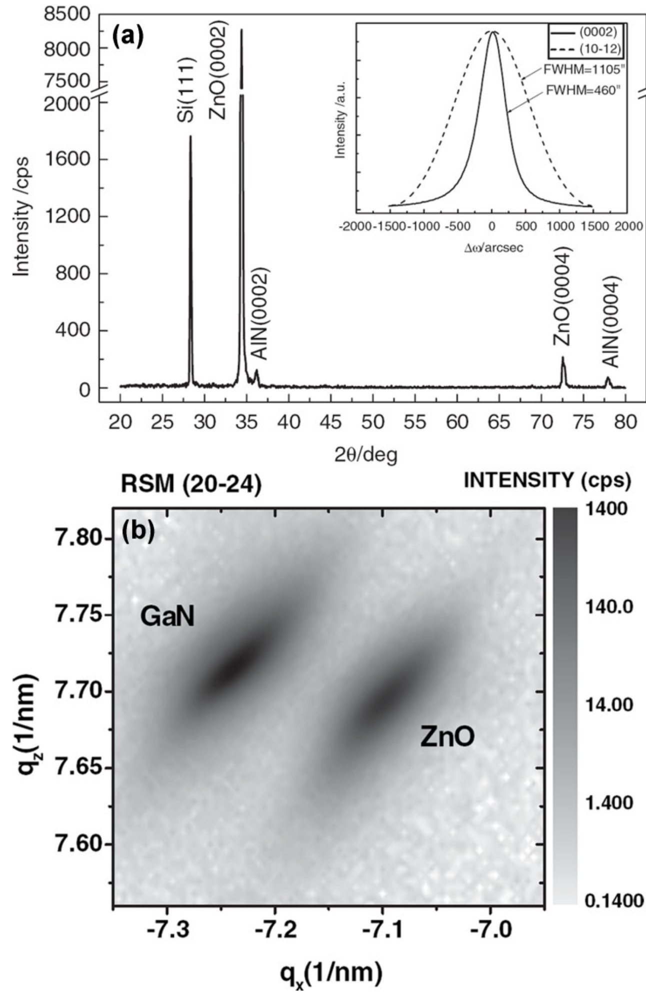


Figure 2.9 (a) XRD $\theta$-$2\theta$ scan of a ZnO/AlN/(111) Si film with inset showing $\omega$-rocking curves of the $0002_{ZnO}$ and $10\bar{1}2_{ZnO}$ reflections, respectively. (b) XRD reciprocal space mapping of asymmetrical $(20\bar{2}4)$ reflection of a ZnO/GaN/(111) Si film. (from Jiang *et al*. [115] and Oleynik *et al*. [94], respectively)

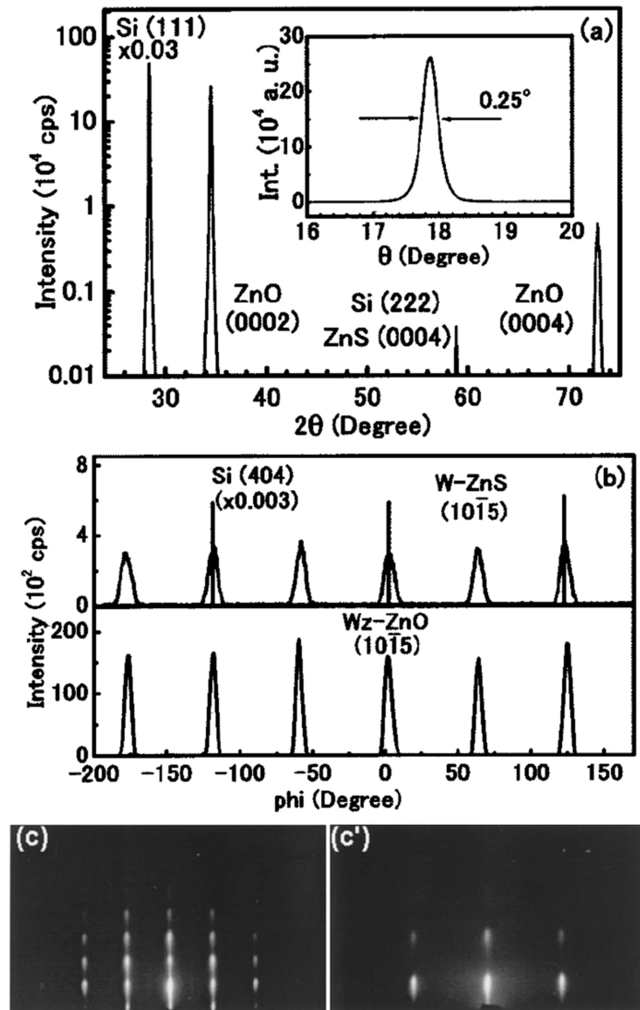


Figure 2.10 (a) XRD $\theta$-$2\theta$ and $\omega$-scans of a ZnO/ZnS/(111) Si film grown by PLD. The ZnS reflections overlap with Si reflections. (b) $\phi$-scans showing in-plane symmetries and orientation relationship. (c) and (c') RHEED patterns of a ZnO/ZnS/(111) Si film grown by electron-beam evaporation. The RHEED beam direction is $[11\bar{2}0]$ for (c) and $[10\bar{1}0]$ for (c'), respectively. ((a) and (b) are from Yoo *et al*. [70]; (c) and (c') are from Miyake *et al*. [96])

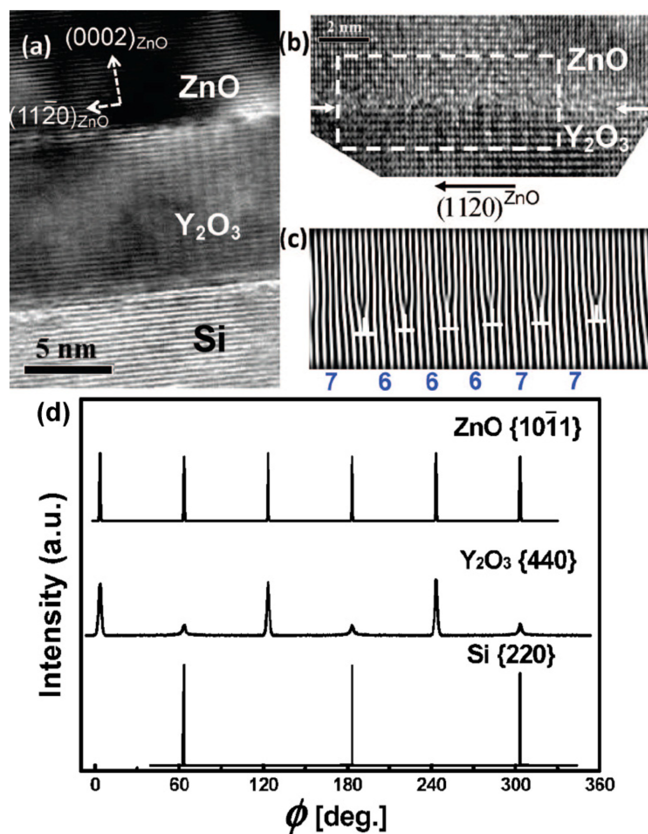


Figure 2.11 (a) Cross-sectional TEM image of a $ZnO/Y_2O_3/(111)$ Si film. (b) HRTEM image of the $ZnO/Y_2O_3$ interface. (c) Fourier filtered image of the selected area in (b). (d) $\phi$-scans shows twin structure in the $Y_2O_3$ layer. (from Liu *et al*. [111])

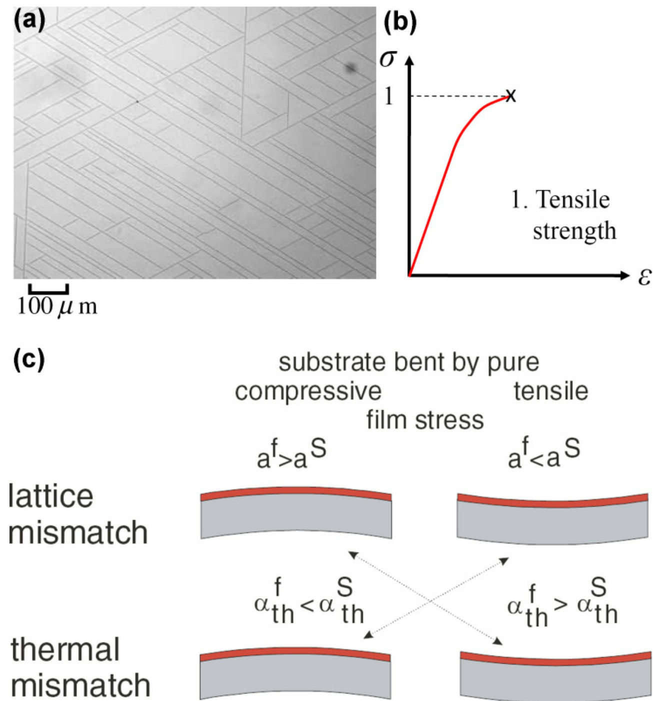


Figure 2.12 (a) Microscopic image showing cracked surface of ZnO/LT-ZnO/oxidized Zn/(111) Si grown by MBE. (b) Schematic of stress-strian relationship. (c) Relationships between the lattice and thermal mismatches, the strain in the film, and the curvature of the film surface. Compressive or tensile strain leads to convex or concave film surface. (Not drawn to scale.) (from Kawamoto *et al*. [112] and Krost *et al*. [123], respectively)

# Chapter 3

# Experimental Techniques

## 3.1 Pulsed laser deposition technique

In this work, pulsed laser deposition (PLD) is adopted to grow the ZnO thin films.

### 3.1.1 Dynamics of the PLD process

PLD is regarded as a versatile method to grow ceramic thin films, such as superconductor films,[132] semiconductor films,[133] and ferroelectric films.[134] A high energy pulsed laser beam (Excimer, $CO_2$, or Nd:YAG lasers) is focused onto the surface of a solid target. Strong absorption of the electromagnetic radiation by the solid surface leads to rapid evaporation of the target materials. The ablated materials consist of highly excited and ionized species. The energized particles present themselves as an immediate glowing plasma plume in front of the target surface, if the ablation is carried out in vacuum or low pressure ambient. The plasma vapor re-condenses on a substrate that is usually heated. Figure 3.1 shows a schematic of the typical PLD system. The main components of the PLD system include a laser, optics, and a vacuum chamber with pumping accessories.

The principle of PLD dynamics, in contrast to the simplicity of the system set-up, is a very complex physical phenomenon. It involves the following four physical processes of laser-plasma-solid interactions, as shown in Figure 3.2 (a).

(1) Interactions between high-power pulsed laser radiation and the solid target:

During the laser ablation process, unique phenomena such as target melting, ripple pattern formation,[135] and phase segregation are usually observed on the target

surface. The amount of material ablated per pulse is calculated according to the heat balance equation:[136]

$$\Delta x_t = \frac{(1-R)(E-E_{th})}{(\Delta H + C_v \Delta T)} \tag{3.1}$$

where $\Delta x_t$ is the evaporated target thickness, $R$ is the reflectivity of the target material, $E_{th}$ is the energy threshold above which evaporation occurs, $\Delta H$ is the volume latent heat, $C_v$ is volume heat capacity, and $\Delta T$ is the maximum temperature rise, respectively. Here the energy threshold depends on laser wavelength, pulse duration, plasma losses, and thermal properties of the target material.

(2) Interactions between the laser radiation and the evaporated high energetic materials:

During this process, the evaporated material plasma is further heated by absorbing the laser radiation through an inverse Bremsstrahlung process, which describes the absorption of a photon by a free electron. A schematic demonstration of the plasma-laser interactions is shown in Figure 3.2(b). The absorption coefficient $\alpha_p$ of the plasma is expressed as:[136]

$$\alpha_p = 3.69 \times 10^8 \frac{Z^3 n_i^2}{T^{0.5} \nu^3}(1 - e^{-\frac{h\nu}{k_B T}}) \tag{3.2}$$

where $\nu$ is the laser frequency, and $Z$, $n_i$, and $T$ are the average charge, ion density, and temperature of the plasma, respectively. Since $\alpha_p$ is proportional to $n_i^2$, the plasma absorbs the incident laser radiation only within a distance very close to the target, which is the region that has high ion density. To obtain the net rate of energy absorption in the plasma, it is necessary to allow for stimulated emission, which is represented by $(1 - e^{-\frac{h\nu}{k_B T}})$.[137] For PLD with an excimer laser, the plasma temperature is estimated to be in the range of 7000-20000 K, though the surface evaporation temperature is much lower.[138] Thus, $(1 - e^{-\frac{h\nu}{k_B T}}) \rightarrow 1$, and the absorption coefficient of the plasma exhibits $T^{-0.5}$ dependence when interacting with an excimer laser.

(3) Adiabatic plasma expansion and deposition of the thin film:

This is the process by which the target materials are transferred through the plasma plume onto the substrate. In the initial plasma expansion process, the plasma is considered to be an ideal gas, and it is also considered as a continuous fluid. The continuous fluid assumption holds because the particle density of the plasma is high ($10^{19}$-$10^{20}$ cm$^{-3}$). The rapid expansion of the plasma in vacuum results from large density gradients and large pressure gradients. At the beginning, the expansion velocities are relatively low, while the acceleration is very high. When the velocities increase (~$10^5$-$10^6$ cm/s) the acceleration starts to decrease and ultimately becomes zero, resulting in the elongated plume shape. After the laser pulse terminates, no particles go in or out of the inner edge of the single-pulsed-generated plasma (Figure 3.2(a)), thus the plasma expands adiabatically into the vacuum until it reaches the substrate. The acceleration of the plasma species depends on temperature, dimensions of the plasma, and the mass of the species.[136]

(4) Nucleation and intergrowth of the thin film on substrate surface:

After the plasma finally reaches the substrate, the particles in the plasma deposit on the substrate. The thin film thickness distribution profile D($\theta$) is represented by a cosine-power expression: [135]

$$D(\theta) \equiv \frac{B}{h^2}\cos^{p+3}\theta \tag{3.3}$$

where $\theta$ is the polar angle of plasma ejection measured from the normal of the target surface, $B$ is a normalization constant, $h$ is the distance between the target and the substrate, and $p$ is an empirical fitting parameter determined by the plasma species. The thickness distribution profile implies that the unique characteristics of employing a plasma plume during growth should be taken into consideration when using the PLD technique. As a result, uniformity considerations limit the substrate size to 2" diameter. Depending on the temperature, the substrate-film lattice mismatch, and the morphology of the substrate, and the density, the energy, and the ionization degree of the plasma, the nucleation of the thin film can be of 2-dimentional or 3-dimentional modes. These modes are usually referred to as continuous (liquid-like) growth and island growth, respectively.

Among the above processes, the first two occur during the time interval of the laser pulse, while the last two processes initiate after the laser pulse terminates. All of the

processes repeat with each pulse during the deposition, and each process is critical in control of crystallinity, stoichiometry, uniformity, surface morphology, and other properties of the thin film.

### 3.1.2 The PLD systems

ZnO films in this study were grown in two different PLD systems both using a KrF excimer laser. One system is manufactured by Neocera, Inc. and mostly used for the growth of ZnO thin films doped with antimony. The other system is manufactured by Thermionics Northwest, Inc. and mainly used for growth of ZnO thin film on Si substrates. The photos of the laser, the plasma plume, and the two systems are presented in Figure 3.3.

The KrF excimer laser (Compex 205, Lambda-Physik) has an output wavelength of 248 nm, a pulse duration of 22 ns, and a beam cross section of $8 \times 22$ mm$^2$. The laser tube is water-cooled and backed with refillable gas of Krypton-Helium-Fluorine-Neon (3.82%-1.68%-0.09%-94.41%) premix. In this study the laser repetition rate is set to 5 Hz and the beam energy is set to 100 mJ using a computerized controller. The laser beam is focused by a fused silica lens onto the target with a spot size of approximately $1 \times 2$ mm$^2$, corresponding to a fluence of ~1.7 J/cm$^2$.

The Neocera PLD system consists of a 14.5" diameter steel vacuum chamber equipped with a substrate holder, a target carrousel, a cryo-pump, and a turbo-pump (Varian V-330). The substrate holder can be heated up to 900 °C. Silver paste is used as the adhesive to hold the substrates. The target carrousel can hold six targets at one time. The cryo-pump is used for pre-stage pumping up to 30 mTorr when loading substrates. The turbo-pump can further lower the pressure of the chamber to $10^{-4}$ mTorr before deposition. The distance between the target and the substrate is fixed at 2.5" in this chamber. During deposition, active gases such as $O_2$ and $N_2$ etc. are introduced through a needle leakage valve. The gas background pressure is adjusted between 5 mTorr and 100 mTorr. A major advantage of using this system is that substrates with all kinds of shapes can be used in this system.

The Thermionics PLD system is an ultra-high vacuum system with a base pressure less than $5 \times 10^{-9}$ mbar ($3.8 \times 10^{-6}$ mTorr). A turbo-pump (Varian V-551) is used to

pump the 22” stainless steel chamber. A load-lock chamber (LLC) is attached to the main chamber and is used for transferring substrates and targets. The LLC is evacuated by its own turbo-pump (Pfeiffer TMU-71P) down to $1\times10^{-7}$ mbar ($7.5\times10^{-5}$ mTorr). The target manipulator can hold six targets vertically in-line at one time. The substrate manipulator has a fine-positioning stage which allows displacements of 1” up and down, 1” left and right, and 4” in and out of the chamber. The substrate manipulator can rotate continuously around 360°, and it is vacuum-sealed by a two-stage differentially pumped rotary seal. The substrate-target distance can be fine-positioned between 1.5” and 2.5”. A Pt-Rh filament is used to heat up the substrates radiatively. The maximum filament temperature is 1100 °C. The relationship between the filament temperature and the real substrate temperature has been calibrated by placing thermocouples directly in contact with the heater core and the substrates. As shown in Figure 3.4, for different substrate materials, the relationship is linear but the slope varies due to different thermal conductivities of the substrates. No adhesive can be used to hold the substrates due to the radiative heating. Therefore, especially designed substrate holders are adopted to hold $1\times1$ cm$^2$, $5\times5$ mm$^2$, and 2” diameter substrates.

The Thermionics system is similarly equipped with an active gas inlet controlled by a needle leakage valve. Oxygen is usually backfilled to $6.7\times10^{-3}$-$2.7\times10^{-2}$ mbar (5-20 mTorr) during the ZnO growth. Different from the Neocera system, the Thermionics system is connected to an RF plasma source (HD-25, Oxford Applied Research, Inc.) that is used to ionize $O_2$ or $N_2$ gas. Some of the depositions (Sections 4.5 and 6.3) were assisted with O-plasma of pressure $3\times10^{-5}$ mbar (0.02 mTorr) and power 150-275 W. The chamber was backfilled with oxygen to $6.7\times10^{-5}$ mbar (0.05 mTorr) during O-plasma-assisted growth.

Comparing the Thermionics system with the Neocera system is useful to understand when we choose each. The Thermionics system has ultra-high vacuum and does not incorporate silver paste, and thus the cross-contamination inside the chamber is considerably lower than that in the Neocera system. The LLC helps to maintain the ultra-high vacuum in the growth chamber and brings convenience to substrate loading. In addition, RF plasma-assisted growth is possible. However, Neocera system is in use

when regular shape substrates of 1×1 $cm^2$, 5×5 $mm^2$, or 2” diameter can not be used, and when we grow doped ZnO films.

### 3.1.3 Substrate preparation for ZnO growth

In order to explore ZnO epitaxy on Si substrates, we used 3” (111) *p*-Si wafers ($\rho$>50 Ω cm) as substrates for undoped ZnO growth. Epitaxial bixbyite oxide buffer layers were pre-grown by MBE on the (111) Si substrates. The detailed MBE growth conditions are discussed in Section 4.1. A dicing saw (MA6) was used to dice the Si wafers covered with bixbyite oxide thin films into 1×1 $cm^2$ substrates. Before dicing, the substrate surface was spin-coated with a thin layer of photo resist for protection. After dicing, the photo resist was completely removed by rinsing successively in acetone, methanol, and de-ionized water for 1 min each. The substrates were then blown dry in $N_2$ gas and transferred into the Thermionics chamber for ZnO growth. Prior to growth, the substrates were heated up in vacuum to avoid Si oxidation. During growth, the substrate temperature was set to 600 °C.

Double-side-polished (0001) $Al_2O_3$ substrates were adopted for the growth of Sb-doped ZnO thin films in the Neocera system. The substrates were ultrasonically cleaned in acetone, methanol, and de-ionized water for 5 minutes each, and blown dry in $N_2$ gas prior to loading. Growth temperature ranged between 400 °C and 600 °C. Some Sb-doped ZnO films were also grown on (100) Si and bixbyite oxide buffered (111) Si substrates at 550 °C in the Thermionics system (Section 6.3).

Other substrates that were incorporated for ZnO growth include (0001) ZnO substrate purchased from CrysTec GmbH, Cermet, Inc., and MTI, Inc., (100) Si with $SiO_2$ cap layer, (111) YSZ (Y-stabilized $ZrO_2$), etc., as listed in Table 3.1.

### 3.1.4 Target preparation for ZnO growth

Commercial ZnO targets of 1” diameter with high purity (99.999%) and high density (>95%) were purchased from Praxair, Inc. and SCI, Inc. The Sb-doped ZnO targets were homemade by grinding ZnO powders (99.999%) and $Sb_2O_3$ powders (99.99%) and uniaxially pressing in mold under $2\times10^4$ psi pressure, followed by cold isotropic pressing under $3\times10^4$ psi pressure and finally sintering at 1250 °C for 8 hours.

The finished Sb-ZnO targets have densities of 93-97% and contain 0.1-1.0 at.% Sb-doping.

Prior to growth, the targets were pre-ablated by the laser for 5 mins to remove surface contaminants. The targets were also regularly polished by SiC grit paper every 4-5 depositions to remove the ripple pattern on surface.

Table 3.1 includes other doped ZnO targets that have been made or purchased, and have incorporated in this study. As space is limited, it is impossible to provide in this thesis the detailed data of the films grown from those targets.

## 3.2 Structural characterization

### 3.2.1 Film thickness measurement

The thicknesses of the ZnO films were measured by three techniques.

For the ZnO films grown on (111) Si substrates with bixbyite oxide buffer layers, optical reflectance spectra were measured by the Filmetrics F20 Thin-film Measurement System located at Professor Phillips' lab in the Department of Electrical Engineering and Computer Science (EECS). The system has a wavelength resolution of 0.5 nm. The built-in film thickness analysis is based on the interference between the optical waves reflected at the film surface, the film/buffer interface, and the buffer/substrate interface. The calculated film thickness has a small error ≤±10 nm.

Based on similar interference theory, optical transmittance spectra can also be used to estimate film thickness. The optical transmittance spectra of Sb-doped ZnO films grown on double-side polished $Al_2O_3$ substrates were measured by Varian 50Bio UV-Spectrophotometer located at the Van Vlack Undergraduate Laboratory. The ZnO film thickness ($d$) can be roughly estimated by:

$$d = \frac{m}{2\left|\frac{n_2}{\lambda_2} - \frac{n_1}{\lambda_1}\right|} \tag{3.4}$$

where $\lambda_1$ and $\lambda_2$ are two wavelengths in the spectrum, $n_1$ and $n_2$ are the corresponding refractive indexes of ZnO[139], and $m$ is the number of periods between $\lambda_1$ and $\lambda_2$ in the spectrum. The film thickness determined by this method has an error of about ±50 nm.

When a mask is employed during the ZnO growth, a clean edge of the ZnO film is formed on the substrate. The film thicknesses of such samples were measured by the Dektak3 precision profilometer of the Michigan Ion Beam Laboratory (MIBL). Depending on the film thickness and surface roughness, the measured thickness has an error of around 10-50 nm.

### 3.2.2 X-ray diffraction

All ZnO films were characterized by two x-ray diffractometers of the J. D. Hanawat X-ray MicroAnalysis Laboratory. The first diffractometer is a Rigaku-Rotaflex rotating anode four-circle diffractometer operated at 40 kV and 100 mA. The second one is a triple-axis high-resolution BEDE-D1 diffractometer operated at 40 kV and 40 mA. Both instruments use monochromatic Cu-K$\alpha$ radiative sources ($\lambda$=1.54 Å).

#### 3.2.2.1 $\theta$-2$\theta$ scan

The Rigaku diffractometer was used for $\theta$-2$\theta$ scan of the ZnO thin films. A 0.5 mm source slit was used to limit the width of the x-ray beam. During the scan, the sample was placed vertically and rotated by $\theta$, and the detector was simultaneously rotated by 2$\theta$ with respect to the horizontal incident x-ray beam. The scanned 2$\theta$ range was set to 20°-130°. The scan speed was 5 °/min and the 2$\theta$ increment was 0.01 °/div. A thin film sample with surface area$\leq$1×1" w as fixed by clay on the sample holder. The sample surface was aligned by a pre-scan of the substrate surface reflection (e.g. 111 Si or 0001 $Al_2O_3$ reflection) with detector intensity up to 2.5-3.0×$10^4$ cps.

#### 3.2.2.2 $\omega$-scan

The BEDE diffractometer was used for $\omega$-scan, i.e. $\omega$-rocking curve scan, of the ZnO epilayers. A high resolution scan was performed by limiting the x-ray beam size with a channel cut collimator (CCC) crystal and two source slits (1 cm dia. and 0.5 mm, respectively). During the scan, the detector was fixed at the 2$\theta_B$ Bragg angle of the reflections (e.g. 0002 ZnO) and the sample was rocked within 2-3° deviation from $\theta_B$. The scan speed was chosen between 0.1-0.5 °/min and the scan increment was 0.005 °/div. The sample was fixed by double-sided tape on the sample holder, and the

position was pre-aligned to cut in the middle of the x-ray beam width by adjusting the triple axes (X, Y, and Z) and optimizing the tilt angle ($\chi$-scan) of the sample holder. The diffractometer axes and angles are referred to Figure 3.5.

The broadening of the rocking curve ($\omega$-FWHM) represents the mosaic misorientation of the reflection and is often used to judge the crystalline quality of the thin film. For ZnO epilayers, the broadening of symmetric 0002 and off-axis $10\bar{1}2$ reflections are measured to estimate the degree of the out-of-plane and in-plane misorientation. The ZnO 0002 reflection is measured in the common symmetric geometry as described above and shown in Figure 3.6(a). The ZnO $10\bar{1}2$ reflection is measured in skew symmetric geometry, as shown in Figure 3.6(b), where the sample holder is first inclined by an angle ($\chi$) equaling the intersection angle between the surface plane (0002) and the measured plane ($10\bar{1}2$), and then rotated an azimuthal angle $\phi_0$ surrounding the $[10\bar{1}2]$ axis to satisfy the Bragg condition of $10\bar{1}2$ reflection. The detailed procedure of doing a skew symmetric $\omega$-scan is presented in Appendix A.

#### 3.2.2.3 $\phi$-scan

A $\phi$-scan of higher order off-axis reflection in XRD is a powerful technique to accurately determine the in-plane orientation relationship between film and substrate, and to reveal a possible twin structure in the film.

The $\phi$-scans in this study were performed in the glancing incidence geometry using the BEDE diffractometer as shown in Figure 3.6(c). The measured off-axis reflection was selected to be $11\bar{2}4$. During the scan, the detector was fixed at the $2\theta_B$ Bragg angle of the reflection, and the sample was fixed at $\omega=\theta_B-\chi_0$. The $\chi_0$ angle equals the intersection angle between $\{11\bar{2}4\}$ and (0002). In the glancing incidence geometry, the sample holder does not need to be inclined ($\chi=0$), but the $\omega$ angle is reduced to $\theta_B-\chi_0$ to satisfy the Bragg condition.

Because of the six-fold symmetry of ZnO, a full $\phi$-scan within 0°-360° of the $11\bar{2}4$ ZnO reflection should contain six peaks of the same intensity with intervals of 60°. The FWHMs of the peaks imply the film mosaic quality. If an extra set of peaks with separations of 60° appear, even if with low intensity, they indicate twin structure in the

films. Sometimes, due to non-uniformity of the film thickness or misalignment in XRD measurement, the six peaks in the $11\bar{2}4$ ZnO $\phi$-scan have different intensities. The intensity can be maximized by optimizing the $\omega$ and $\phi$ angles. The comparison of peak positions in $\phi$-scans of both the film and the substrate yields the in-plane orientation relationship between the film and the substrate. Appendix A also lists the angles setting used in the $\phi$-scans of ZnO $11\bar{2}4$ reflection, $Al_2O_3$ $11\bar{2}9$ reflection, and Si 440 reflection, respectively.

#### 3.2.2.4 Pole figure

The right arm of the Rigaku diffractometer is capable of pole figure measurements. It was used to determine the texture of the thin films, as well as the in-plane orientation relationship. The sample was fixed on a round triple-axis rotating plate. During the measurement of ZnO $10\bar{1}1$ pole figure, the sample plate was moved to the Bragg angle ($\omega$=$\theta_B$) of ZnO ($10\bar{1}1$), and the detector was fixed at $2\theta_B$. Then the sample plate was inclined from $\chi$=0° to $\chi$=80° with a step of 5°. A 360° $\phi$-scan, with a step of 10°, was measured at each $\chi$ angle. All these $\phi$-scans plotted on the same polar diagram forms the XRD pole figure.

Figure 3.7 shows an example of ZnO $10\bar{1}1$ pole figure of the ZnO films grown in this study on (111) Si substrates with the bixbyite oxide buffer layers. The label on the polar axis refers to 90°-$\chi$. It was very difficult to align the sample surface perfectly in position, so the intensities of the poles are not homogeneous. Both ZnO $10\bar{1}1$ poles and Si 200 poles showed up because of the close Bragg angles. Compared with the polycrystalline and textured ZnO pole figures reported elsewhere (Figure 2.1), the six ZnO poles and three Si poles observed in Figure 3.7 clearly indicate the single crystallinity of the ZnO films in this study. It also implies an in-plane orientation relationship that agrees with the relationship obtained from $\phi$-scans in Section 4.2.

#### 3.2.2.5 Determination of tilt and twist angles and dislocation densities

The tilt and twist angles of epilayers grown on mismatched substrates are two crystallographic parameters introduced to quantitatively determine the out-of-plane and

in-plane components of the mosaic misorientation, respectively. High-resolution triple-axis XRD is essential to measure the two angles.

The tilt angle, representing the out-of-plane misorientation, can be obtained from the broadening of ZnO $\omega$-scans of symmetric reflections 0002, 0004, and 0006 by the Williamson-Hall analysis[140], when the FWHM values measured for each reflection 000$l$ ($l$=2, 4, 6) are fitted by a straight line in the plot of FWHM×Sin$\theta_B/\lambda$ vs. Sin$\theta_B/\lambda$. Here $\theta_B$ is the Bragg angle of each reflection and $\lambda$ is the x-ray wavelength. The slope of the linear fitting is a direct measure of the tilt angle ($\alpha_\Omega$) of the film.[141]

The twist angle ($\alpha_\Phi$), representing the in-plane rotation of sub-grains about the surface normal, can be obtained from the broadening of skew symmetric $\omega$-scans of off-axis reflections $10\bar{1}l$ ($l$=1-5) using the Srikant analysis of inter-dependent distribution[142]. The FWHM values measured for each off-axis reflection, together with the FWHM value of the 0002 reflection, are plotted with respect to the inclination angles $\chi$ of the sample during measurements. The plot is then fitted, considering an exponential interaction between the tilt and the twist distributions, by the following equations (modified from Ref. 142):

$$\omega_0^{\text{tilt}}[\chi] = \cos^{-1}[\cos^2(\chi)\cos(\omega_y) + \sin^2(\chi)] \tag{3.5}$$

$$\omega_0^{\text{twist}}[\chi] = \cos^{-1}[\sin^2(\chi)\cos(\omega_z) + \cos^2(\chi)] \tag{3.6}$$

$$\omega_{\text{eff}}^{\text{twist}}[\chi] = \omega_0^{\text{twist}}[\chi]\exp\left(-m\frac{\omega_0^{\text{tilt}}[\chi]}{\omega_0^{\text{tilt}}[0°]}\right) \tag{3.7}$$

$$\omega_{\text{eff}}^{\text{tilt}}[\chi] = \omega_0^{\text{tilt}}[\chi]\exp\left(-m\frac{\omega_0^{\text{twist}}[\chi]}{\omega_0^{\text{twist}}[90°]}\right) \tag{3.8}$$

$$\omega(\text{resultant}) = \{\omega_{\text{eff}}^{\text{twist}}[\chi]^n + \omega_{\text{eff}}^{\text{tilt}}[\chi]^n\}^{1/n} \tag{3.9}$$

where $\omega$(resultant) is the Pseudo-Voigt fitting of the FWHMs for $\chi$ varies within 0°-90°, $\omega_y$ is the FWHM of the surface normal reflection ($\omega_y = \omega_0^{\text{tilt}}[0°]$=FWHM$_{0002}$), $\omega_z$ is the FWHM of the in-plane reflection ($\omega_z = \omega_0^{\text{twist}}[90°] = \text{FWHM}_{10\bar{1}0}$), and $m$ is a parameter within 0-1 characterizing the inter-dependence between the two distributions. Here $\omega_z$ corresponds to the twist angle $\alpha_\Phi$. For highly crystalline ZnO epitaxial films, the parameter $m$ is usually chosen to be less than 0.4. The angle settings of the measured

reflections and the MATLAB code developed for the Srikant analysis of the twist angles are included in Appendix A.

Assuming random distribution of the dislocations in the films, the dislocation densities are estimated by Gay *et al.*[143] and modified by Dunn *et al.*[144] as follows:

$$N_c = \frac{\alpha_\Omega^2}{4.35 b_c^2}; \quad N_a = \frac{\alpha_\Phi^2}{4.35 b_a^2} \tag{3.10}$$

Here $N_c$ and $N_a$ are the densities of *c*-type and *a*-type dislocation components, which have Burgers vectors $\mathbf{b}_c$ and $\mathbf{b}_a$ lying respectively parallel to *c*-axis and in the basal plane. Note that a mixed type dislocation may be counted in both $N_c$ and $N_a$.

#### 3.2.2.6 Determination of out-of-plane and in-plane strains

Due to the lattice and thermal expansion mismatches between the film and the substrate, the residual strain in the film stretches or shrinks the actual lattice constants of the film, leading to small deviations in the Bragg angles measured in XRD compared to standard Bragg angle values.

The residual strain in ZnO films grown on (111) Si substrates with bixbyite oxide buffer layers was investigated in this study. XRD $\theta$-$2\theta$ scans were performed using the BEDE diffractometer, taking the Bragg angles of the substrate peaks as the zero-strain references. In symmetric geometry, the out-of-plane ZnO 0002 reflection was measured in the same $\theta$-$2\theta$ scan as the Si 111 reflection. Assuming the Si 111 peak is located at the standard Bragg angle of $\theta_{\mathrm{Si}}$, the actual Bragg angle of ZnO 0002 peak is determined as $\theta_{\mathrm{B}}^{\mathrm{actual}} = \theta_{\mathrm{Si}} + \delta\theta$, where $\delta\theta$ is the displacement between the ZnO 0002 peak and Si 111 peak in the $\theta$-$2\theta$ scan. In skew symmetric geometry, the measurement of ZnO $10\bar{1}3$ reflection has a close inclination angle ($\chi$=31.66°) compared to that of Si 113 reflection ($\chi$=29.5°). Therefore, when the inclination angle is set near 30°, both reflections can show up in the $\theta$-$2\theta$ scan. Similarly, the actual Bragg angle of ZnO $10\bar{1}3$ reflection can be determined referred to Si 113 reflection.

Applying the Bragg equation:

$$2d \sin\theta_{\mathrm{B}}^{\mathrm{actual}} = \lambda \tag{3.11}$$

and the d-spacing equation of hexagonal lattice:

$$\frac{1}{d^2} = \frac{4}{3}\left(\frac{h^2 + hk + k^2}{a^2}\right) + \frac{l^2}{c^2} \tag{3.12}$$

to both ZnO 0002 and $10\overline{1}3$ reflections, the actual lattice constants *a* and *c* of the strained ZnO film can be obtained. Thus the residual strains along the *c*- and *a*-axes in the ZnO film can be calculated by:

$$\varepsilon_{zz} = \frac{c - c_0}{c_0}; \quad \varepsilon_{xx} = \frac{a - a_0}{a_0} \tag{3.13}$$

where $c_0$=5.2042 Å and $a_0$= 3.2496 Å are adopted for unstrained ZnO film.[22]

The ratio of $\varepsilon_{zz}$ vs. $\varepsilon_{xx}$ should be constant and related with the Poisson number ($\gamma$) of ZnO by:[145]

$$\frac{\varepsilon_{zz}}{\varepsilon_{xx}} = -\frac{2\gamma}{1-\gamma} \tag{3.14}$$

The Poisson number reported in literatures is about 0.3 for ZnO[145,146] and 0.23 for GaN.[147] For reference, the Poisson number is about 0.5 for rubber, and 0.18-0.3 for glass materials.

### 3.2.3 Atomic force microscopy

The film surface structure was characterized by a Digital Instruments NanoScope IIIa Scanning Probe Microscope located at the Electron Microbeam Analysis Laboratory (EMAL). The microscope was operated under Tapping-Mode during scanning, allowing the imaging of the surface morphology by tracking a small silicon cantilever ($\mu$-masch NSC15/AIBS) over the surface and recording the oscillation of the coupled laser signals. The cantilever was pre-tuned, oscillating near the resonance frequency around 300 kHz. Images were recorded at a scan size of 5×5 $\mu m^2$ and a scanning rate of 1-2 μm/s. With the EV scanner installed, the maximum scan size can be 14.8×14.8 $\mu m^2$. The ultimate resolution in a small size scan can reach 1 Angstrom when the scan rate, the proportional gain, and the integral gain of the cantilever are optimized. The Nanoscope III software offers 1-D and 3-D processing of the images, root-mean-square (rms) roughness and grain size analyses of the entire image, and cross-sectional analysis.

### 3.2.4 Transmission electron microscopy

The film microstructures and defects were studied by JEOL 2010F Analytical Electron Microscopy (AEM) and JEOL 3011 TEM (HRTEM) located at EMAL, and JEOL 2100F Scanning Transmission Electron Microscopy (STEM) at the University of South Carolina. TEM specimen preparation and TEM imaging were done by our research group members: Yi Zhang (part of Ch4 and Ch5), Yanbin Chen (part of Ch4 and Ch6), Michael Katz (part of Ch4), and Christopher Nelson (part of Ch4).

The JEOL 2010F AEM was used to perform cross-sectional diffraction contrast imaging of the films. It has an electron source of zirconated tungsten thermal field emission gun, operated at 200 kV, with conventional lattice resolution of 0.1 nm, and point-to-point resolution of 0.25 nm. It is also capable of other analytical techniques, including x-ray energy dispersive spectrometry (EDS), electron energy loss spectrometry (EELS), and STEM mode $Z$-contrast imaging.

The JEOL 3011 HRTEM was used for high resolution phase contrast imaging of the film's atomic structure, such as the interfaces and defects structures. The accelerating voltage is optimized at 300 kV. The lattice resolution is 0.14 nm and the point-to-point resolution is 0.17 nm. The specimen stage can be tilted over a range of ±30°, allowing various choices of illumination conditions. A Gatan 794 slow scan CCD TV system and a Gatan 622SC image intensified TV rate camera are equipped to allow digital recording of the HRTEM images.

The JEOL 2100F STEM is an advanced field emission electron microscope equipped with a spherical aberration ($Cs$) hexapole STEM probe corrector (CEOS GmbH). The accelerating voltage is at 200 kV. The TEM point-to-point resolution is 0.19 nm. The STEM probe size is $<0.1$ nm. $Z$-contrast image is obtained in STEM mode by focusing and rastering the electron probe across the specimen while using a Fischione high angle angular dark field (HAADF) detector to collect the scattered electrons. The brightness of atoms in the $Z$-contrast image is approximately proportional to the square of the atomic numbers ($Z$).

Preparation of TEM thin film specimen consists of standard processes of mechanical grinding, polishing, precision dimpling, and ion milling. High quality TEM imaging requires a critical thickness of the specimen to be electron-transparent, and little

artificial damage of the specimen. Detailed information of the preparation procedure can be found in Ref. 148. The imaging zone-axis of the ZnO films was chosen along the *a*-axis $<11\bar{2}0>$ rather than $<10\bar{1}0>$ for better atomic resolution. Therefore, the specimen was pre-cut along ZnO $<10\bar{1}0>$. Precise determination of the cutting direction was enabled by finding the azimuthal angle $\phi_0$ in skew symmetric XRD $\omega$-scan of off-axis reflections (Appendix A).

## 3.3 Composition characterization

### 3.3.1 Secondary ion mass spectrometry

Secondary Ion Mass Spectrometry (SIMS) was performed to detect very low concentrations of dopants and impurities in the ZnO films. Elemental SIMS depth profiles of pure ZnO targets and the ZnO films grown on Si substrates with bixbyite oxide buffer layers were measured at Evans Analytical Group LLC, CA. The sample surface was sputtered with a beam of primary ions, and the formed secondary ions were extracted and analyzed using a mass spectrometer. The sputtering destroyed the sample surface. The experimental accuracy is around 90%. There are various concentration limits for different elements, below which the detected signals are too small for accurate analysis.

The depth profile of several impurities in thecommercial ZnO target is shown in Figure 3.8. Besides the element of In whose concentration is below the detection limit, the major impurities in the ZnO target include Fe and Ca, with concentrations of $10^{16}$-$10^{17}$ $cm^{-3}$. The Fe impurities could possibly be induced during laser alignment when the laser occasionally hit the target holder and deposited Fe on the target surface. The impurities Ca, K, and Na could be artificially induced when handling the target. Possible sources for the impurities In, Ga, and Al are the cross-contaminations in the growth chamber since other targets doped with these elements were used in the same chamber. All of these impurities could also possibly be induced from contaminations in the ZnO target manufacturing process. Pre-ablation of the target by the laser is necessary to remove the cross-contamination impurities as much as possible prior to the ZnO growth.

### 3.3.2 X-ray photoelectron spectroscopy

X-ray Photoelectron Spectroscopy (XPS) was used to study the doping concentration and chemical bonding state in the Sb-doped ZnO films. The Kratos Axis Ultra XPS located at EMAL with a monochromatic Al source was used. The base pressure was $<5\times10^{-7}$ Torr. The photoelectrons excited from the sample surface by the soft x-ray were analyzed according to their kinetic energies; thus, the elements in the film and their chemical states can be identified. Furthermore, the doping concentration can be estimated from simulation of the XRS spectrum. The spectrum has an energy resolution of about 0.5 eV. The peak induced from carbon contamination on the sample surface is always shown in the spectrum, and its energy position is usually used to calibrate the whole spectrum. The XPS instrument is also equipped with Ar gas ion gun sputtering, allowing depth profiling of peaks of interest in the XPS spectrum.

### 3.3.3 Rutherford backscattering spectrometry

The ZnO film stoichiometry, Sb-doping concentration, and depth-profiles were studied by a Rutherford backscattering spectrometry (RBS) system located at MIBL. A 1.7 MV Tandem Accelerator were used to create $\alpha$ particles ($^{4}_{2}\mathrm{He}^{2+}$) with high kinetic energies and to incident onto the sample surface. After elastic collision with the atoms in the sample, the backscattered $\alpha$ particles were measured by a semiconductor detector with a 5 millisteradian solid angle, producing the RBS spectrum of particle intensities vs. energies. The energy spectrum was thereby simulated using the SIMNRA software by M. Mayer *et al.*[149] to determine the Zn:O:Sb stoichiometry and the ZnO thin film thickness. The simulated stoichiometry has an error of about 0.03-0.05%. The thin film thickness is usually given in RBS number ($n_{\mathrm{RBS}}$) with units of $\times10^{15}$ atoms·cm$^{-2}$, thus the real thickness ($t$) is expressed as:

$$t = \frac{n_{\mathrm{RBS}} M}{N_{\mathrm{Av}} \rho Z} \tag{3.15}$$

where $M$ is the molar mass, $\rho$ is the density, Z is the atomic number of ZnO, and $N_{\mathrm{Av}}$ is Avogadro's number.

## 3.4 Electrical characterization

The electrical transport properties of the ZnO films were characterized by Hall effect measurements using the Van der Pauw configuration[150]. Figure 3.9 shows the preferred, acceptable, and not recommended sample geometries suggested by National Institute of Standards and Technology[151]. The configuration in Figure 3.9(b) with contact size of 0.25 $mm^2$ is employed in this study. For 5×5 $mm^2$ and 10×10 $mm^2$ samples, which are typically measured, the contact size induces about 5-10% relative error in Hall effect measurements. The contacts are made by pressing In dots on the sample surface, bonding with Au wires, and annealing at 300 °C in $N_2$ gas flow for 1 min. Linear dependence between current and voltage of the contacts are obtained prior to each measurement. Therefore, the contacts are assumed to be ohmic to ZnO thin films, and the contact resistance is neglected.

Other geometries proposed to improve the accuracy of the Hall effect measurements can be referred in the book of E. H. Putley *et al*.[152]

### 3.4.1 Room temperature Hall effect measurement

Room temperature Hall effect measurements were performed using two systems. The first one is an MMR H-50 Hall Measurement System equipped with a 0.64 T permanent magnet, supplied by IMRA America, Inc. The other one, employed as verification to the first system, is integrated with the cryostat of the photoluminescence (PL) characterization system (Section 3.5.2), and is accessorized with a 0.22 T permanent magnet, a Keithley 220 current source, and a Keithley 6517a high resistance meter.

The resistivity ($\rho$) is determined without a magnetic field ($B$=0) by measuring the voltages ($V_{ij}$) across two adjacent contacts while running currents ($I_{kl}$) through the other two contacts. The measurements are repeated eight times by rotating among the four contacts and reversing the direction of current each time. The resistivity is thus given by:[153]

$$\rho = R_S d = \frac{\pi d}{\ln 2}\frac{\overline{V_{ij}}}{I_{kl}} f, \quad (i, j, k, l = 1-4) \tag{3.16}$$

where $R_S$ is the sheet resistance, $d$ is the ZnO thin film thickness, and $f$ is a factor between 0 and 1 related to the sample geometry and can be found in Ref. 153. The average of

eight $\frac{V_{ij}}{I_{kl}}$ values eliminates potential errors caused by non-uniformity of the thin film and misalignment of the contacts.

During Hall voltage measurements, current runs diagonally through the sample (e.g. $I_{13}$) and voltage is measured across the other diagonal direction twice for $+B$ and $-B$ magnetic fields, respectively (e.g. $V_{24}^{+B}$, $V_{24}^{-B}$). The measurements are repeated four times by rotating the contacts and reversing the current direction. The voltage sum is given by $\sum(V_{ij}^{+B} - V_{ij}^{-B})$, where the combinations of $ij$ are 13, 31, 24, and 42. If the polarity of the voltage sum is positive, then the sample is $p$-type, whereas negative voltage sum indicates an $n$-type sample. Note that the plus-or-minus sign of the voltages are maintained during calculation to correct the zero-offset of the voltmeter. The carrier concentration ($n$) and Hall mobility ($\mu$) are calculated by:[151]

$$n = \frac{n_S}{d} = \frac{8\times10^{-8} IB}{ed} \frac{1}{\sum(V_{ij}^{+B} - V_{ij}^{-B})} \tag{3.17}$$

$$\mu = \frac{1}{e\rho n} \tag{3.18}$$

where $n_S$ is the sheet carrier density and $e$ is the elementary charge.

### 3.4.2 Temperature-dependent Hall effect measurement

Temperature-dependent Hall effect measurements were carried out using the cryostat of the PL system and the 0.22 T permanent magnet. Ten to fifteen temperatures between 10 K and 300 K were selected, and the measurements described in section 3.4.1 were performed at each steady temperature $T_k$ ($k$=1-15) to obtain the resistivities $\rho(T_k)$, carrier concentrations $n(T_k)$, and Hall mobilities $\mu(T_k)$. The information of multi-band conduction and scattering mechanisms in the thin films can be acquired from theoretical simulations of the temperature dependence of $n(T_k)$ and $\mu(T_k)$.

For heteroepitaxial ZnO thin films, the measured Hall effect data usually contain information of a degenerate interfacial layer that has temperature-independent electron concentration ($n_0$) and mobility ($\mu_0$), and that dominates the carrier transport at low

temperatures. In this case, the bulk electrical properties [ $n(T_k)'$ and $\mu(T_k)'$ ] of the ZnO films can be extracted from the measured two-layer properties by:[154]

$$\begin{cases} n(T_k)' = \dfrac{[\mu(T_k)n(T_k) - \mu_0 n_0 / d]^2}{\mu(T_k)^2 n(T_k) - \mu_0^2 n_0 / d} \\ \mu(T_k)' = \dfrac{\mu(T_k)^2 n(T_k) - \mu_0^2 n_0 / d}{\mu(T_k)n(T_k) - \mu_0 n_0 / d} \end{cases} \tag{3.19}$$

The temperature dependence of the carrier concentration can be fitted using the Charged Balance Equation (CBE):[155]

$$n + \sum_i N_{Ai}^- = p + \sum_i N_{Di}^+ \tag{3.20}$$

where $n$ and $p$ are the electron and hole concentrations, and $N_{Ai}^-$ and $N_{Di}^+$ are the concentrations of single-ionized acceptors and donors.

For ZnO there usually are multiple types of ionized impurity donors contributing to electrical transport. In this study we assume three donor bands and one residual acceptor band exist in undoped ZnO thin films, thus the CBE equation can be expressed as:[155]

$$n(T) + N_A = \sum_{i=1}^{3} \frac{N_{Di}}{1 + \dfrac{n}{\phi_i}} \tag{3.21}$$

where $\phi_i = g_{Di} N_C' T^{3/2} \exp(-E_{Di} / k_B T)$ . Here $N_{Di}$ and $E_{Di}$ are the concentration and activation energy of donor $i$ ($i$=1-3). The constant $g_{Di}$ is the ratio of unoccupied to occupied state degeneracies of donor $i$, and we assume $g_{Di}$=1/2 for an $s$-like donor state. $N_C'$ is the effective conduction-band density of states at 1 K, which is $8.66\times10^{14}$ cm$^{-3}$ for ZnO.[156] MATLAB code is developed for the three-band CBE simulation of $n(T)$ vs. $1/k_BT$ in Appendix B, taking $N_A$, $N_{Di}$, and $E_{Di}$ as fitting parameters.

The temperature dependence of the Hall mobilities is fitted by Matthiessen's rule:[155]

$$\frac{1}{\mu_{\text{total}}} = \frac{1}{\mu_{\text{pe}}} + \frac{1}{\mu_{\text{dp}}} + \frac{1}{\mu_{\text{po}}} + \frac{1}{\mu_{\text{ii}}} + \frac{1}{\mu_{\text{dis}}} \tag{3.22}$$

considering five principal scattering mechanisms as explained below.

The conduction electrons in undoped ZnO thin films can be scattered by acoustic phonons induced by lattice vibrations. Since ZnO is a piezoelectric material, the built-in longitudinal electric field disturbs the propagation of acoustic phonons. This perturbation then, affects the scattering of electrons. The piezoelectric potential induced mobility component ($\mu_{pe}$) is given by the following equation deduced by Hutson:[157]

$$\mu_{pe}(T) = 1.44 \frac{\varepsilon_0 \varepsilon_S}{K^2} \left( \frac{m_0}{m_e^*} \right)^{3/2} \left( \frac{300}{T} \right)^{1/2} \xrightarrow{\text{for ZnO}} 160 \left( \frac{m_0}{m_e^*} \right)^{3/2} \left( \frac{300}{T} \right)^{1/2} \tag{3.23}$$

where $K$ is the piezoelectric coupling coefficient ($K$=0.21 for ZnO), $\varepsilon_0$ and $\varepsilon_S$ are the vacuum permittivity and the relative static (low frequency) dielectric constant of ZnO ($\varepsilon_S$=8.12), and $m_0$ and $m_e^*$ are the free electron mass and the electron effective mass of ZnO ( $m_e^*$=0.318$m_0$).[156] The unit of $\mu_{pe}(T)$ in equation (3.23) is cm$^2$/V s.

The lattice vibrations change local band gaps in the films, creating a deformation potential to disturb the acoustic phonon scattering of the conduction electrons, thereby inducing the mobility component of $\mu_{dp}$:[155]

$$\mu_{dp}(T) = 10^4 \frac{\sqrt{8\pi}\hbar^4 \rho s^2 e}{3E_1^2 m_e^{*5/2} (k_B T)^{3/2}} \tag{3.24}$$

where $\hbar$ and $k_B$ are Plank constant and Boltzman constant, respectively. The deformation potential is $E_1$=15 eV. The mass density of ZnO is $\rho$=6.1×10$^3$ kg m$^{-3}$. The speed of sound in ZnO is $s$=6.59×10$^3$ m/s.[156] Note that $\mu_{dp}(T)$, together with the following mobility components, is multiplied by 10$^4$ to change the unit from m$^2$/V s to cm$^2$/V s, so that it matches the unit of $\mu_{pe}(T)$ and that of the experimental data.

The dipole moments formed by the interaction of the ionic charges of the atoms with the optical-mode lattice vibrations can also scatter the electrons, inducing the mobility component of polar optical phonon scattering ($\mu_{po}$) as calculated by C. Hammar and B. Magnusson:[158]

$$\mu_{po} = 10^4 \frac{4}{3E_0} \sqrt{\frac{2k_B T}{\pi m_e^*}} (e^z - 1) G(z) \tag{3.25}$$

$$E_0 = \frac{m_e^* e k_B \theta_D}{\varepsilon_0 \hbar^2} \left( \frac{1}{\varepsilon_\infty} - \frac{1}{\varepsilon_S} \right); \quad \text{and} \quad z = \frac{\theta_D}{T} \tag{3.26}$$

where $\varepsilon_\infty$ is the relative infinite (high frequency) dielectric constant of ZnO ($\varepsilon_\infty$=3.72) and $\theta_D$ is the Debye temperature of the optical modes ($\theta_D$=837-1000 K).[156] $G(z)$ is a correction factor of the order of unity,[158] and is taken as unity in our calculation. $G(z)$ has an approximated function expression reported in other calculations.[159,160]

The ionization of impurities in the ZnO films generates screened Coulomb potentials to scatter the electrons. The corresponding mobility component ($\mu_{ii}$) is:[155,161]

$$\mu_{ii} = 10^4 \frac{128\sqrt{2\pi}\varepsilon_S^2\varepsilon_0^2}{[2N_A + n(T)]Z^2e^3\sqrt{m_e^*}} \frac{(k_BT)^{3/2}}{[\ln(1+y) - y/(1+y)]} \quad (3.27)$$

$$y = \frac{24\varepsilon_S\varepsilon_0 m_e^*(k_BT)^2}{\hbar^2e^2n(T)} \quad (3.28)$$

where $Z$ is the number of the ionic charge of the impurity assumed to be unity, and $2N_A+n(T)$ is the total density of ionized impurities assuming all acceptors are ionized in the $n$-type ZnO.[162]

Charged dislocation lines in the epitaxial ZnO films also act as Coulomb scattering centers. Weimann *et al.*[163] calculated the corresponding mobility component ($\mu_{dis}$) to be:

$$\mu_{dis} = \frac{\hbar^3c^2\varepsilon_S^2\varepsilon_0^2}{e^3f^2m_e^{*2}N_{dis}\lambda_D^4}\left(1+4k_\perp^2\lambda_D^2\right)^{3/2} = \frac{\hbar^3ec^2n^2(T)}{N_{dis}m_e^{*2}(k_BT)^2}\left(1+\frac{8\varepsilon_S\varepsilon_0m_e^*(k_BT)^2}{e^2\hbar^2n(T)}\right)^{3/2} \quad (3.29)$$

where $N_{dis}$ is the dislocation density, $c$ is the lattice parameter along [0001] direction, $\lambda_D = \left(\frac{\varepsilon_S\varepsilon_0k_BT}{e^2n(T)}\right)^{1/2}$ is the screening Debye length, $k_\perp$ is the scattering wave vector with a magnitude approximately equals $\sqrt{\frac{2m_e^*k_BT}{\hbar^2}}$, and $f$ is the fraction of filled traps, ideally unity.[164]

The total Hall mobility ($\mu_{total}$) is fitted vs. $T$ including all the five scattering mechanisms, taking $N_A$, $N_{dis}$, and $\theta_D$ as fitting parameters, and employing the CBE fitted $n(T)$ values. Corresponding MATLAB code is included in Appendix B.

### 3.4.3 I-V characterization of junction samples

For the ZnO films grown on (111) Si substrates with bixbyite oxide buffer layers, the current-voltage characteristics of *p*(Si)-*i*($M_2O_3$)-*n*(ZnO) junction structures were measured using a HP 4156 Precision Semiconductor Parameter Analyzer and probe stations. For most of the samples, the top and bottom contacts are made of pressed and annealed In dots bonded with Au wires. For a few samples, $300\times300\ \mu m^2$ masked contacts of Ti (7 nm) and Au (10 nm) double layers were sputtered on the ZnO films by Brandon Choi from EECS.

## 3.5 Optical characterization

### 3.5.1 Transmittance

Since the $Al_2O_3$ substrates we used are double-side polished, we were able to measure room temperature optical transmittance spectra of the ZnO films grown on $Al_2O_3$ substrates by the Varian 50Bio UV-Spectrophotometer located in the Van Vlack Undergraduate Laboratory. The scan range was from 190 nm to 1000 nm. All transmittance spectra were base-line corrected instantly after measurements according to a transmittance spectrum of a bare $Al_2O_3$ substrate. The absorption edge in the spectra indicates the optical band gap of the ZnO films. The band gap ($E_g$) can be accurately determined by drawing the Tauc plot[165] of:

$$\begin{cases} (\alpha h\nu)^2 \ vs.\ h\nu \quad \text{for determining the direct band gap} \\ (\alpha h\nu)^{1/2} \ vs.\ h\nu \quad \text{for determining the indirect band gap} \end{cases} \tag{3.30}$$

and extrapolating the absorption edge to the $h\nu$ axis, since $\alpha h\nu \sim (h\nu - E_g)^2$. Here the absorption coefficient is determined by: $\alpha \sim -\log T$ , where $T$ is the transmittance intensity. $h\nu$ is the corresponding photon energy. The shift of the optical band gap with respect to Sb-doping concentration was studied in Chapter 6.

### 3.5.2 Photoluminescence

Temperature-dependent photoluminescence (PL) measurements were made using a Kimmon IK3501RG He-Cd laser ($\lambda$=325 nm) incident on the sample surface, and the luminescence excited from the sample was collected by a HORIBA Jobin-Yvon 1000M

monochromator (1 m in length) operating between 350 and 800 nm. The sample was mounted by conductive copper tape onto a cold finger holder of close-cycle cryostat. The temperature of the cold finger holder can be cooled down to 10 K by a He gas compressor. The optical signals collected by the monochromator were transferred to electrical signals by a photon counting photomultiplier (PMT) tube operated at 950 V. The monochromator entrance and exit slit widths were selected to be between 10 and 400 μm depending on the sample characteristics and/or the PMT saturation limit ($10^7$ cps). The monochromator scan speed was 1 Å/step, and the integration time was 1 s/step. The highest resolution can reach to 0.1 Å/step. Three filters were inserted in the laser and signal beams to filter radiation around the laser wavelength and also to allow changing of the incident laser power. A schematic of the PL system setup is shown in Figure 3.10.

During PL measurements, the incident laser power was absorbed near the sample surface region, generating excitons, *i.e.* electron hole pairs, which immediately recombined and released photons carrying the energies dependent on both the band gap and the donors/acceptors of the sample materials. Therefore, PL is a powerful tool to determine the exciton fine structures and the impurities in the sample as well as the crystalline quality. The characteristic luminescence lines measured in the near-band-edge region of the ZnO PL spectra usually include:

(1) Free exciton recombination from the conduction band to the valance band (band gap transition), generally denoted by FX.[166] The valance band is split by crystal field and spin orbit interaction into three states named A, B, and C. Each state can have transverse and longitudinal polarization characteristics.[167] Therefore, the free exciton recombination observed in PL spectra of high quality bulk crystals includes fine details of the ground states (*n*=1) and the first excited states (*n*=2) transition lines of the three excitons, labeled $A_T^{n=1}$, $A_L^{n=1}$, $B_T^{n=1}$, $B_L^{n=1}$, and $A_L^{n=2}$ etc. in this study. The luminescence line width of free exciton recombination can be as narrow as 40 μeV for high quality bulk ZnO crystals.[167]

(2) Ionized donor bound exciton recombination, which is a bound exciton complex composed of an intrinsic exciton (an electron-hole pair) molecularly bound to an ionized center, sometimes denoted by $D^+X$. The ionized center is usually a donor center, because ionized acceptors are energetically unfavorable to bind with excitons. A few

ionized donor bound exciton recombination lines, distinguished as lines $I_0$-$I_3$, are usually recognized in the ZnO PL spectra, with small exciton-to-ionized-center binding energy (<0.01 eV).[168]

(3) Neutral donor/acceptor bound exciton recombination, also known as $D^0X/A^0X$ or BX, is a bound exciton complex composed of a free A or B exciton bound to neutral defect centers, which are either donor-like or acceptor-like, such as impurities or point defects. After recombination, the neutral defect returns to its 1*s* state. Much research has been devoted to identifying the physical nature of the several observed recombination lines of neutral donor bound excitons, from $I_4$ to $I_{11}$, as well as a few Y-lines induced by structural defects.[167,168] So far, neutral donors induced by H, Al, Ga, In, and other chemical impurities have been proposed.[167] The exciton-to-neutral-donor binding energy, also known as the localization energy ($E_{\mathrm{loc}}$), is related to the ground state donor-bound exciton energy ($E_{\mathrm{DX}}$) and the ground state free exciton energy ($E_{\mathrm{FX}}$) by:

$$E_{\mathrm{loc}} = E_{\mathrm{FX}} - E_{\mathrm{DX}} \tag{3.31}$$

(4) Two-electron satellite recombination (TES), which is also a neutral donor bound exciton transition line. The difference in this recombination is that, the donor final state after recombination is in the excited states (2*s*, 2*p*). The TES line appears at the lower energy side of the corresponding $D^0X$ line. In temperature-dependent PL spectra, it evolves in the same trend as the corresponding $D^0X$ line. The energies difference between the TES line and the $D^0X$ line ($E_{\mathrm{DX}}$-$E_{\mathrm{TES}}$) is important in determining the neutral donor binding energy ($E_{\mathrm{D}}$), since in hydrogen approach:

$$E_{\mathrm{DX}}^{n_1=1} - E_{\mathrm{TES}}^{n_2=2} = \left(\frac{1}{n_1^2} - \frac{1}{n_2^2}\right)E_{\mathrm{D}} = \frac{3}{4}E_{\mathrm{D}} \tag{3.32}$$

(5) Longitudinal optical phonon replicas (LO phonons), due to multiple phonons being created during the free or the donor bound exciton recombination's. LO phonon lines observed in PL spectra are usually weak, and they appear at the lower energy side of the free and donor bound excitons. The LO photons of ZnO have energy separations of 71-73 meV due to the LO phonon frequency of 591 $cm^{-1}$ in ZnO.[169]

For detailed information of acceptor related recombination lines, and temperature-dependent and power-dependent PL spectra analysis, please refer to the Ph.D. thesis[170] of A. Allenic.

### 3.5.3 Electroluminescence

For the *p*-*i*-*n* junction of ZnO films grown on (111) p-Si substrates with bixbyite oxide buffer layers, temperature-dependent EL measurements were made using the PL system without the pumping laser. The sample was fixed on the cold finger holder by electrical insulating tape. The top and bottom contacts on the sample were annealed In dots bonded with Au wires. Current was supplied to the sample by an external Keithley 220 current source. The maximum current was limited 100 mA to avoid contact melting induced by overheating of the sample.

When applying forward bias to the sample, holes were supposed to be driven from *p*-Si into the ZnO film, and to recombine with electrons and emit photons. The electroluminescence between 350 nm and 800 nm was collected by the 1000M monochromator with a slit width of 3 mm, an acquisition time of 1s/step, and a scan speed of 10 Å/step. The measurement room was maintained completely dark during measurements.

A Konica Minolta 7D DSLR camera equipped with a fixed focal length 50 mm lens was used to take photographs of the luminous samples. The aperture size was f/8. The maximum exposure time I used is 30 s.

Table 3.1 Substrates and targets used in my study for ZnO growth.

| Substrates | Targets and raw materials | |
|---|---|---|
| (111) $Sc_2O_3$/(111) Si | ZnO (99.999%) | Commercial |
| (111) $Lu_2O_3$/(111) Si | 0.1-1.0 at.% Sb-ZnO | ZnO + $Sb_2O_3$ |
| (111) $Gd_2O_3$/(111) Si | 10 at.% N-ZnO | ZnO + $Zn_3N_2$ |
| $SiO_2$/(100) Si | 5 at.% Bi-ZnO | ZnO + $Bi_2O_3$ |
| (0001) ZnO | 1 at.% P-ZnO | ZnO + $P_2O_5$ or $Zn_3P_2$ |
| (0001) $Al_2O_3$ | 0.1 at.% P-$Zn_{0.8}Mg_{0.2}O$ | ZnO + $P_2O_5$ + MgO |
| $(10\bar{1}2)$ $Al_2O_3$ | 10 at.% Mg-ZnO | Commercial |
| (111) Y-$ZrO_2$ (YSZ) | 3 at.% Al-ZnO | Commercial |
| (100) $SrTiO_3$ | 3 at.% Ga-ZnO | Commercial |
| (100) $LiAlO_2$ | 5 at.% Mn-ZnO | Commercial |
| | 0.5 at.% P-ZnO | Commercial |
| | 10 at.% In-$SnO_2$ (ITO) | Commercial |

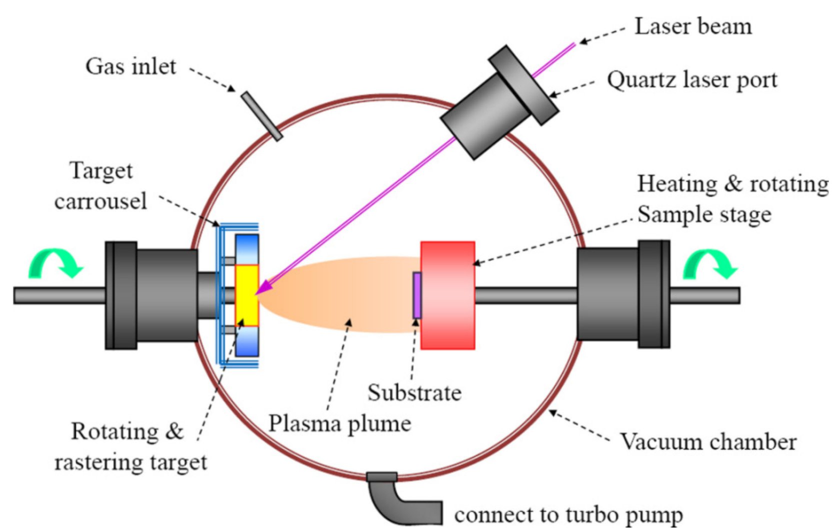


Figure 3.1 Schematic of a typical PLD system

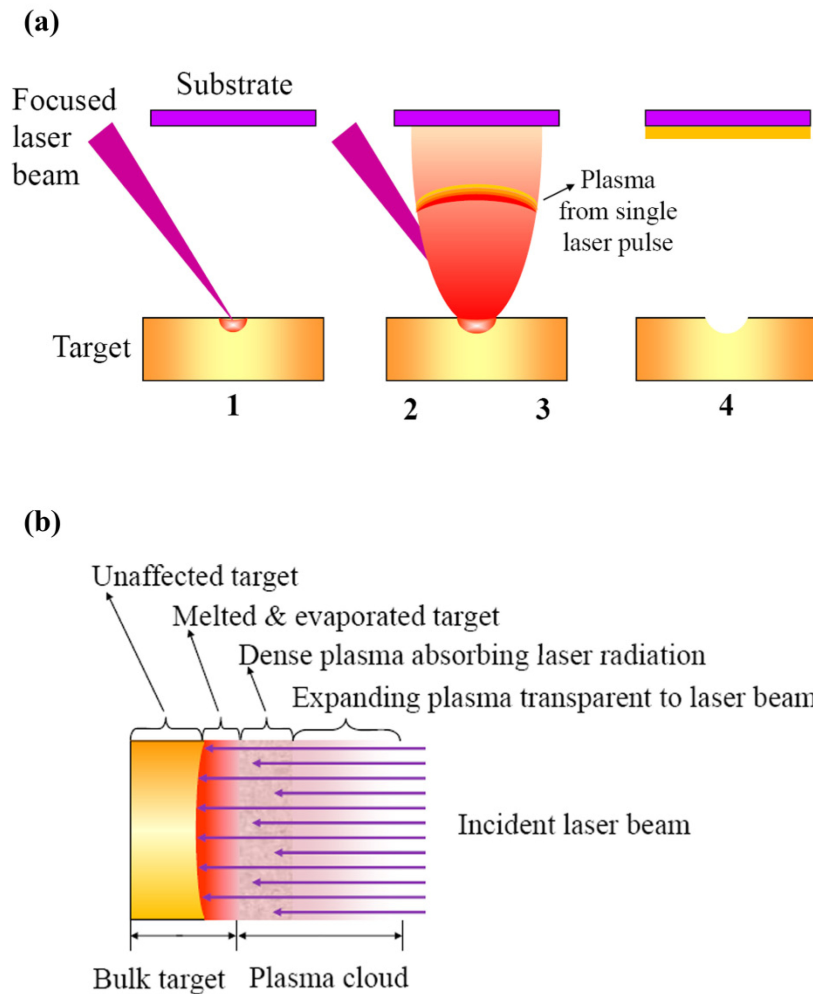


Figure 3.2 Schematics showing (a) the four dynamic processes of laser-plasma-solid interactions in PLD technique, and (b) a close look of the interactions between the plasma plume and the laser radiation.

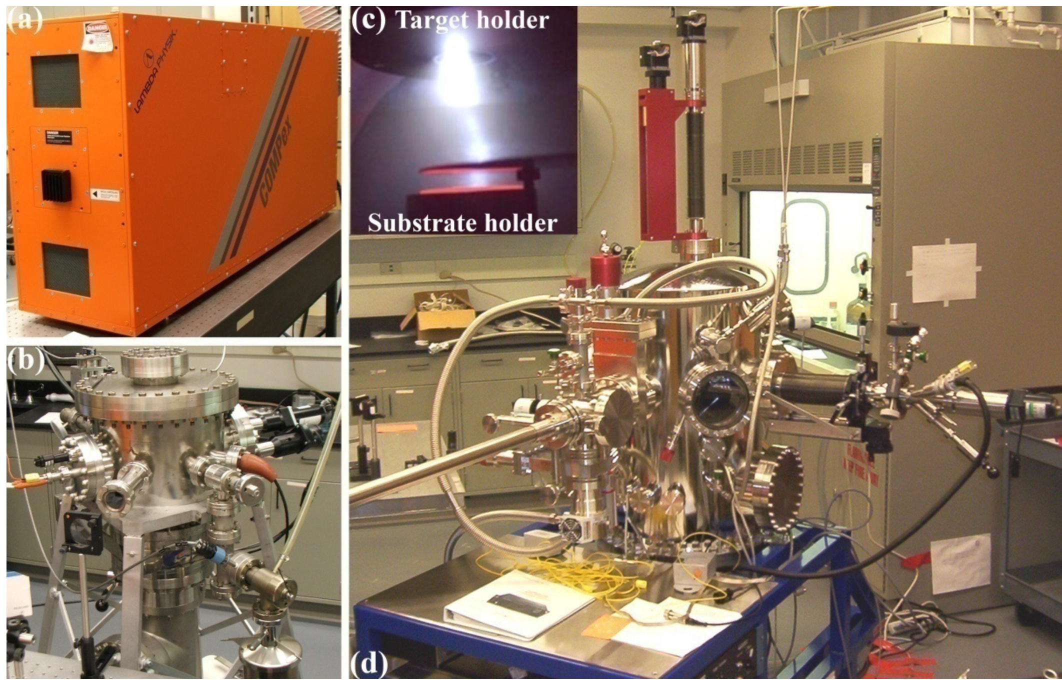


Figure 3.3 Photographs of (a) the excimer laser, (b) the Neocera PLD system, (c) the plasma plume, and (d) the Thermionics PLD system.

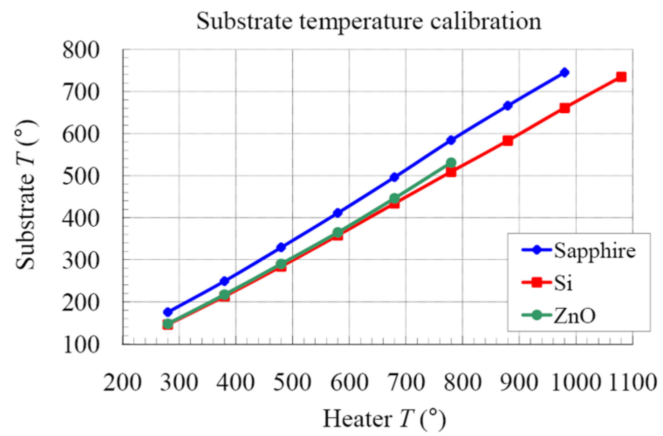


Figure 3.4 Calibration of the substrate temperature vs. the heater temperature in the Thermionics system.

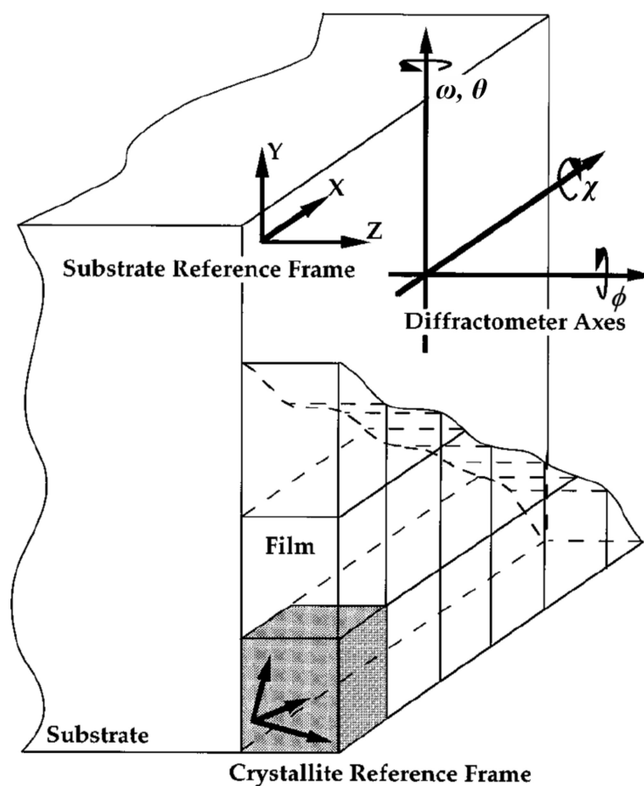


Figure 3.5 Schematic showing the relationship between the diffractometer axes and the substrate reference frame in XRD measurement. (modified from V. Srikant *et al.* [142])

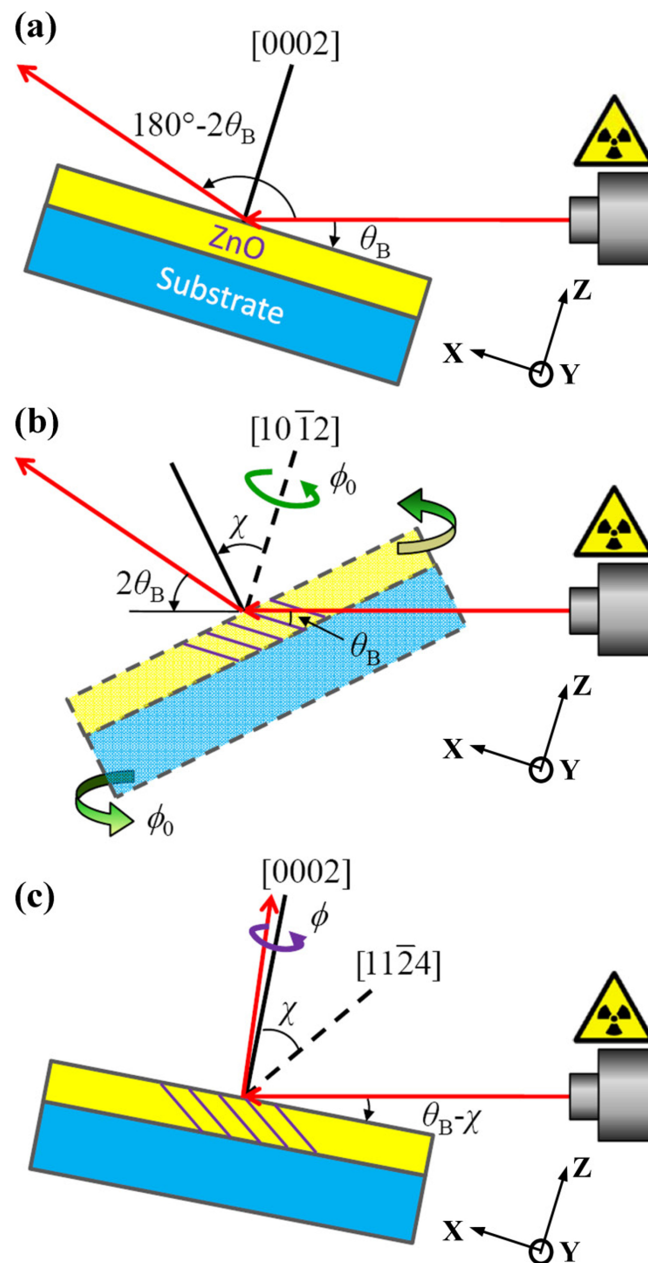


Figure 3.6 Schematics showing (a) symmetric, (b) skew symmetric, and (c) glancing incidence asymmetric XRD geometries used to measure the $\omega$-scans of ZnO 0002 and $10\bar{1}2$ and the $\phi$-scan of ZnO $11\bar{2}4$ reflections, respectively.

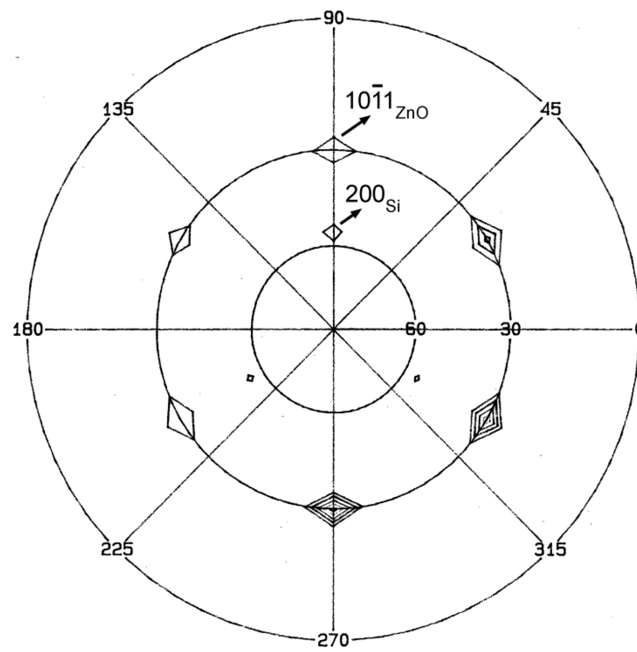


Figure 3.7 Pole figure of ZnO grown on (111) Si with bixbyite oxide buffer layer.

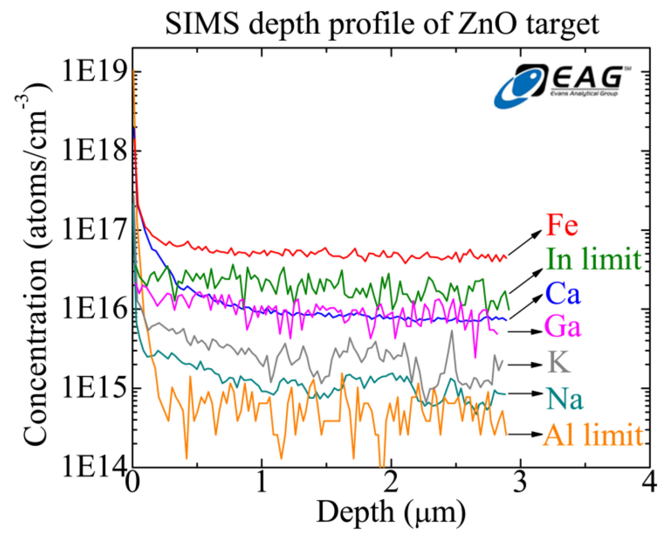


Figure 3.8 SIMS depth profile of impurities in a commercial ZnO target.

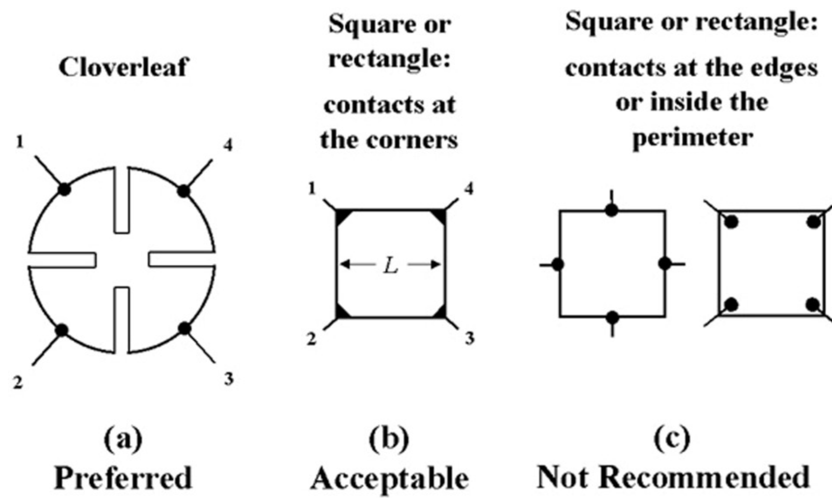


Figure 3.9 Commonly used Van der Pauw configurations of Hall effect measurements. (from NIST [151]) The configuration used in this study is (b).

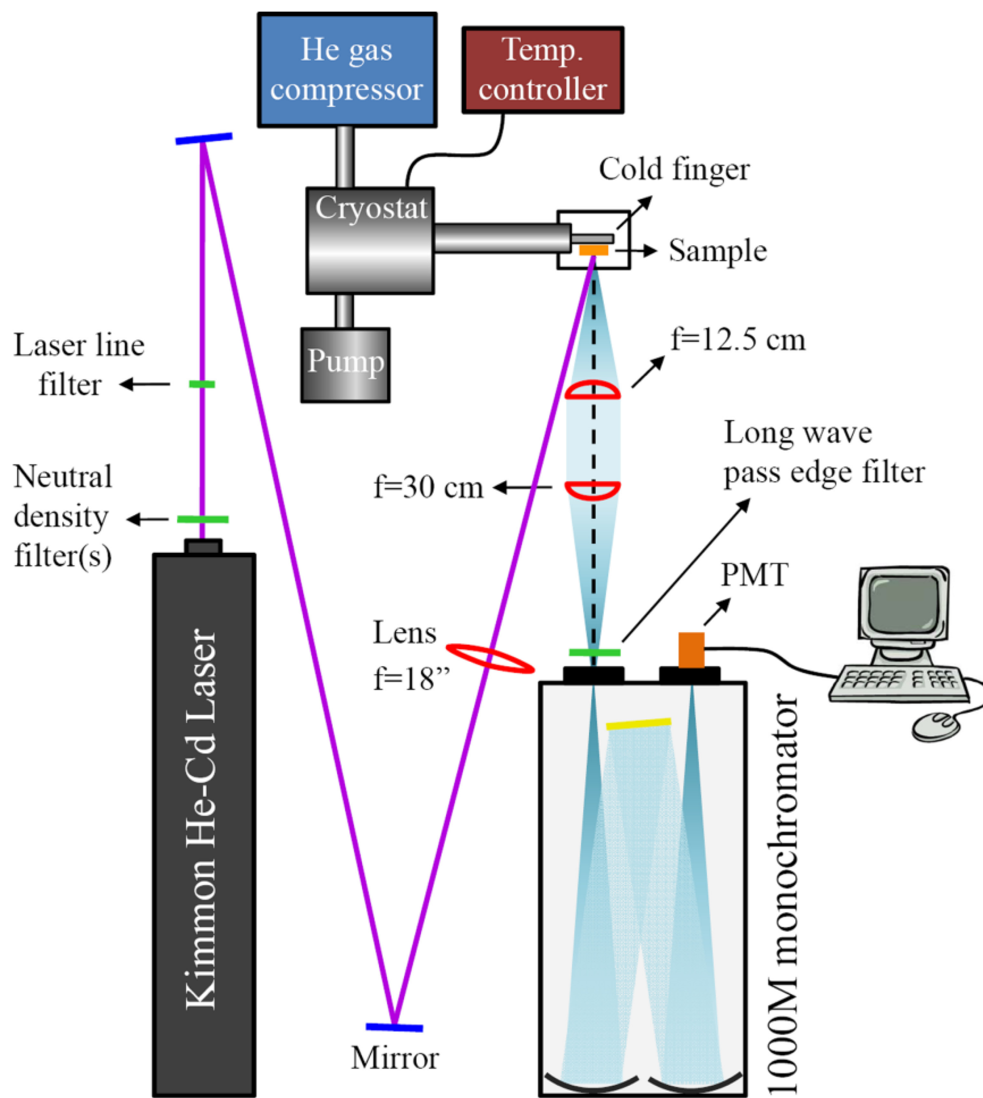


Figure 3.10 Schematic of the PL system setup (not drawn to scale)

# Chapter 4

# Epitaxy and Properties of ZnO Thin Films Grown on (111) Si Using Bixbyite Oxide Buffer Layers

In Chapter 2, we have reviewed all current reports of ZnO growth on Si, and have made the point that ZnO can not be grown epitaxially on (100) Si, and single-crystalline ZnO films can only be synthesized on (111) Si substrates with the use of proper buffer layers. In Table 2.1, the ZnO films I grew on $Sc_2O_3$, $Lu_2O_3$, and $Gd_2O_3$ bixbyite buffer layers have the smallest 0002 $\omega$-FWHM values among all the reports of ZnO epitaxy on (111) Si. Though there is one comparable $\omega$-FWHM value of 0.114° reported for ZnO film on AlN buffer, that ZnO film is twice as thick as those grown on bixbyite oxide buffer layers. Since the FWHM measured in XRD narrows when the film thickness increases, if we compare the ZnO films of the same thickness, the films grown on bixbyite oxide buffer layers should have better crystallinity than those on AlN buffer layers. In the following chapter, we provide a detailed report of the physical properties of the ZnO films grown on Si with bixbyite oxide buffer layers, including crystallinity, microstructure, and electrical and optical properties, to demonstrate that these properties are superior to all current reports of ZnO growth on Si.

## 4.1 Properties of the bixbyite oxide buffer layers

Bixbyite oxides $M_2O_3$ ($M$=Sc, Lu, Y, Gd) are high-$\kappa$ dielectric materials that are of interest for implementation as the next generation of epitaxial gate insulators for the ultimate scaling of Si-based MOSFET technology. These oxides are electrically

insulating and appear to be thermodynamically stable on Si without reactions with Si.[20] Figure 4.1(a) shows the unit cell of bixbyite oxide (space group $Ia\overline{3}$), which contains 14 distorted octahedral cells in one body-centered large lattice. The bixbyite oxide has atomic positions of $M_1$ on 8*b* sites, $M_2$ on 24*d* sites with internal parameter *u*, and O on 48*e* sites with internal parameters *x*, *y*, and *z*. The enthalpies of formation, lattice constants, and internal parameters of these bixbyite oxides are listed in Table 4.1.

Figure 4.1(b) shows schematics of the atomic arrangements for the (111) surface of Si, the (111) surface of $M_2O_3$, and the (0001) surface of ZnO. It is clearly illustrated how the atoms in the three layers overlap with each other when ZnO is grown on $M_2O_3$ on (111) Si. The lattice mismatches between Si and $M_2O_3$ are calculated from $(a_{\mathrm{Si}} - \frac{1}{2} a_{M_2\mathrm{O}_3}) / a_{\mathrm{Si}}$. The lattice mismatch between $M_2O_3$ and ZnO can be calculated from $(\frac{\sqrt{2}}{2} a_{M_2\mathrm{O}_3} - a_{ZnO}) / (\frac{\sqrt{2}}{2} a_{M_2\mathrm{O}_3})$ along the $[1\overline{1}0]$ direction of Si. The lattice mismatch values for the four bixbyite oxides $M_2O_3$ (*M*=Sc, Lu, Y, Gd) are listed in Table 2.1.

It has been reported that bixbyite oxides $Y_2O_3$ and $Sc_2O_3$ grown on (111) Si have two (111)-oriented domain structures, the A-type and B-type domains, which are distinguished by an in-plane rotation of 180°.[111,171,172] Typically, the A-type domain $M_2O_3$ film grown on (111) Si has an in-plane orientation relationship of $[1\overline{1}0]_{M_2\mathrm{O}_3} \| [1\overline{1}0]_{\mathrm{Si}}$, while the B-type domain film has a relationship of $[\overline{1}10]_{M_2\mathrm{O}_3} \| [1\overline{1}0]_{\mathrm{Si}}$. As seen from the $\phi$-scan of $Y_2O_3$ 440 peaks in Figure 2.11(d), the A-type domain is represented by a set of three-fold symmetric peaks with low intensity and identical $\phi$ angles as those of the Si 220 peaks; while the B-type domain is represented by the other set of high intensity peaks with 180° shift from the Si 220 peaks. Generally, the $Y_2O_3$ and $Sc_2O_3$ films grown on (111) Si have the double-domain twin structure with dominating B-type domains.

In this work, epitaxial growth of $M_2O_3$ (*M*=Sc, Lu, Gd) films were performed by researchers in Prof. Darrell G. Schlom's group on 3-inch (111) *p*-Si wafers ($\rho$>50 Ω cm) using reactive MBE. The Si wafer was etched by HF acid prior to loading to remove $SiO_2$ on the surface, and then it was heated in vacuum up to 950 °C for desorption prior to growth. There was no residual native oxide on the Si surface. The epitaxial $M_2O_3$ films were grown at a substrate temperature of 700 °C by exposing the Si substrate to a *M* flux in oxygen background. Several film thicknesses (30 nm, 60 nm, and 100 nm) were used.

The typical $\omega$-FWHM value of $Lu_2O_3$ 222 reflections measured by XRD for a 30 nm thick $Lu_2O_3$ film is only 0.0025° (9 arc sec), suggesting the $Lu_2O_3$ films are of high crystalline quality. $Sc_2O_3$ films with the same thickness have a larger $\omega$-FWHM value of 0.06°. For $Gd_2O_3$ films, because the lattice constant $\frac{1}{2}a_{Gd_2O_3}$ is too close to $a_{Si}$, we can only measure the $Gd_2O_3$ 444 $\omega$-rocking curve in order to avoid the ambiguity caused by strong Si 222 signals in the $Gd_2O_3$ 222 $\omega$-scan. The average $\omega$-FWHM value of $Gd_2O_3$ 444 reflections is 1.27°, indicating poorer crystallinity than the other two bixbyite films.

The $\phi$-scans of $M_2O_3$ 211 peaks in Figure 4.2 show that the $Sc_2O_3$ film on Si has the twin structure with A-type domains less than 5%, whereas the $Lu_2O_3$ and $Gd_2O_3$ films contain almost exclusively B-type domains. It is worthy to note that the 211 reflection is selected for $\phi$-scans instead of the 440 reflection in order to avoid the ambiguity from strong Si 440 signals. A Si 220 $\phi$-scan is compared in Figure 4.2 to clarify the B-type domain orientation relationship, since the overlapping between $M_2O_3$ 211 signals and Si 220 signals indicates a 180° rotation between $M_2O_3$ {220} and Si {220}.

The HRTEM images of $Sc_2O_3$/Si interface in Figure 4.3 clearly visualize the B-type domain orientation relationship of $(111)[\bar{1}10]_{M_2O_3} \| (111)[1\bar{1}0]_{Si}$. As seen in Figure 4.3(a), the $M_2O_3$ film has an atomically sharp interface on Si with no $SiO_x$ layer. This result is in agreement with the high enthalpies of formation of $M_2O_3$ (Table 4.1), suggesting that the bixbyite oxides have good thermodynamic stability on Si and impede the Si surface oxidation. The periodic interfacial misfit dislocations marked in Figure 4.3(b) indicate a domain matching relationship of 9-10 Si unit cells matching 10-11 $Sc_2O_3$ unit cells.

In addition to the structural characterizations above, we have also examined 4-probe resistivity measurements (Section 3.4.1) on the $M_2O_3$ films and confirmed they were electrically insulating.

To summarize this section, the bixbyite oxide buffer layers grown by MBE on (111) Si substrates are insulating and of high crystallinity, and have sharp and oxide-free interface on Si. The $Lu_2O_3$ and $Gd_2O_3$ films have nearly exclusively B-type domains, whereas the $Sc_2O_3$ film contain <5% A-type twin domains. These properties, together

with the relatively small lattice mismatches to ZnO and to Si, make bixbyite oxides the potential buffer layers for epitaxial growth of ZnO on Si.

### 4.2 Crystallinity of the epitaxial ZnO films grown on $M_2O_3$/Si

The Thermionics PLD system was used to fabricate epitaxial ZnO films on the bixbyite oxide buffered (111) Si substrates. The laser conditions are described in Section 3.1.2. After the $M_2O_3$/Si substrate was transferred into the PLD chamber, the growth of a nucleation ZnO layer (*nu-ZnO*) of about 10 nm nominal thickness was first initiated at 240 °C. Then the substrate temperature was raised to 600 °C for the main ZnO film growth. The ZnO film thickness ranges from 300 nm to 2 μm. The deposition rate was estimated to be 0.3 Å/pulse at a substrate temperature of 600 °C. During the ZnO growth, the chamber was backfilled with $6.7\times10^{-3}$ mbar (5 mTorr) $O_2$. In the following part of this chapter, unless specially stated, all the terms of "ZnO films" denote the 600 °C grown films with 240 °C grown nu-ZnO layers.

Figure 4.4(a) shows typical XRD $\theta$-$2\theta$ scans of the ZnO films grown on the three $M_2O_3$/Si substrates. The 111 series of $M_2O_3$ and Si peaks and the 0001 series of ZnO peaks are clearly seen. No impurity or polycrystalline peaks are detected. The out-of-plane orientation relationship is determined to be $(0001)_{\mathrm{ZnO}}||(111)_{M_2\mathrm{O}_3}||(111)_{\mathrm{Si}}$ from Figure 4.4(a). Figure 4.4(b) shows that, in the enlarged $\theta$-$2\theta$ scans, the $M_2O_3$ 222 peaks were superimposed by Kiessig interference fringes[173], indicating highly ordered crystalline structure and thickness homogeneity of the $M_2O_3$ layers. The thicknesses of the $M_2O_3$ layers, 30 nm or 60 nm in these samples, are calculated from the $2\theta$ fringe spacing: $t \approx \lambda_{\mathrm{Cuk}\alpha}/\Delta 2\theta$. Figure 4.4(c) shows typical $\phi$-scans of ZnO $11\bar{2}4$ and Si 440 peaks, from which an in-plane orientation relationship of $[1\bar{2}10]_{\mathrm{ZnO}}||[\bar{1}10]_{M_2\mathrm{O}_3}||[1\bar{1}0]_{\mathrm{Si}}$ is obtained, corroborating with the pole figure in Figure 3.7 and the prediction in Figure 4.1(b).

The mosaic misorientation of the ZnO epilayers was first quantified by XRD $\omega$-rocking curve measurements. The broadening, i.e. $\omega$-FWHM, of ZnO 0002 and $10\bar{1}2$ $\omega$-rocking curves was measured according to Figure 3.6, for judging the out-of-plane and in-plane components of the mosaic misorientation, respectively. Figure 4.5(a) shows the

0002 and $10\bar{1}2$ $\omega$-rocking curves for a 1 μm thick ZnO film grown on 100 nm $Sc_2O_3$/Si, with small $\omega$-FWHM values of 0.084° and 0.112° respectively. These small values indicate only a few slightly misoriented crystallites within the epitaxial films. These $\omega$-FWHM values, together with those reported for ZnO epitaxy on Si using other buffer layers (Table 2.1), are plotted in Figure 4.5(b) and compared to the values obtained from a 1 μm thick ZnO film grown on the traditional *c*-plane $Al_2O_3$ substrate. In particular, the film on *c*-$Al_2O_3$ was grown in the same chamber and under the same conditions as the films on $M_2O_3$/Si. It is seen that the three films on $M_2O_3$/Si have smaller 0002 $\omega$-FWHM values (squares, 0.08°~0.11°) than other films, and the values are comparable to that of the film on *c*-$Al_2O_3$ (0.09°). For the $10\bar{1}2$ $\omega$-FWHM values (circles), not all reports contain such information, yet the values measured for the films on $M_2O_3$/Si (≤ 0.16°) are only half of those reported for the films of ZnO/AlN/Si (0.31°) and ZnO/$Al_2O_3$ (0.36°). We conclude from Figure 4.5(b) that the ZnO/$M_2O_3$/Si films have superior crystalline quality than all other ZnO films grown on Si. And the crystalline quality is also better than that of the ZnO film grown on *c*-$Al_2O_3$.

In order to have a deeper understanding of the mosaic nature of the epitaxial ZnO films, high resolution triple-axis XRD measurements described in Section 3.2.2.5 was performed to determine the two crystallographic parameters: the tilt angle ($\alpha_\Omega$) of the subgrains with respect to the substrate normal and their in-plane twist angle ($\alpha_\Phi$), representing the azimuthal rotation around the substrate normal.[142] Here we use a 1 μm thick ZnO film grown on 100 nm $Sc_2O_3$/Si as an example. Figure 4.5(c) is a Williamson-Hall plot[140] of the $\omega$-FWHM values of ZnO 0001 series rocking curves measured from the film. The slope of the linear fitting gives a small tilt angle of $\alpha_\Omega$=0.05°. We also measured the $\omega$-rocking curves of off-axis reflections such as $10\bar{1}l$ ($l$=1-5) reflections in skew symmetric geometry, and plotted the $\omega$-FWHM values against the inclination angles ($\chi$) of the sample in Figure 4.5(d). The plot is then fitted using the Srikant method[142] combining Equations 3.5~3.9. The extrapolation of the fitting to $\chi$=90° gives an estimation of the twist angle ($\alpha_\Phi$=0.11°). The tilt and twist angles of the ZnO/100 nm $Sc_2O_3$/Si film are so far the smallest in all the reports of ZnO grown on Si. The angles measured for certain ZnO/$M_2O_3$/Si films and for the ZnO/*c*-$Al_2O_3$ film are listed in Table

4.2. It is worthy to note that all the angles are smaller than those reported in Ref. 111 for the ZnO film grown on $Y_2O_3$/Si ($\alpha_\Omega$=0.27° and $\alpha_\Phi$=0.52°).

A primary measure of thin film's microcrystallinity is its defect density. From $\alpha_\Omega$ and $\alpha_\Phi$ we can further derive the approximate values of the film's threading dislocation densities using equations 3.10. The $c$-type dislocations, which are mostly dislocations with a screw component (Burgers vector **b**=<0001>), are corresponding to the tilt of the subgrains. And thus the density can be estimated as $N_c \approx \alpha_\Omega^2 / 4.35 b_c^2$, where $b_c = c_{ZnO}$=5.2066 Å. On the other hand, the $a$-type dislocations, which are mostly edge dislocations (**b**=$\frac{1}{3}\langle 11\bar{2}0 \rangle$), are corresponding to the twist of the subgrains. Therefore, the density is $N_a \approx \alpha_\Phi^2 / 4.35 b_a^2$, where $b_a = a_{ZnO}$=3.2498 Å. The estimated $N_c$ and $N_a$ for our ZnO films are listed in Table 4.2.

In ZnO, most threading dislocations are either edge or mixed-type, due to a lower nucleation energy of edge dislocations than that of screw dislocations. This idea is in agreement with the fact that the value of $N_a$ is always larger than that of $N_c$ in Table 4.2, notably 5 to 50 times larger. Comparing the $N_a$ values of the ZnO films on 30 nm $M_2O_3$/Si and that of the film on $Al_2O_3$, the film on $Gd_2O_3$/Si has similar value ($10^{10}$ cm$^{-2}$) to that of the film on $Al_2O_3$, whereas the films on $Lu_2O_3$/Si and $Sc_2O_3$/Si have smaller values ($10^9$ cm$^{-2}$) than that of the film on $Al_2O_3$, up to one order of magnitude less. This is probably due to a smaller lattice mismatch to ZnO and a better crystallinity of the $Lu_2O_3$ and $Sc_2O_3$ films than those of the $Gd_2O_3$ film. And this is also in agreement with the $\omega$-FWHM difference of the three $M_2O_3$ layers described in Section 4.1.

The dislocation densities can be further reduced by increasing the thicknesses of the $M_2O_3$ buffer layers. For example, Table 4.2 shows that a ZnO film on 100 nm $Sc_2O_3$/Si has smaller dislocation densities than those of the film on 30 nm $Sc_2O_3$/Si. The reduction of dislocation densities in the ZnO film upon increasing of $M_2O_3$ thickness probably results from the crystallinity difference of the $M_2O_3$ buffer layers. The thicker the $M_2O_3$ buffer layer, the less is the defect density at its surface. Thus, there is less dislocations propagate into the ZnO films when the $M_2O_3$ buffer layer is grown thicker.

The bottom part of Table 4.2 shows the dislocation density difference between the ZnO films grown with and without the nu-ZnO nucleation layer. The films grown on 60

nm $Gd_2O_3$/Si are taken as an example. Similar features have been observed in the films grown on other $M_2O_3$/Si substrates. In Table 4.2, $N_a$ is reduced from $4.8\times10^9$ cm$^{-2}$ to $5.4\times10^8$ cm$^{-2}$ when the nu-ZnO layer is incorporated in the ZnO growth on $Gd_2O_3$/Si. The effect of nu-ZnO layer is similar to the LT-ZnO layer discussed in Section 2.2, which has been used as a buffer layer for ZnO growth on Si. Since the migrations and interactions of dislocations occur during the growth of the nu-ZnO layer, most of the dislocations annihilate internally, and thus do not penetrate through the nu-ZnO layer during the second stage of the thick ZnO film growth. Therefore, the films with the nu-ZnO layers usually have less dislocation densities than the ones without the nu-ZnO layers.

Briefly summarizing the crystallinity of the ZnO/$M_2O_3$/Si films here, the $\omega$-FWHMs, tilt and twist angles, and dislocation densities of the ZnO/$M_2O_3$/Si films are either comparable to or smaller than those of the ZnO/$Al_2O_3$ film grown under the same conditions, and they are also smaller than the values currently reported for all other ZnO/Si films. The density of *a*-type dislocations is 5-50 times larger than that of *c*-type dislocations. The dislocation densities can be further reduced by increasing the $M_2O_3$ layer thicknesses. The nu-ZnO layer shows significant effect on suppressing the dislocations.

### 4.3 Microstructures and defects of the epitaxial ZnO films on $M_2O_3$/Si

The microstructures of the ZnO films grown on bixbyite oxide buffer layers were imaged by a JEOL 3011F HRTEM operated at 300 kV. The TEM specimens were cut along the $[10\bar{1}0]_{ZnO}$ direction so that the electron beam was set along the zone axis of $[1\bar{2}10]_{ZnO}$. The films grown on all three $M_2O_3$/Si substrates show similar features in TEM studies. It is apparent from the cross-sectional bright field image of Figure 4.6(a) that both the ZnO film and the $M_2O_3$ buffer layer have uniform thicknesses and smooth interfaces. Threading dislocations originate from the ZnO/$M_2O_3$ interface and propagate to the ZnO film surface. The nu-ZnO layer is too thin to be distinguishable in the bright field image.

Figure 4.6(b) is a cross-sectional dark field image of the same area showing a strong contrast of the threading dislocations (vertical lines), when the diffraction vector **g**

of $10\bar{1}2$ was selected. Several areas of white contrast appear in the figure at or near the nu-ZnO layer. These areas indicate a high density of misfit dislocations, which are either in the plane of the interface or have threaded a small distance into the film, having formed threading dislocation loops. The nu-ZnO layer, however, confines most of these defects to the near-interface region, improving the crystallinity of the ZnO film in general.

Under high magnification **g**-3**g** weak-beam condition (not shown), extinction of most threading dislocation contrast in the ZnO film was observed when the diffraction vector **g** was selected 0002 (out of plane), whereas only a few dislocation become extinct when **g** was selected $20\bar{2}0$ (in plane). Using the **g·b** extinction criterion, we determined that the majority of the threading dislocations were either edge or mixed type with a Burgers vector component lying in the basal plane. The dislocation density calculated from the TEM images is of the same order of magnitude as $N_a$ obtained from high resolution XRD (Table 4.2). For example, the dislocation density obtained from TEM of ZnO/30 nm $Lu_2O_3$/Si is ~$6\times10^9$ $cm^{-2}$.

Figure 4.6(c) is a selected area electron diffraction (SAED) pattern of the interface region containing reflections from ZnO, $M_2O_3$, and Si, under the zone axis of $[1\bar{2}10]_{ZnO}$ (also $[1\bar{1}0]_{Si}$). It is simulated in Figure 4.6(d) where the overlapping of the reflection spots from all three layers is distinguished. No extra reflection spots, such as those related to impurities or twin structures, were seen in the diffraction pattern. The orientation relationship between ZnO, $M_2O_3$, and Si can be directly obtained from the diffraction pattern: $(0001)[10\bar{1}0]_{ZnO}||(111)[\bar{1}\bar{1}2]_{M_2O_3}||(111)[11\bar{2}]_{Si}$.

HRTEM image of the ZnO/$M_2O_3$ interface (e.g. $M$=Gd) is shown in Figure 4.6(e). It reveals an atomic sharp interface between ZnO and $Gd_2O_3$ with no sign of reaction between the two layers. The interface roughness is within one atomic layer. A high density of periodic misfit dislocations with average spacing of about 2 nm is marked, which is originated from the domain matching condition of 6 or 7 atomic spacings of ZnO match 5 or 6 atomic spacings of $Gd_2O_3$.

Besides the threading dislocations, Figure 4.6(b) also shows that both the interface vicinity and inside the ZnO film contain several areas of small, weak lateral contrasts. This is due to a high density of lateral defects that are unable to be resolved

under the diffraction contrast imaging. Using the following HRTEM imaging techniques, we were able to determine the majority of the lateral defects are intrinsic type $I_1$ stacking faults[174] and prismatic dislocation loops.[175]

Figure 4.7(a) is a HRTEM image showing the most commonly observed short segment of type $I_1$ stacking faults in our ZnO films, which are usually formed by insertion of additional ZnO (0001) planes. There are two Frank partial dislocations terminating the stacking fault, and they are typically not located on the same plane. (They will form prismatic dislocation loop if locate on the same plane). This can be clearly visualized by the fast Fourier transform (FFT) pattern and inverse FFT (iFFT) image constructed from the stacking fault vicinity (Figures 4.7(b) and (c)). A Burgers circuit is drawn around one of the Frank partial dislocation in Figure 4.7(d), indicating a Burgers vector of $\mathbf{b}=\frac{1}{6}<20\bar{2}3>$. Figure 4.7(e) simulates the insertion of an extra plane into ZnO lattice using the ball-and-stick model, indicating possible association with zinc vacancies at the dislocation core.

The type $I_1$ stacking faults have also been observed in the vicinity of antiphase boundary (APB) as shown in Figure 4.8(a). The black dotted line indicates the APB, and the white dotting lines indicate the stacking faults where the change in stacking sequence AaBbAaBb|CcBbCcBb is clearly seen. (Here the capital and small letters denote the Zn and O double layers in one plane.) This change in stacking sequence can be recognized as a shear of half of the crystal by $\frac{1}{3}<10\bar{1}0>$ after removal of a (0001) plane.[176] The ball-and-stick model simulation in Figure 4.8(b) clearly visualizes the stacking sequence.

The type $I_1$ stacking faults are the dominant lateral defect in our ZnO films probably due to them having the lowest formation energy among all the types of stacking faults in wurtzite crystals.[174] They have also been observed in ZnO films grown on $Al_2O_3$ and GaN buffer layers,[177,178] and other wurtzite crystals.[176] The association with the insertion of additional planes suggests that the type $I_1$ stacking faults originate from precipitation of Zn interstitials ($Zn_i$). The formation of an additional ZnO double-layer plane requires diffusion of oxygen atoms from surrounding lattice, which could result in condensation of oxygen vacancies ($V_O$) in the lattice.[178] Since both $Zn_i$ and $V_O$ are abundant double donors in ZnO,[179] we believe that stacking faults closely correlates to the unintentional *n*-type electrical transport properties of ZnO films (Section 4.5).

The microstructure of the $M_2O_3$/Si interface after the ZnO growth was investigated by JEOL 2100F STEM with a hexapole $C_S$ corrector. Z-contrast image were obtained in STEM mode using a HAADF detector. The brightness contrast in Z-contrast STEM image is roughly proportional to the square of the atomic number. Figure 4.9(a) is a HAADF-STEM image of the $M_2O_3$/Si interface after the ZnO growth. The dark band in the image is a 3-4 nm thick amorphous layer at the interface. However, no amorphous layer was seen in either HRTEM (Figure 4.3) or STEM (Figure 4.9(b)) images of the $M_2O_3$/Si interface before the ZnO growth.

As mentioned earlier in Section 2.1.1, there has been an ambiguity about the nature of the amorphous layer generated during the direct growth of ZnO on Si. In our work, the amorphous layer is generated at the $M_2O_3$/Si interface but not at the ZnO/$M_2O_3$ interface (Figure 4.6(e)), which is a direct proof that it is $SiO_x$ phase rather than ZnO phase. The dark contrast in STEM image of Figure 4.9(a) also implies that the amorphous layer only contains light elements. The $SiO_x$ layer was generated during the ZnO growth due to oxygen diffusion under a growth pressure of $6.7\times10^{-3}$ mbar. With an estimation of the oxygen diffusion coefficient in $M_2O_3$ to be around $10^{-10}$-$10^{-9}$ $cm^2/s$,[180,181] oxygen ion can diffuse from the $M_2O_3$ surface to the Si surface in 1-8 hours.

Although using $M_2O_3$ buffer layers did not completely prevent the Si surface oxidation during the ZnO growth, it actually prevented the oxide layer from detrimentally affecting the ZnO epitaxy, since the pre-grown highly crystalline $M_2O_3$ layers provide stable templates for ZnO growth, and thus the $SiO_x$ generated below the $M_2O_3$ layer later does not impede the epitaxial growth of subsequently-grown ZnO films. Moreover, using $M_2O_3$ buffer layers for ZnO growth on (111) Si have many advantages such as: (1) avoiding using vacuum growth conditions of ZnO that may induce inferior optical quality of the film (such as in Figure 2.5(c)); and (2) avoiding using extra nitride or sulfide passivation layers and low growth temperature that may result in degradation of the ZnO quality.[112,113,117,118]

In conclusion, our TEM studies reveal much detailed information on the microstructures and defects of the epitaxial ZnO films grown on $M_2O_3$/Si. The orientation relationship between ZnO, $M_2O_3$, and Si is $(0001)[10\bar{1}0]_{\text{ZnO}}\|(111)[\bar{1}\bar{1}2]_{M_2O_3}\|(111)[11\bar{2}]_{\text{Si}}$. Most of the threading dislocations are either edge or mixed type with a Burgers vector

component in the basal plane. Most of the lateral defects are intrinsic type $I_1$ stacking faults and prismatic dislocation loops, which are suggested to be correlated with the electrical properties of the films. There is an amorphous $SiO_x$ layer generated during ZnO growth at the $M_2O_3$/Si interface, however, it does not impede the epitaxial growth of ZnO.

### 4.4 Surface morphologies of the epitaxial ZnO films on $M_2O_3$/Si

Atomic force microscopy (AFM) and optical microscopy were used to measure the surface morphologies of the ZnO films. There is no significant difference for the morphologies of all three $M_2O_3$ buffer layers before the ZnO growth, and also no difference for the morphologies of the ZnO films grown under the same conditions.

Figure 4.10 shows example AFM images of the $Lu_2O_3$ buffer layer and those of the ZnO films grown on it with and without the nu-ZnO layers. The $Lu_2O_3$ buffer layer has a smooth surface shown in Figure 4.10(a), with a root-mean-square (rms) roughness of 0.37 nm. The $Sc_2O_3$ and $Gd_2O_3$ buffer layers have comparable rms roughness of 0.51 nm and 0.45 nm, respectively. A 600 nm thick ZnO film grown on $Lu_2O_3$/Si without the nu-ZnO layer shows hexagonal hills and valleys on the surface (Figure 4.10(b)), with a large rms roughness of 12.55 nm. Similarly, the rms roughness of the films grown without the nu-ZnO layers on $Sc_2O_3$/Si and $Gd_2O_3$/Si are 8.27 nm and 9.63 nm, respectively.

If the nu-ZnO layer was employed initially, the resulting film roughness dramatically drops and the surface morphology changes to a flat plane, as that shown in Figure 4.10(c), but embedded with small scattered surface pits which have hexagonal cross-sections. The depth of the surface pit ranges between 10 nm and 50 nm, and the diameter of the top opening varies from 100 nm to 500 nm. A finer scan of the marked region without the pits is shown in Figure 4.10(d). An atomically smooth surface with steps of the atomic terraces is clearly seen. The rms roughness is in the sub-nanometer range, 0.18 nm, which is close to the height of one atomic layer ($\frac{1}{2}c_{ZnO}$=0.26 nm). Rms roughness of 0.15 nm and 0.16 nm are measured for films grown on $Sc_2O_3$/Si and $Gd_2O_3$/Si, respectively. Combined with the TEM results in Figures 4.6(a) and (b), it can be concluded that the surface pits are induced by threading of edge dislocations during growth, and the surface termination of the edge dislocations is formed at some small-

angle boundaries of slightly misoriented crystal domains.[182] The observation of scattered surface pits is also in agreement with the reduction of dislocation densities by employing nu-ZnO layers, as shown in Table 4.2.

As pointed out in Section 2.2.2.2, cracking often occurs in highly crystalline epitaxial films with larger thickness due to the accumulation of large thermal strain. Figure 4.11 shows an optical microscopic image of a thick ZnO film grown on $Lu_2O_3$/Si. Well ordered crack lines are seen along $<1\bar{2}10>_{ZnO}$ on the surface, forming the shape of equilateral triangles. The crack density is estimated to be ~40 $cm^{-1}$, comparable to the reports of ZnO grown on (111) Si with other buffer layers.[112,115] There exists a cracking critical thickness ($h$) of the film, beyond which the accumulated tensile in-plane strain is too large for the film to remain cohesive. The critical thicknesses are about 800 nm for the ZnO films grown on $Sc_2O_3$/Si and $Lu_2O_3$/Si, and about 1.4 µm for the films grown on $Gd_2O_3$/Si. Using a tensile strength ($\sigma$) value of 412 MPa reported for polycrystalline ZnO film measured by the microbridge methods,[122] we estimate the fracture toughness ($K_{1C}$) of our ZnO film to be[183] $K_{1C} = 1.37\sigma\sqrt{h}$ =0.67 MPa $m^{1/2}$. Although this value is overestimated due to the tensile strength difference between polycrystalline and epitaxial films, it is reasonably located between the $K_{1C}$ values reported for $\{10\bar{1}0\}$ plane of ZnO crystal (0.09 MPa $m^{1/2}$)[184] and that reported for sintered ZnO disk (0.75-1.0 MPa $m^{1/2}$).[185]

The larger cracking critical thickness of ZnO on $Gd_2O_3$/Si is probably due to a larger thermal expansion coefficient of $Gd_2O_3$ than that of ZnO, which introduces compensative strain in the ZnO films. The cracking critical thickness can be effectively improved by reducing the cooling rate after growth, increasing ($Gd_2O_3$) or decreasing ($Sc_2O_3$ and $Lu_2O_3$) the buffer layer thickness, and by employing proper multi-step growth to effectively strain-engineer the ZnO films.[110] However, the improvement of cracking critical thickness always has some tradeoffs, such as degrading the film crystallinity and complicating the fabrication process.

In short, our ZnO films grown on $M_2O_3$/Si have atomically smooth surface embedded with a few threading dislocation pits. A low density of cracks is observed on the surface when the film is grown above cracking critical thickness.

### 4.5 Electrical properties of the epitaxial ZnO films on $M_2O_3$/Si

The electrical transport properties of crack-free ZnO films grown on $M_2O_3$/Si were measured by temperature-dependent Hall measurements using the van der Pauw four-point configuration. Unintentional *n*-type electrical transport was measured for these undoped ZnO films. Table 4.3 compare the electrical data of these films measured at room temperature (300 K) with those of the ZnO films grown under the same conditions on *c*-$Al_2O_3$ and ZnO substrate. No significant differences were observed for the films grown with or without the nu-ZnO layers. Ohmic contacts to the ZnO films were made by pressing indium shot and annealing at 300 °C in flowing $N_2$. The measurements made on the ZnO/$M_2O_3$/Si films were supposed to reflect electrical transport only in the ZnO layers, since the *p*-Si substrates were resistive (>50 Ω cm) and the $M_2O_3$ layers were insulating (Section 4.1).

Due to smaller dislocation densities of the ZnO films on $M_2O_3$/Si than those on *c*-$Al_2O_3$ (Table 4.2), better electrical properties are also measured. Comparing with the film grown on *c*-$Al_2O_3$ substrate in Table 4.3, the ZnO films grown on $M_2O_3$/Si are 7-10 times more conductive, have 6-9 times higher electron concentrations, and most significantly, the electron Hall mobilities are enhanced by 100%-170%. Although the ZnO films grown in our PLD system on *c*-$Al_2O_3$ substrates do not show the same high Hall mobility as those (130-155 $cm^2$/V s) reported for multistep PLD[186] or multi-buffer-layer MBE[187] growth, the films grown on $M_2O_3$/Si show mobilities that are among the highest of all reports of ZnO growth on Si. Generally, the ZnO films on $M_2O_3$/Si have resistivities of 0.2-0.3 Ω cm, electron concentrations of $2.5\text{-}3.5\times10^{17}$ $cm^{-3}$, and Hall mobilities of 76-80 $cm^2$/V s, all in narrow ranges despite the variation of the $M_2O_3$ layers thicknesses. The highest Hall mobility was measured 107 $cm^2$/V s from a 1 μm thick ZnO film grown on 60 nm thick $Gd_2O_3$ buffer layer,[110] which is also the highest mobility value ever reported for ZnO growth on Si substrates. In Table 4.3, we also compare the films electrical data with that of a ZnO film homoepitaxially grown in the same PLD system on a semi-insulating (0001) ZnO substrate (~$10^3$ Ω cm).

The narrow range of the RT electrical data of ZnO/$M_2O_3$/Si films is in agreement with our previous assumption that the dominant defects correlating to the RT carrier transport are stacking faults rather than dislocations. One reason to support the

assumption is that, in contrary to the electrical data, the measured dislocation densities (Table 4.2) have a wide fluctuation range of about two orders of magnitude. On the other hand, one would assume that under fixed deposition conditions, such as fixed laser fluence and repetition rate, target conditions, substrate temperature, and oxygen pressure, the stacking faults generated in the film have a constant density. Finally, Look *et al.*[188] and Meyer *et al*.[189] have all predicted that one of the major shallow donors of ZnO is singly-ionized $Zn_i$, which is likely to be structurally stabilized by stacking faults, according to our TEM studies (Section 4.3). Another donor induced by stacking faults, $V_O$, is a deep donor[190], but can also contribute to the *n*-type electrical transport properties by acting as a hole killer to compensate other native acceptors. Therefore, based on the above reasons, we suggest that stacking faults probably correlates to the unintentional *n*-type electrical transport of the ZnO films. The higher electron concentrations of ZnO films grown on $M_2O_3$/Si than those on *c*-$Al_2O_3$ are possibly related to a higher density of stacking faults.

In order to justify the effect of donors $Zn_i$ and $V_O$ on the electrical transport, we have grown a ZnO film on 30 nm $Sc_2O_3$/Si under similar growth conditions but with a smaller film thickness of 300 nm and with a RF oxygen plasma (175W, $3\times10^{-5}$ mbar) source employed during the ZnO growth. Comparing with the ZnO film on 30 nm $Sc_2O_3$/Si in Table 4.3, the film grown with oxygen plasma has an increase of the resistivity, from 0.27 Ω cm to 0.62 Ω cm, a decrease of the electron concentration, from $3.0\times10^{17}$ cm$^{-3}$ to $1.0\times10^{17}$ cm$^{-3}$, and an increase of the mobility, from 76 cm$^2$/V s to 98 cm$^2$/V s. The decrease in electron concentration is due to a suppression of $Zn_i$ and $V_O$ in the films by employing oxygen plasma. The mobility increases because the density of stacking faults is reduced at the same time, so that the defects' effect on electron scattering is also suppressed. The same trend in electrical transport properties has also been reported for CVD grown ZnO films under Zn-rich and O-rich conditions.[189]

In PLD grown ZnO films, usually more than one donor band exists, due to extrinsic shallow donors induced from impurities in the ZnO target or from contaminations in the growth system. Those extrinsic donors are mostly localized by formation of defects such as the stacking faults. Temperature-dependent Hall measurement is employed to study the multi-band conduction and scattering mechanisms

in our films, and to estimate the donor concentrations and binding energies, based on the analysis in Section 3.4.2. Constants used in our simulations are from Ref. 155, 156, 163, and 191.

The temperature dependence of electron concentrations and Hall mobilities between 10 K and 300 K is shown in Figures 4.12 (a)-(c) and (d)-(e) for the ZnO films grown on (111) Si with 30 nm $Lu_2O_3$, 30 nm $Sc_2O_3$, and 60 nm $Gd_2O_3$ buffer layers, respectively. Proceeding from high $T$ (low $1/k_BT$) toward low $T$ in Figures 4.12 (a)-(c), the measured electron concentrations (red squares) rapidly decrease because of donor freeze out. If this decreasing trend continued, the electron concentration would be less than $10^{15}$ $cm^{-3}$ at very low $T$. However, the electron concentration becomes flat (~4-6×$10^{16}$ $cm^{-3}$) below 30 K in Figures 4.12 (a) and (c), and even tunes up to about 2.4×$10^{17}$ $cm^{-3}$ in Figure 4.12 (b). This unexpected phenomenon implies that the low temperature Hall data are strongly affected by a degenerate conduction band, probably located at the ZnO/$M_2O_3$ interface. This degenerate layer implies down-bending of the ZnO conduction band at the interface as shown in Figure 4.13, possibly induced by (1) the defective nu-ZnO layer at interface (Figure 4.6(b)), and/or (2) the polarity effect of ZnO surfaces.[192] To draw to scale the band diagram in Figure 4.13, the band gap energy ($E_g$ ~ 6.3 eV) and the electron affinity ($\chi$ ~ 3 eV)[193] of $Sc_2O_3$ were used. ($E_g$ ~ 5.3 eV, $\chi$ ~ 0.63 eV for $Gd_2O_3$).[194] Our ZnO film has O-polar face at the ZnO/$M_2O_3$ interface, where positive charged bounded spontaneous polarization charges ($+Q_{SP}$) can induce band bending and accumulation of electrons at the interface.[192]

It has been pointed out by Look *et al*.[154] that the fitted donor concentrations and binding energies can be significantly deviated from the true values if CBE simulation was simply applied to the as-measured data without taking into account the degenerate layer. Therefore, we have applied the two-layer model discussed in Section 3.4.2 to the as-measured Hall data, assuming the degenerate interfacial layer has an electron concentration ($n_0$) and a mobility ($\mu_0$) independent of temperature at low $T$ (<30 K). The corrected electron concentrations and mobilities are extracted from the as-measured data and plotted in Figure 4.12 (black dots) for comparison. It is obvious that after the two-layer correction, the electron concentrations at low $T$ are shifted down and the corresponding mobilities are shifted up. The corrected data are well fitted (black lines) by

three-band CBE simulation and the Matthiessen's rule. The values used for $n_0$, $\mu_0$, and the fitting parameters such as concentrations ($N_D$) and binding energies ($E_D$) of the three donors are listed in Table 4.4.

Table 4.4 shows that the films grown on three different $M_2O_3$/Si substrates have two consistent donor states: one is at 63-65 meV ($E_{D1}$) below the conduction band with donor concentration of 1.5-2.4×$10^{17}$ $cm^{-3}$ ($N_{D1}$), and the other one is at 40-46 meV ($E_{D2}$) with concentration of 1.1-1.9×$10^{17}$ $cm^{-3}$ ($N_{D2}$). $E_{D1}$ is in line with the dominant hydrogenic-nature donor at 60 meV reported for bulk ZnO.[8] $E_{D2}$ is close to the donor binding energy predicted for the intrinsic donor $Zn_i$ (~30 meV).[188,189] However, in Section 4.6 we will combine with PL and SIMS measurements to demonstrate that it is possible that these two donors are extrinsic donors referring to indium and calcium impurities in the films. The third donor with extremely small binding energy ($E_{D3}$≤6 meV) has not been reported. We found it is only necessary to be included in simulation if we want to fit the electron concentration at low $T$ (<50 K). This donor may not reflect true properties since the low $T$ data is often discarded during other simulations.[154,188]

Note that in the simulation of the film on $Gd_2O_3$/Si, we choose $\mu_0$=20 $cm^2$/V s for the interfacial layer, though the measured mobility at very low $T$ is as high as 140 $cm^2$/V s. Here we underestimate $\mu_0$ considering the fact that this interfacial layer should be highly defective with strong scattering effect, and thus it should has a reasonable mobility of around 10-20 $cm^2$/V s, as shown in the films on $Lu_2O_3$/Si and $Sc_2O_3$/Si. We have confirmed that if we use $\mu_0$=140 $cm^2$/V s, then the extracted mobility in Figure 4.12(f) would have a secondary peak of about 300 $cm^2$/V s at low $T$, which would make no sense and could not be fitted. Using $\mu_0$=20 $cm^2$/V s, the corrected Hall data can be fit well, but the electron concentration and the mobility are not shifted much as shown in Figures 4.12 (c) and (f). The corrected electron concentration data are still flat at low $T$, whose fit requires an extremely small $E_{D3}$ which does not have a true physical meaning. From this inconsistency in the simulation, we propose that another carrier source other than the interfacial layer should be taken into account for the film grown on $Gd_2O_3$/Si. And this source should produce electrons with high mobilities of >100 $cm^2$/V s at low $T$. Although details of this LT electron source is unclear at present, some reports suggest that it could

possibly be hydrogen-related surface conduction[195] or two-dimensional electron gas formed at $ZnO/Gd_2O_3$ interface.[196]

The mobility fit of the three films in Figures 4.12 (d)-(f) includes the five components of scattering mechanisms (colorful lines), among which the dislocation scattering mechanism ($\mu_{dis}$) was originally developed in the GaN system[163] and recently adapted for use for the ZnO system. Figure 4.12 shows that the electron mobilities of the ZnO films generally peak at 150 K; the dislocation scattering dominates at low *T*, while the polar optical phonon scattering ($\mu_{po}$) is the dominant mechanism at high *T*. The fits give dislocation densities between $2.6\times10^8$ $cm^{-2}$ and $8.0\times10^8$ $cm^{-2}$ (Table 4.4), which are consistent with the *c*-type dislocation densities obtained from XRD measurements (Table 4.2). It implies that *c*-type dislocations may have a larger impact on the film's electrical properties at low *T*.

Some conclusions on the electrical properties of the ZnO films grown on $M_2O_3$/Si are: the films exhibit small resistivities of 0.2-0.3 Ω cm, steady electron concentrations of 2.5-3.5$\times10^{17}$ $cm^{-3}$, and high Hall mobilities of 76-107 $cm^2$/V s at RT; stacking faults are suggested to contribute to the RT electrical transport by association with $Zn_i$ and $V_O$ donors; temperature-dependent Hall measurements and two-layer corrected simulations give two donor states with energy levels of 63-65 meV and 40-46 meV, respectively; the mobility fittings indicate that dislocation scattering and polar optical phonon scattering dominate respectively at LT and RT.

## 4.6 Optical properties of the epitaxial ZnO films on $M_2O_3$/Si

### 4.6.1 Temperature-dependent PL measurements

The ZnO films on $M_2O_3$/Si exhibit outstanding optical properties. Temperature-dependent PL measurements were made using a He-Cd laser with a wavelength of 325 nm. Figure 4.14(a) compares representative PL spectra of the films measured at 10 K with that of a ZnO single crystal (Zn-face, MTI corp.). The ZnO films shown in Figure 4.14(a) are about 800 nm thick, grown on 60 nm $Gd_2O_3$/Si, 30 nm $Lu_2O_3$/Si, and 100 nm $Sc_2O_3$/Si, respectively. (No significant difference of PL spectra were observed regarding to different $M_2O_3$ layer thicknesses.) The spectra of the films show excitonic recombination features comparable to those of the bulk crystal in the NBE region of 3.0-

3.4 eV. Such features include the signal to noise ratio ($10^6/10^2$) and the energy positions of sharp fine lines. The deep level emission[51,79] between 2.0 and 2.8 eV, which is obvious in the spectrum of the bulk crystal, however, is suppressed nearly to the noise level in the spectra of the films. This phenomenon suggests a much lower density of intrinsic defects ($O_{Zn}$, $Zn_i$, or $V_O$ etc.) in the ZnO films than in the ZnO single crystal. The fine features in the spectra of the ZnO films have the highest resolution among all the reported PL properties of ZnO films grown on Si.

The exciton fine lines in NBE region yield a significant amount of information about the films. First, the FWHM of the dominant sharp peak is strongly dependent on the microcrystallinity of the films. After decomposing the overlapped fine lines in linear scale spectra, we determined the FWHM values of the strongest peaks of the ZnO films grown on $Gd_2O_3$/Si (6.4 meV), $Lu_2O_3$/Si (4.7 meV), and $Sc_2O_3$/Si (2.5 meV), and that of the bulk crystal (2.1 meV). The close-to-bulk FWHM value of ZnO/100 nm $Sc_2O_3$/Si indicates a superior microcrystalline quality of the film, and is in agreement with the lowest dislocation density (Table 4.2) and smallest rocking curve FWHMs (Figure 4.5(b)) measured by XRD.

The fine structure of the exciton lines in NBE region are studied by temperature-dependent PL. For example, Figure 4.14(b) shows the temperature dependence of the NBE emissions of the ZnO film on $Sc_2O_3$/Si. Upon temperature increasing, it is apparent that some peaks become more and more prominent, whereas the others gradually disappear. The former have free exciton feature and the latter have donor-bound exciton feature. Most of the peaks located at lower photon energies are the longitudinal optical phonon replicas (LO phonons) of the high energy ones, and each peak is separated from the previous one by 71-73 meV. In particular, for the high energy fine lines located between 3.34 eV and 3.44 eV, we tabulated their excitonic peak energies in Table 4.5 for the three ZnO films on $M_2O_3$/Si and the ZnO single crystal, and compared with the reported values for ZnO bulk crystals in references.

In Table 4.5, 15 fine lines between 3.34 eV and 3.44 eV are recognized in the spectrum of the ZnO bulk crystal measured in this work, and only 7 lines are distinguishable in the spectra of the films. Comparing the exciton energies of the ZnO bulk crystal with those reported by Renolds *et al.*,[197] Teke *et al.*,[166] and Meyer *et al.*,[167]

there is a steady blueshift of 2.7-3.6 meV for the energies obtained in this work. This blueshift maybe result from sample quality difference, since the quality of current commercial ZnO single crystals varies between venders due to different growth methods. One report[198] showed similar exciton energies to ours with only 1 meV difference, in which the ZnO single crystal was grown by seeded vapor transport method. The 1 meV shift can be easily generated if the constants used in the conversion from wavelength to photon energy ($E=hc/e\lambda$) are different. (We used $h$=6.6260693×$10^{-34}$ J/s, $c$=299792458 m/s, and $e$=1.60217646×$10^{-19}$ C.) Despite the small blueshift, the energy intervals between the exciton lines in this work closely match the reports of others. Therefore, all the fine lines in the spectrum of our measured ZnO bulk crystal can be labeled, as shown in Table 4.5, including longitudinal and transversal free A and B excitons ($A_L$, $A_T$, $B_L$, and $B_T$, where $n$=1 is the ground state and $n$=2 is the excited state), and ionized ($I_0^*$-$I_3$) and neutral donor bound A ($I_4$-$I_{10}$) and B ($I_6^B$) excitons. The 7 lines shown in the spectra of the films are $A_L^{n=2}$, $B_L^{n=1}$, $A_L^{n=1}$, $I_0$, $I_6$, $I_6^B$, and $I_{10}$. The physical nature of the 6 excitons ($I_4$-$I_{10}$) bound to neutral donors is still under investigation at present, however, it is commonly acknowledged that $I_6$ and $I_9$, which are usually the two dominant exciton lines in the PL spectra of ZnO films, are excitons bound to neutral donors of Al and In impurities, respectively.[167]

The 10 K NBE spectra of the ZnO bulk crystal, the ZnO film on $c$-$Al_2O_3$, and the ZnO films on $M_2O_3$/Si are further compared in Figure 4.15. It is clear that the films on $M_2O_3$/Si have comparable spectrum resolution to the ZnO crystal, and much better than that of the film on $c$-$Al_2O_3$. Besides the 15 exciton lines, the spectrum of the ZnO bulk crystal shows a sharp peak located at 3.3256 eV which is the two-electron-satellite[167] (TES) of the $I_6$ line. Based on the donor energy difference between 1s and 2p states in the hydrogenic effective-mass-approach,[167] we obtained a TES separation of 38 meV and a donor binding energy of 50.7 meV for $I_6$, which again, closely match the TES separation (38.8 meV) and the donor binding energy (51.55 meV) reported for excitons bound to neutral Al donors.[167] The two dominant peaks in the ZnO films are $I_6$ and $I_6^B$. The $I_{10}$ line is also intense for all the ZnO films. However, we have performed SIMS depth profile measurements (Figure 4.16), confirming that Ca and In are the two major impurities in

the ZnO films with concentrations of 4-5×$10^{17}$ atoms/$cm^{-3}$ each. Since no significant amount of Al was detected by SIMS, we attribute Ca impurities to be the donor related to $I_6$ rather than the commonly assigned Al. The $I_{10}$ line is then very likely to be In-related. Considering the fact that $I_6$ is also dominant in the ZnO crystal spectrum and Ca is also detected by SIMS for the ZnO target (Figure 3.8), thus Ca is probably a residual impurity from the manufacturing process of the ZnO bulk crystal and the target. Possible sources of the In impurities are the ZnO target or the cross-contamination from the PLD chamber.

Comparing the SIMS data in Figure 4.16 and Figure 3.8, it is worthy to note that: the Mg and Ga impurities in the ZnO film are probably induced by cross-contamination from the chamber because the concentrations are higher in the film than in the target; and the ZnO films grown on $M_2O_3$/Si generally have small artificial contaminations such as Na, K, and Fe.

It is important to note that the donor binding energy obtained by PL measurements, also known at the optical ionization energy ($E_{D0}$), is not the same as the donor binding energy obtained by electrical measurements, known at the thermal activation energy ($E_D$). However, the concentration dependence[199] of $E_D$ suggests that the two energies are related by $E_{D0}=E_D+\alpha N_D^{1/3}$, where $\alpha_{ZnO}$=1.2×$10^{-5}$ meV cm.[200] Using the fitted $E_D$ and $N_D$ of the first two donors from the electrical measurements (Table 4.4), we calculated the optical ionization energies of Donor 1 and Donor 2 to be 47-52 meV and 69-73 meV, respectively. These values well match the value of 50.7 meV we obtained from PL spectra for $I_6$, and the value of 72.6 meV reported[167] for $I_{10}$. Therefore, our electrical and optical measurements reach an agreement on the binding energies of the two major donors in the ZnO films. It is also worth noting that the extrinsic donor suggested by electrical and optical measurements is consistent with the TEM results that stacking faults contribute to the electrical transport. The reason is that the incorporation of impurities, such as In and Ca, into the ZnO films can consequently induce $Zn_i$ defects which promote the formation of type $I_1$ stacking faults.

The vertical dotted lines in Figure 4.15 indicate that the spectra of the ZnO/$M_2O_3$/Si films slightly redshift from that of the ZnO crystal. Comparing the energies of the 7 exciton lines listed in Table 4.5, the redshifts are roughly 2-4 meV, 3-5 meV, and 4.5-6.5 meV for the ZnO films grown on $Gd_2O_3$/Si, $Lu_2O_3$/Si, and $Sc_2O_3$/Si, respectively.

The redshifts of PL spectra are correlated with residual in-plane tensile strain in the films. The strain will be quantified by high resolution XRD measurements in Section 4.6.2. Generally, the redshifts of free exciton lines are about 1-2 meV larger than those of $I_6$ and $I_6^B$ due to a band gap reduction induced by free electron many-body effect.[200] And the redshifts varies from sample to sample, because the strain status is different for the ZnO films grown on different buffer layers, or grown with different film or buffer layer thicknesses.

In Figure 4.15, there is one intense line located at 3.3329 eV, which is only shown in the spectra of the ZnO films but not clearly distinguishable in the spectrum of the ZnO crystal. This line shows donor bound exciton nature in temperature-dependent PL measurements but almost has no energy shift between the films grown on different $M_2O_3$ buffer layers. It has been assigned to excitons bound to native structural defects (Y-line),[167] such as dislocations in the films. Since the ZnO bulk crystal must have lower defects density than the ZnO films, Y-line is not intense in the PL spectrum of the ZnO crystal. In addition, structural defects are all localized at crystal irregularities throughout the film, thus the energy positions of Y-lines should not be strain sensitive.

### 4.6.2 Strain-related PL spectrum shift

It has been pointed out in Section 2.2.2.2 that the residual elastic strain in heteroepitaxial films is induced by lattice and thermal mismatches between the film and the substrate. It is important to understand and control such strain, because an in-plane tensile strain could induce severe film cracking and thus degrade the device performances. In one respect, the in-plane tensile strain leads to renormalization of the energy band gap, which is represented by a redshift in PL or Raman spectrum. Although a free carrier screening and band gap renormalization effect[200] and Burstein-Moss effect[201] can also induce spectrum shifts, they are unlikely to be the main effects in our films, because all of the $ZnO/M_2O_3/Si$ films are grown under the same conditions, have constant electron concentrations of $2.5\text{-}3.5\times10^{17}$ $cm^{-3}$, and are characterized by the same laser intensity in PL measurements. If the correlation between the spectrum redshift and the in-plane strain can be quantified, it can provide an effective method to use PL for monitoring and

manipulating the strain in ZnO films. Similar correlation[147,202] has already been established for epitaxial GaN films.

In this work, we quantify the correlation between the PL spectrum shift and the residual strain in ZnO/$M_2O_3$/Si films by directly measuring both our-of-plane and in-plane strains of the films using high resolution triple-axis XRD. In symmetric geometry, the Bragg angle of ZnO 0002 reflection can be accurately determined in a $\theta$-$2\theta$ scan by taking the Si 111 reflection as a standard reference. In skew symmetric geometry, the Bragg angle of ZnO $10\bar{1}3$ reflection can be measured referred to Si 113 reflection. Figure 4.17(a) shows an example of the scans in both geometries, taking Si reflections as the $\delta\theta$=0 reference peaks. After deriving the *d*-spacings of both ZnO 0002 and $10\bar{1}3$ reflections from the corresponding Bragg angles, we calculated the lattice constants *c* and *a* of the films, and obtained the residual strains of the films along the *c*- and *a*- axes ($\varepsilon_{zz}$ and $\varepsilon_{xx}$) using equation 3.12 and 3.13.

Positive $\varepsilon_{xx}$ and negative $\varepsilon_{zz}$ were measured in all ZnO/$M_2O_3$/Si films, suggesting all films are biaxially tensile strained in the basal plane and compressively strained along the *c*-axis. Energies of the strongest free exciton line ($A_L^{n=1}$) and the most intense donor bound exciton line ($I_6$) are plotted versus the in-plane biaxial strain $\varepsilon_{xx}$ in Figure 4.17(b) for a group of ZnO/$M_2O_3$/Si samples with different film and buffer layer thicknesses. As seen from Table 2.2 and the discussion in Section 2.2.2.2, the residual strain in ZnO films grown on Si is induced during post-growth cooling by a smaller thermal expansion coefficient of the substrate Si than that of ZnO. Figure 4.17(b) shows that, the films grown on $Gd_2O_3$ buffer layers (blue triangles) have roughly smaller in-plane tensile strain than those grown on $Lu_2O_3$ and $Sc_2O_3$ buffer layers, owing to a larger thermal expansion coefficient of $Gd_2O_3$ than that of ZnO (Table 2.2). Therefore, using buffer layers with larger thermal expansion coefficients than that of ZnO is a feasible way of introducing compressive strain to partially compensate the residual tensile strain in the ZnO films grown on Si. It is also consistent with the smaller redshift indicated in Figure 4.15 for the ZnO films grown on $Gd_2O_3$/Si.

Figure 4.17(b) shows that both $A_L$ and $I_6$ shift to lower energy as $\varepsilon_{xx}$ increases. The straight lines are linear regression to the data. For reference, we include a homoepitaxial ZnO film grown on (0001) ZnO substrate, which is slightly compressively

strained due likely to native defects or impurities in the homoepitaxial film. Assuming the films were biaxially strained only, from Hooke's law the in-plane biaxial stress is $\sigma_{xx} = \sigma_{yy} = (C_{11} + C_{12} - 2C_{13}^2 / C_{33})\varepsilon_{xx}$, where the elastic constants are $C_{11}$=207 GPa, $C_{12}$ =117.7 GPa, $C_{13}$ =106.1 GPa, and $C_{33}$ =209.5 GPa.[146] Therefore, from the slopes in Figure 4.17(b) we calculate the energy redshift induced by the biaxial stress to be $\delta E / \delta\sigma_{xx}$ = -4.0±0.7 meV/GPa for free exciton $A_L^{n=1}$ and -3.3±0.7 meV/GPa for donor bound exciton $I_6$. These values are consistent with theoretical computations[203] and are only one sixth of those reported for GaN films (-27 meV/GPa),[147] suggesting the optical properties of ZnO are less strain-sensitive than those of GaN.

It should be pointed out that the average value of the Poisson number obtained from Equation 3.14 for our films ($\gamma$~0.23) is slightly deviated from those reported[145,146] for biaxially strained bulk ZnO and films (~0.3). This could be induced by nonstoichiometric composition of our ZnO films. Taking the Poisson number deviation into account, the slope of $\delta E / \delta(\varepsilon_{xx} \times 10^2)$ can be converted into $\delta E / \delta\varepsilon_{zz}$ ~1.4 eV, which is comparable to the values in other ZnO reports obtained by Raman and reflectance measurements (~1.5 eV).[145]

### 4.6.3 Electroluminescence from ZnO/$M_2O_3$/*p*-Si (111) heterostructures

The ZnO/$M_2O_3$/(111) Si heterojunctions were further fabricated into prototype light emitting diodes and tested EL properties. Pressed and annealed In shot was adopted as Ohmic contacts on the ZnO surfaces and on the bottom of the *p*-Si (111) substrates. Figure 4.18(a) shows the I-V characteristics and the schematic diagram of a ZnO (300 nm)/$Gd_2O_3$ (20 nm)/*p*-Si diode operated at forward bias. A good rectification is observed with a threshold voltage of about 6 V. In the forward bias region above the threshold voltage, the increase of current is limited by a linear resistance of about 240 Ω, which is consistent with the resistance of the Si substrate ($\rho$>50 Ω cm).

The EL spectra measured at room temperature are shown in Figure 4.18(b) with respect to different forward currents from 10 mA to 35 mA. There are four distinguishable peaks located at 3.18 eV (390 nm), 2.64 eV (470 nm), 2.25 eV (550 nm), and 1.91 eV (645 nm) in the 35 mA spectrum. The diodes of ZnO on $Sc_2O_3$/Si and

$Lu_2O_3$/Si show similar EL spectra. The 3.18 eV peak (marked by arrow) indicates the NBE emission from the ZnO film, however, with a weak intensity due to self-absorption of ZnO.[204] The other three peaks have similar energy positions as those reported to be Bragg's multiple reflections in a ZnO-based homojunction LED,[204] however, we have different explanations here. It is necessary to note that the black dashed spectrum in Figure 4.18(b) is the luminescence measured from an ITO/$Gd_2O_3$/*p*-Si structure under a forward current of 100 mA. The $Gd_2O_3$/Si layer is the same as in the ZnO-based diode. The ITO layer (~100 nm thick) is a transparent conductive layer which acts as a secondary ohmic contact. The top and bottom contacts are still In. Comparing the dashed spectrum with the 35 mA spectrum of the ZnO-based diode, they both have the peaks of 2.25 eV and 1.91 eV. We suggest that these two peaks originate from defect level emissions in $Gd_2O_3$ layer, possibly from structural defects localized at the $Gd_2O_3$/Si interface or at uneven, ragged cleave edges of the samples. The other peak at 2.64 eV, which does not show up in the $Gd_2O_3$ spectrum, could be another defect-related emission from structural defects inside the ZnO film such as threading dislocations.

Although the physics of the defect level emissions is unclear at present, and the EL intensities of the ZnO NBE emissions are low in our prototype diode, we have demonstrated that the ZnO films grown on $M_2O_3$/(111)Si have the potential to be used in light-emitting devices. The series resistance of the prototype diode can be reduced by employing conductive Si substrate, reducing the $M_2O_3$ thickness, and applying *n*-type doping to the ZnO film. Eventually, the EL intensity of the ZnO NBE emission can be enhanced if the ZnO self-absorption issue can be solved, and if the defect level emission can be suppressed. In future work, we will attempt to enhance the EL intensity and fabricate high quality ZnO-based homojunction devices on (111) Si for LED applications.

To wrap up the optical properties of the ZnO/$M_2O_3$/(111)Si films: The films exhibit outstanding PL characteristics comparable to that of ZnO single crystal. The two major donor-bound exciton lines $I_6$ and $I_{10}$ are assigned to excitons bound to Ca and In neutral donors with optical ionization energies of 50.7 meV and 69-73 meV, respectively. Thermal-mismatch induced residual in-plane tensile strain causes PL spectrum redshifts. Due to thermal expansion differences, the films grown on $Gd_2O_3$/Si, $Lu_2O_3$/Si, and

$Sc_2O_3$/Si show a redshift of 2-4 meV, 3-5 meV, and 4.5-6.5 meV, respectively. The relationship between the redshift and the biaxial stress is quantified by high-resolution XRD that: 1 GPa of biaxial stress results in a shift of 4.0±0.7 meV for the free exciton and 3.3±0.7 meV for donor-bound exciton transition lines. Prototype LED devices of ZnO/$M_2O_3$/*p*-Si exhibit rectifying I-V characteristics and EL of ZnO NBE emission. Although strong defect level emissions exist in the EL spectra, the ZnO films grown on $M_2O_3$/(111)Si have great potential for optoelectronic applications.

### 4.7 Summary and conclusions

The epitaxial ZnO films grown on (111) Si with epitaxial bixbyite oxide ($M_2O_3$, *M*=Sc, Lu, Gd) buffer layers are of high structural quality, represented by:

(1) small FWHM values of ZnO $\omega$-rocking curves of 0.08°-0.11° for 0002 reflections and 0.11°-0.16° for $10\bar{1}2$ reflections;

(2) small tilt and twist angles and low densities of $10^7$-$10^9$ cm$^{-2}$ for *c*-type dislocations (dislocations with screw components), and $10^8$-$10^{10}$ cm$^{-2}$ for *a*-type dislocations (dislocations with edge components);

(3) amorphous-free and atomically sharp interfaces with $M_2O_3$;

(4) atomically smooth ZnO surfaces with rms roughnesses in the sub-nanometer range;

(5) epitaxial out-of-plane and in-plane orientation relationships of $(0001)[10\bar{1}0]_{\mathrm{ZnO}}||(111)[\bar{1}\bar{1}2]_{M_2O_3}||(111)[11\bar{2}]_{\mathrm{Si}}$.

The films exhibit good *n*-type electrical transport properties with resistivities of 0.2-0.3 Ω cm, electron concentrations of 2.5-3.5×$10^{17}$ cm$^{-3}$, and Hall mobilities of 76-107 cm$^2$/V s at RT. Intrinsic type $I_1$ stacking faults and prismatic dislocation loops are identified in the films, and they correlates to the *n*-type conductivity. Temperature-dependent Hall measurements imply the existence of degenerate interfacial layer and two dominant hydrogenic-nature donors.

The films exhibit outstanding PL properties comparable to those of ZnO single crystal. Temperature-dependent PL measurements indicate neutral donors in the films with optical ionization energies of 50.7 meV and 69-73 meV, respectively. The optical

ionization energies match the thermal activation energies obtained for the two donors from temperature-dependent Hall measurements. SIMS measurement identify the two major impurities are Ca and In.

A couple of meV redshift of the PL spectrum is caused by thermal-mismatch induced biaxial tensile strain in the ZnO films on $M_2O_3$/Si. The correlation between the tensile stress and the spectrum shift are quantified: 1 GPa of biaxial stress results in a shift of 4.0±0.7 meV for the free exciton, and 3.3±0.7 meV for donor-bound exciton transition lines.

Usually the ZnO films grown on $Sc_2O_3$ buffer layer have the best structural quality than the films grown on the other two buffer layers. And the films grown on $Gd_2O_3$ buffer layer have the least residual strain than grown on the other two buffer layers.

ZnO NBE emission is demonstrated in EL spectra from prototype ZnO/$M_2O_3$/*p*-Si light-emitting heterostructures.

The above results indicate that the epitaxial ZnO films grown on $M_2O_3$/(111) Si are of high structural, electrical, and optical qualities. This work is an important step toward the development of ZnO-based optoelectronic devices and the realization of ZnO-based multifunctional device integration on Si substrates.

Table 4.1 Enthalpy of formation ($\Delta_f H°$), lattice constants ($a_{latt}$), and internal parameters ($u$, $x$, $y$, and $z$) of the bixbyite oxides.

| Bixbyite oxide | $\Delta_f H°$ (kJ/mol)[205] | $a_{latt}$ (Å)[206-209] | Internal parameters[210-212] | | | |
|---|---|---|---|---|---|---|
| | | | $u$ | $x$ | $y$ | $z$ |
| $Sc_2O_3$ | -1908.8 | 9.845 | -0.0351 | 0.3928 | 0.1528 | 0.3802 |
| $Lu_2O_3$ | -1878.2 | 10.391 | -0.0330 | 0.3912 | 0.1521 | 0.3800 |
| $Y_2O_3$ | -1905.31 | 10.604 | -0.0327 | 0.3908 | 0.1516 | 0.3799 |
| $Gd_2O_3$ | -1819.6 | 10.813 | -0.0324 | 0.3910 | 0.1518 | 0.3755 |

Table 4.2 Comparison of tilt ($\alpha_\Omega$) and twist ($\alpha_\Phi$) angles and dislocation densities ($N_c$ and $N_a$) of ~1 μm thick ZnO films grown under the same growth conditions.

| ZnO films grown on | $\alpha_\Omega$ (°) | $\alpha_\Phi$ (°) | $N_c$ ($cm^{-2}$) | $N_a$ ($cm^{-2}$) |
|---|---|---|---|---|
| nu-ZnO/*c*-$Al_2O_3$ substrate | 0.11 | 0.49 | $3.4\times10^8$ | $1.6\times10^{10}$ |
| nu-ZnO/30 nm $Gd_2O_3$/(111)Si | 0.22 | 0.49 | $1.2\times10^9$ | $1.6\times10^{10}$ |
| nu-ZnO/30 nm $Lu_2O_3$/(111)Si | 0.08 | 0.25 | $1.7\times10^8$ | $4.1\times10^9$ |
| nu-ZnO/30 nm $Sc_2O_3$/(111)Si | 0.08 | 0.13 | $1.6\times10^8$ | $1.1\times10^9$ |
| nu-ZnO/100 nm $Sc_2O_3$/(111)Si | 0.05 | 0.11 | $6.9\times10^7$ | $8.0\times10^8$ |
| 60 nm $Gd_2O_3$/(111)Si | 0.19 | 0.27 | $9.0\times10^8$ | $4.8\times10^9$ |
| nu-ZnO/60 nm $Gd_2O_3$/(111)Si | 0.08 | 0.10 | $1.5\times10^8$ | $5.4\times10^8$ |

Table 4.3 Comparison of RT electrical properties of ZnO films grown at 600 °C on different buffer layers/substrates under the same growth conditions.

| ZnO films grown on | ZnO thickness ±20 (nm) | $\rho$ (Ω cm) | $n$ ($cm^{-3}$) | $\mu$ ($cm^2$/V s) |
|---|---|---|---|---|
| (0001) $Al_2O_3$ substrate | 600 | 2.4 | $4.0\times10^{16}$ | 40 |
| nu-ZnO/30 nm $Gd_2O_3$/(111)Si | 800 | 0.24 | $3.5\times10^{17}$ | 76 |
| nu-ZnO/30 nm $Lu_2O_3$/(111)Si | 600 | 0.31 | $2.5\times10^{17}$ | 80 |
| nu-ZnO/30 nm $Sc_2O_3$/(111)Si | 800 | 0.27 | $3.0\times10^{17}$ | 76 |
| nu-ZnO/100 nm $Sc_2O_3$/(111)Si | 700 | 0.33 | $2.5\times10^{17}$ | 77 |
| nu-ZnO/60 nm $Gd_2O_3$/(111)Si | 1000 | 0.2 | $3.0\times10^{17}$ | 107 |
| (0001) ZnO substrate* | 800 | 0.015 | $2.8\times10^{18}$ | 146 |

* ZnO substrate is from MTI, Inc.

Table 4.4 Fitting parameters used in the CBE simulations and mobility fittings for the corrected electrical data in Figure 4.12.

| Fitting parameters in Figure 4.12 | | (a) on $Lu_2O_3$ | (b) on $Sc_2O_3$ | (c) on $Gd_2O_3$ |
|---|---|---|---|---|
| Interfacial layer | $n_0$ ($cm^{-3}$) | $4.4\times10^{16}$ | $2.4\times10^{17}$ | $5.7\times10^{16}$ |
| | $\mu_0$ ($cm^2$/V s) | 11 | 10 | 20* |
| Donor 1 | $n_{D1}$ ($cm^{-3}$) | $2.4\times10^{17}$ | $2.3\times10^{17}$ | $1.5\times10^{17}$ |
| | $E_{D1}$ (meV) | 65 | 63 | 63 |
| Donor 2 | $n_{D2}$ ($cm^{-3}$) | $1.4\times10^{17}$ | $1.1\times10^{17}$ | $1.9\times10^{17}$ |
| | $E_{D2}$ (meV) | 42 | 46 | 40 |
| Donor 3 | $n_{D3}$ ($cm^{-3}$) | $4.8\times10^{16}$ | $6.2\times10^{16}$ | $1.0\times10^{17}$ |
| | $E_{D3}$ (meV) | 6 | 5 | 2 |
| Background acceptor | $N_A$ ($cm^{-3}$) | $1.0\times10^{16}$ | $4.0\times10^{15}$ | $2.0\times10^{15}$ |
| Dislocation density | $N_{dis}$ ($cm^{-2}$) | $5.0\times10^{8}$ | $8.0\times10^{8}$ | $2.6\times10^{8}$ |

* We assume the value of $\mu_0$ should be no more than 20 $cm^2$/ V s for the defective interfacial layer, though the measure mobility at low *T* in Figure 4.12(f) is high.

Table 4.5 Comparison of PL exciton peak energies of the ZnO films grown on $M_2O_3$/Si with the energies of a ZnO single crystal and those reported in references.

| Excitons \ $E$ (eV) | ZnO crystals (references) | | ZnO crystal (this work) | ZnO/ $Gd_2O_3$/Si | ZnO/ $Lu_2O_3$/Si | ZnO/ $Sc_2O_3$/Si |
|---|---|---|---|---|---|---|
| 1) $A_L^{n=2}$ | 3.4221 [197] | | 3.4249 | 3.4203 | 3.4198 | 3.4180 |
| 2) $B_L^{n=1}$ | 3.3895 [197] | | 3.3934 | 3.3890 | 3.3884 | 3.3870 |
| 3) $B_T^{n=1}$ ($UPB_A$) | 3.3810 [166] | 3.3829 [198] | 3.3838 | | | |
| 4) $A_L^{n=1}$ | 3.3772±0.0001 [197,167] | 3.3793 [198] | 3.3803 | 3.3765 | 3.3750 | 3.3735 |
| 5) $A_T^{n=1}$ | 3.3759 [167] | 3.3775 [198] | 3.3786 | | | |
| 6) $I_0^*$ | 3.3733 [167] | | 3.3767 | | | |
| 7) $I_0$ | 3.3725 [167] | | 3.3756 | 3.3728 | 3.3709 | 3.3697 |
| 8) $I_3$ | 3.3665 [167] | | 3.3695 | | | |
| 9) $I_6^B$ | 3.3652 [167] | | 3.3680 | 3.3658 | 3.3652 | 3.3637 |
| 10) $I_4$ | 3.3628 [167] | | 3.3661 | | | |
| 11) $I_5$ | 3.3614 [167] | | 3.3650 | | | |
| 12) $I_6$ | 3.3608 [167] | | 3.3636 | 3.3609 | 3.3600 | 3.3587 |
| 13) $I_7$ | 3.3600 [167] | | 3.3628 | | | |
| 14) $I_9$ | 3.3567 [167] | | 3.3600 | | | |
| 15) $I_{10}$ | 3.3531 [167] | | 3.3561 | 3.3527 | 3.3518 | 3.3502 |

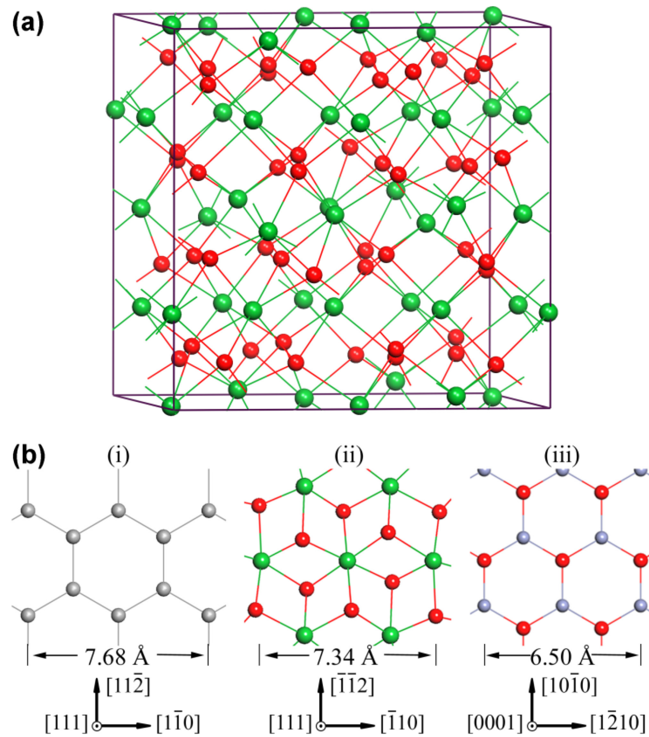


Figure 4.1 (a) Unit cell of the $M_2O_3$ lattice. Green spheres indicate $M$ (Sc, Lu, Y, Gd) atoms, red spheres oxygen. The internal parameters of $Lu_2O_3$ (Table 3) are adopted to construct this unit cell. (b) Atomic arrangements of (111) Si (i), (111) $M_2O_3$ (ii), and (0001) ZnO (iii). (from Guo *et al*. [108])

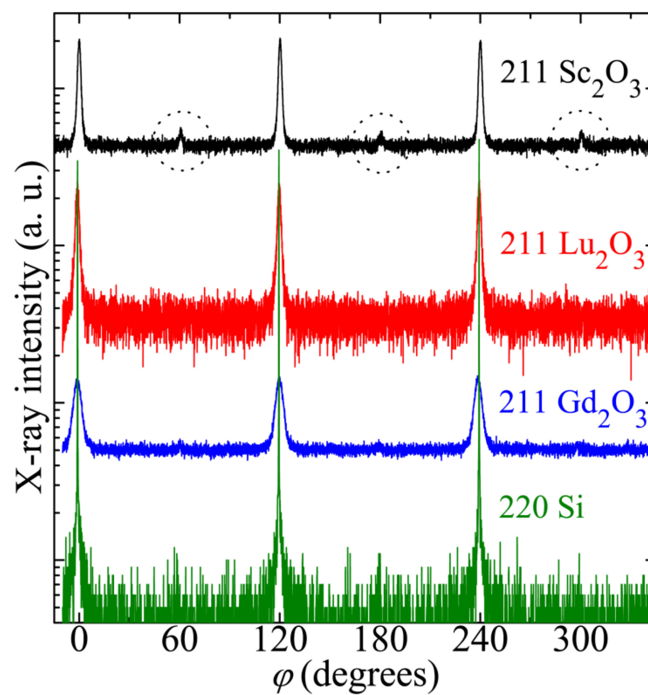


Figure 4.2 XRD $\phi$-scans (on a log scale) of $Sc_2O_3$, $Lu_2O_3$, and $Gd_2O_3$ 211 peaks, and Si 220 peaks. The spectra are vertically displaced for clarity. The circles indicate a small fraction (<5%) of A-type domains in the $Sc_2O_3$ films.

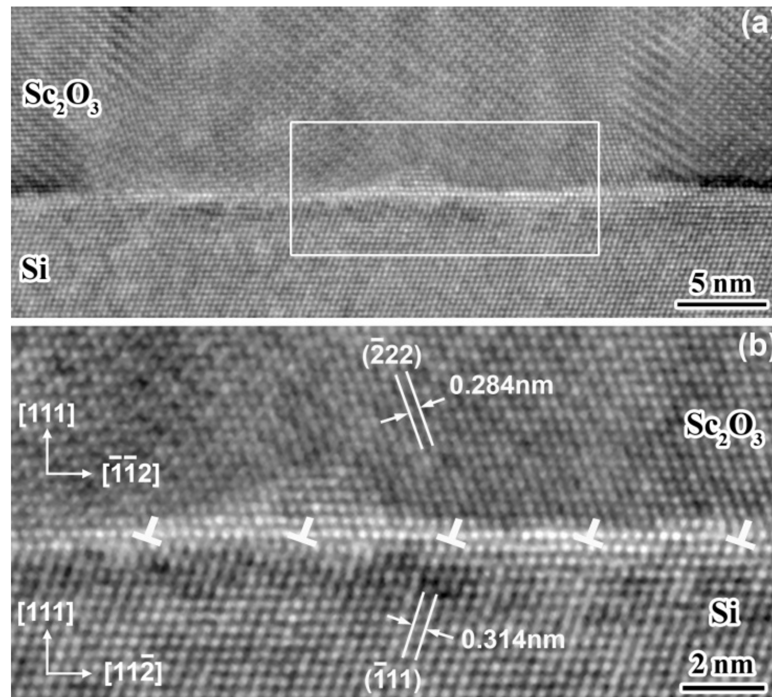


Figure 4.3 (a) HRTEM image of $Sc_2O_3$ film grown on (111) Si. (b) The area marked in (a) under larger magnification. The $Sc_2O_3$ film clearly shows sharp interface with periodic misfit dislocations and B-type domain orientation with respect to Si. The $Lu_2O_3$ and $Gd_2O_3$ films show the same features.

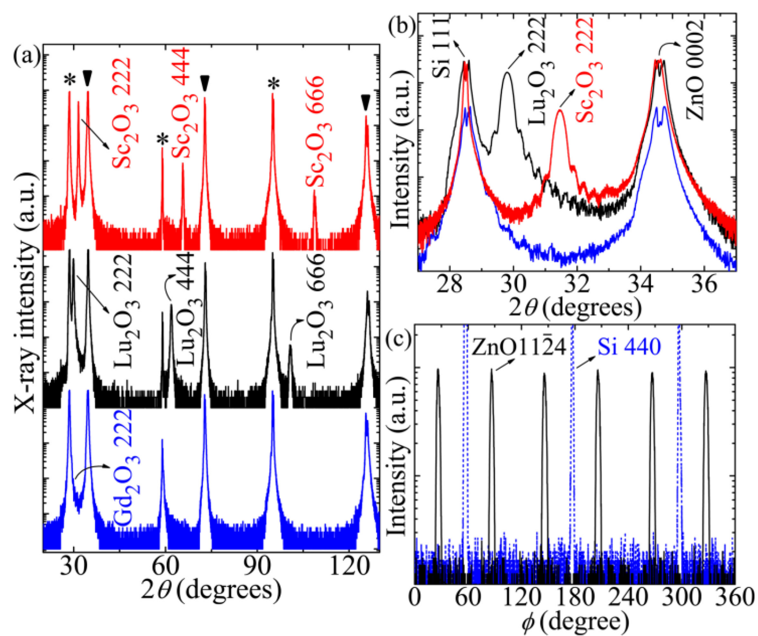


Figure 4.4 (a) XRD $\theta$-$2\theta$ scans (on a log scale) of the ZnO films grown on $Sc_2O_3$/Si (red), $Lu_2O_3$/Si (black), and $Gd_2O_3$/Si (blue). Spectra are vertically displaced for clarity. "*" denotes the 111 series of Si peaks, "▼" denotes the 0001 series of ZnO peaks. The $Gd_2O_3$ peaks are overlapped with strong Si peaks. (b) Enlarged $\theta$-$2\theta$ scans show interference fringes on the $M_2O_3$ 222 peaks, indicating thickness homogeneity and good crystallinity of the $M_2O_3$ layers. The split of strong Si and ZnO peaks are caused by detector saturation. (c) Representative XRD $\phi$-scans (on a log scale) of ZnO $11\bar{2}4$ (black) and Si 440 (blue) peaks from ZnO/$M_2O_3$/Si films.

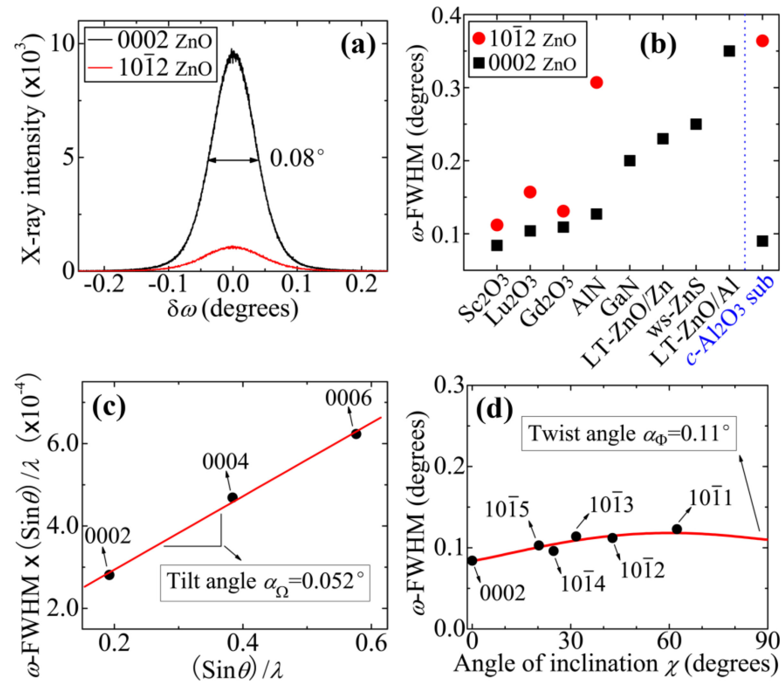


Figure 4.5 (a) XRD ω-scans of ZnO 0002 and 10$\bar{1}$2 reflections of a ZnO film grown on 100 nm $Sc_2O_3$/(111) Si. (b) Comparison of the ω-FWHM values of ZnO 0002 and 10$\bar{1}$2 reflections reported for several films in Table 2.1. The values of a ZnO/*c*-$Al_2O_3$ film grown by the same PLD system are also included. (c) Williamson-Hall plot of ZnO 0001 series of reflections measured from the ZnO/100 nm $Sc_2O_3$/Si film. The slope gives the tilt angle of the film. (d) Plot of ω-FWHM values of ZnO 0002 and off-axis reflections with Srikant method fitting. The extrapolation of the fitting to χ=90° gives the twist angle of the film.

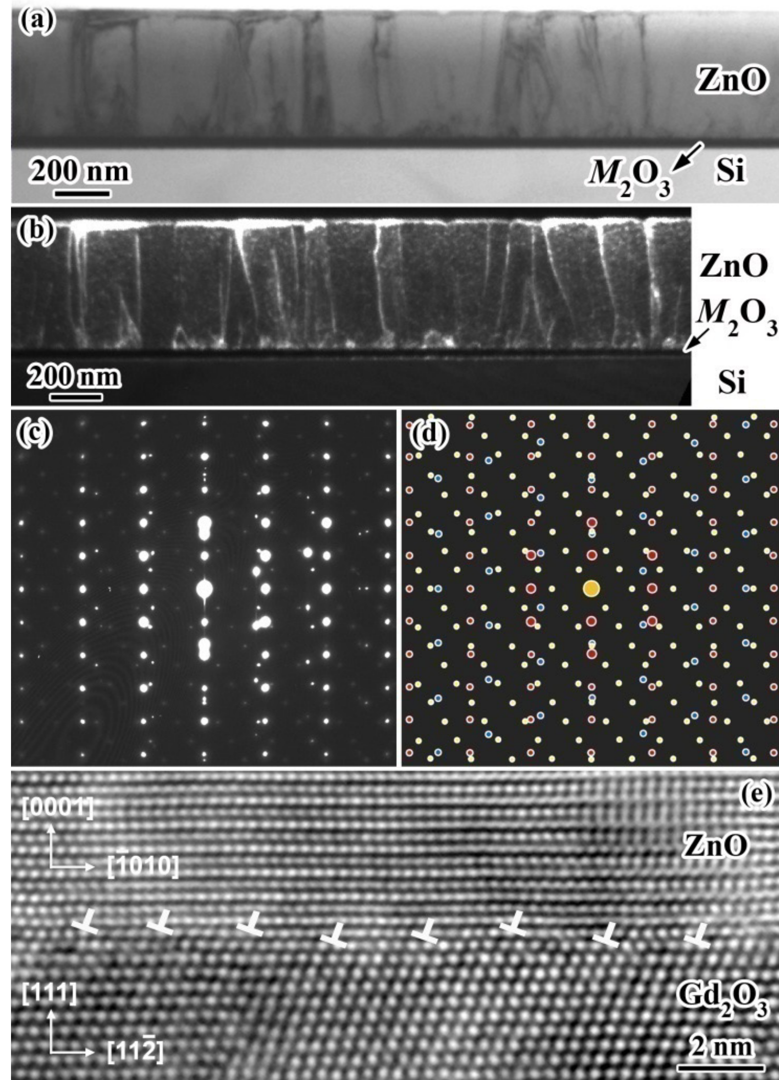


Figure 4.6 (a) Typical cross-sectional TEM image of a ZnO/$M_2O_3$/(111) Si film. The $M_2O_3$ layer in this specimen is a 30 nm thick $Lu_2O_3$ layer. (b) Cross-sectional dark field image of the same area with $\mathbf{g}=10\bar{1}2$. (c) SAED pattern of the interface region under the zone axis of $[1\bar{2}10]_{ZnO}$ ($[1\bar{1}0]_{Si}$). (d) Simulated SAED pattern revealing the overlapping of Si (blue dots), $M_2O_3$ (yellow dots), and ZnO (red dots) patterns. (e) HRTEM image of the ZnO/ $M_2O_3$ interface. The $M_2O_3$ layer in the specimen is a 30 nm thick $Gd_2O_3$ layer.

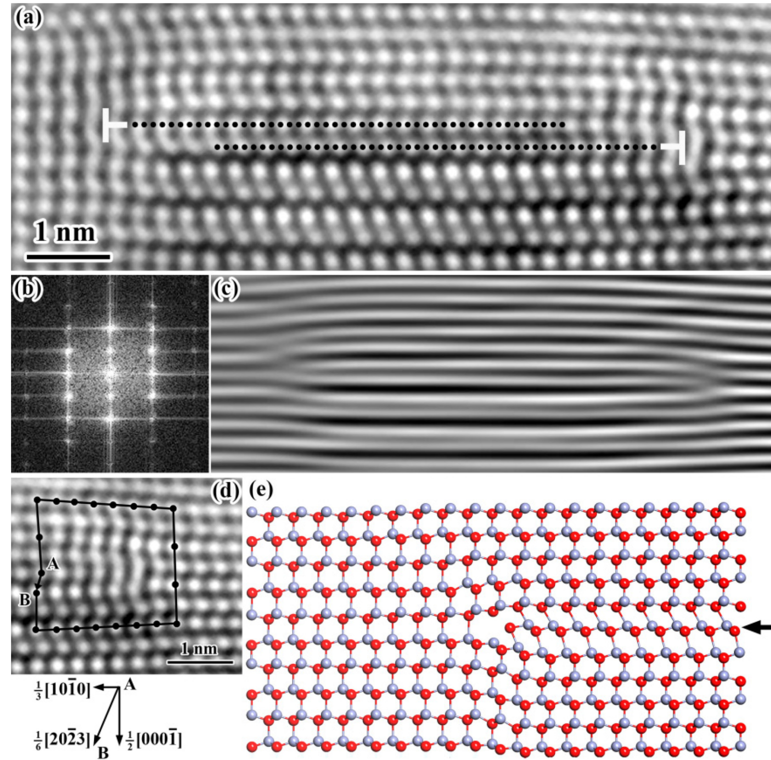


Figure 4.7 (a) HRTEM image taken along zone axis $[11\bar{2}0]$ showing a pair of Frank partial dislocation surrounds a short segment of type $I_1$ stacking fault. The dotted lines indicate insertion of extra (0001) planes. (b) and (c) are the corresponding FFT pattern and iFFT image respectively. (d) A Burgers circuit surrounding one of the end-on Frank partial dislocations, indicating a Burgers vector of **b**=**AB**=$\frac{1}{6}\langle 20\bar{2}3\rangle$. (e) A ball-and-stick model simulation of a plane insertion.

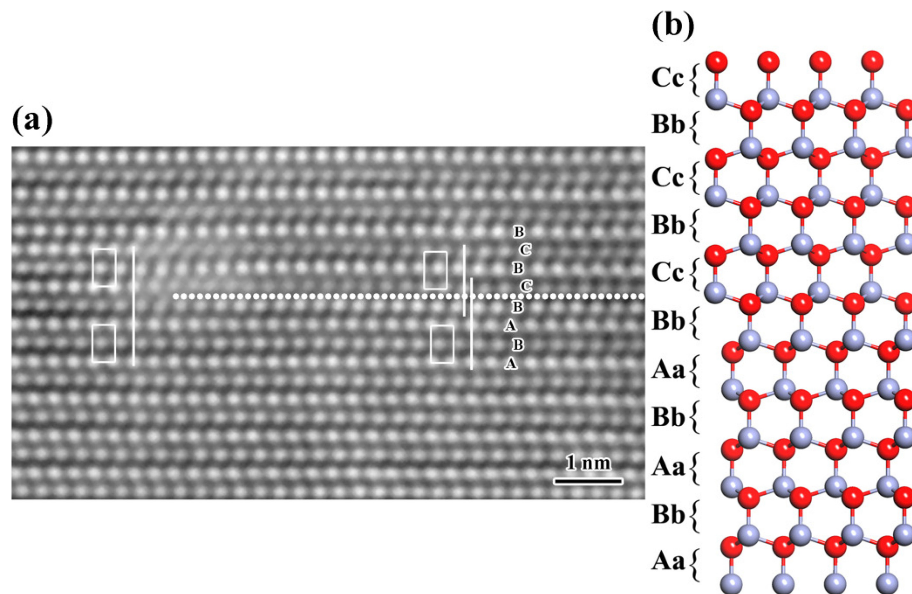


Figure 4.8 (a) HRTEM image (zone axis $[11\bar{2}0]$) of type $I_1$ stacking fault formed by removing one (0001) plane and displacing half crystal by $\frac{1}{3}<10\bar{1}0>$ in the vicinity of an APB. (b) A ball-and-stick model simulation of the stacking fault.

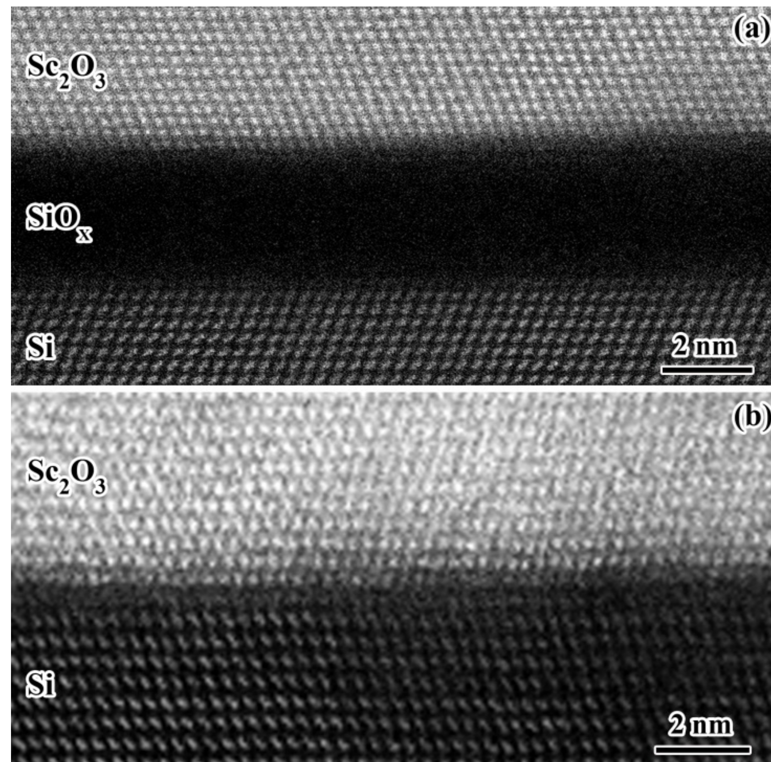


Figure 4.9 $C_S$-corrected HAADF STEM images of the $M_2O_3$/Si interface (a) after the growth and (b) before the growth of ZnO film, respectively. The samples with each of the $M_2O_3$ buffer layers exhibit similar features.

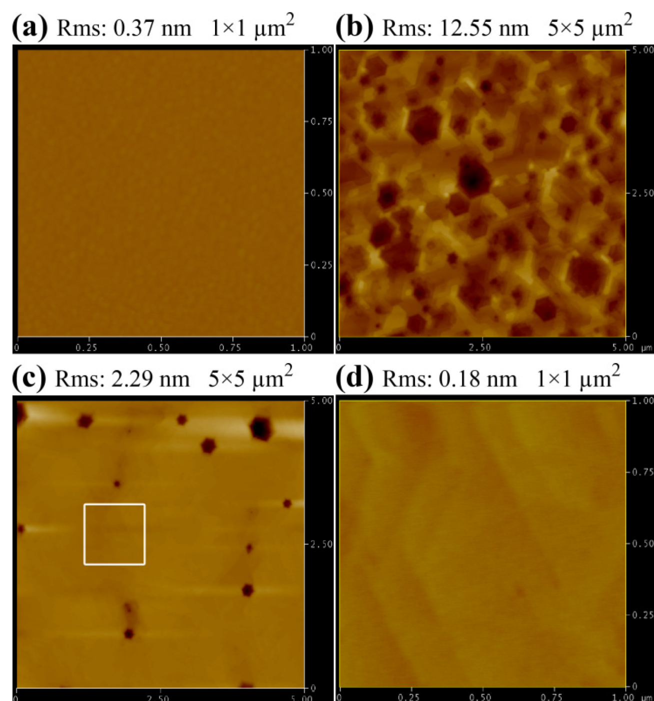


Figure 4.10 AFM images of (a) 30 nm thick $Lu_2O_3$ film grown on (111) Si, (b) 600 nm thick ZnO film grown on the $Lu_2O_3$/Si substrate without the nu-ZnO layer, (c) 800 nm thick ZnO film grow on $Lu_2O_3$/Si with the nu-ZnO layer, and (d) finer scan of the enlarged area marked in (c). "Rms" denotes the root-mean-square roughness of the images.

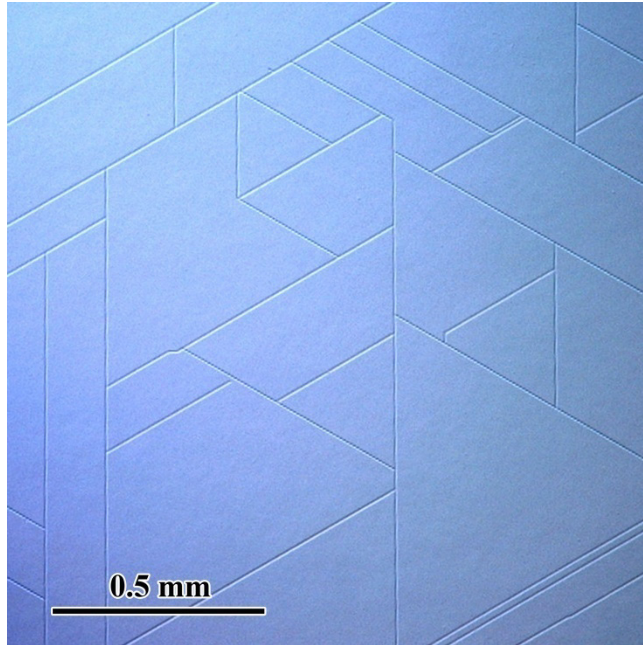


Figure 4.11 Optical microscopic image of a 800 nm thick ZnO film grown on $Lu_2O_3$/Si, showing surface cracks along $<1\bar{2}10>_{ZnO}$ with a density of ~40 $cm^{-1}$.

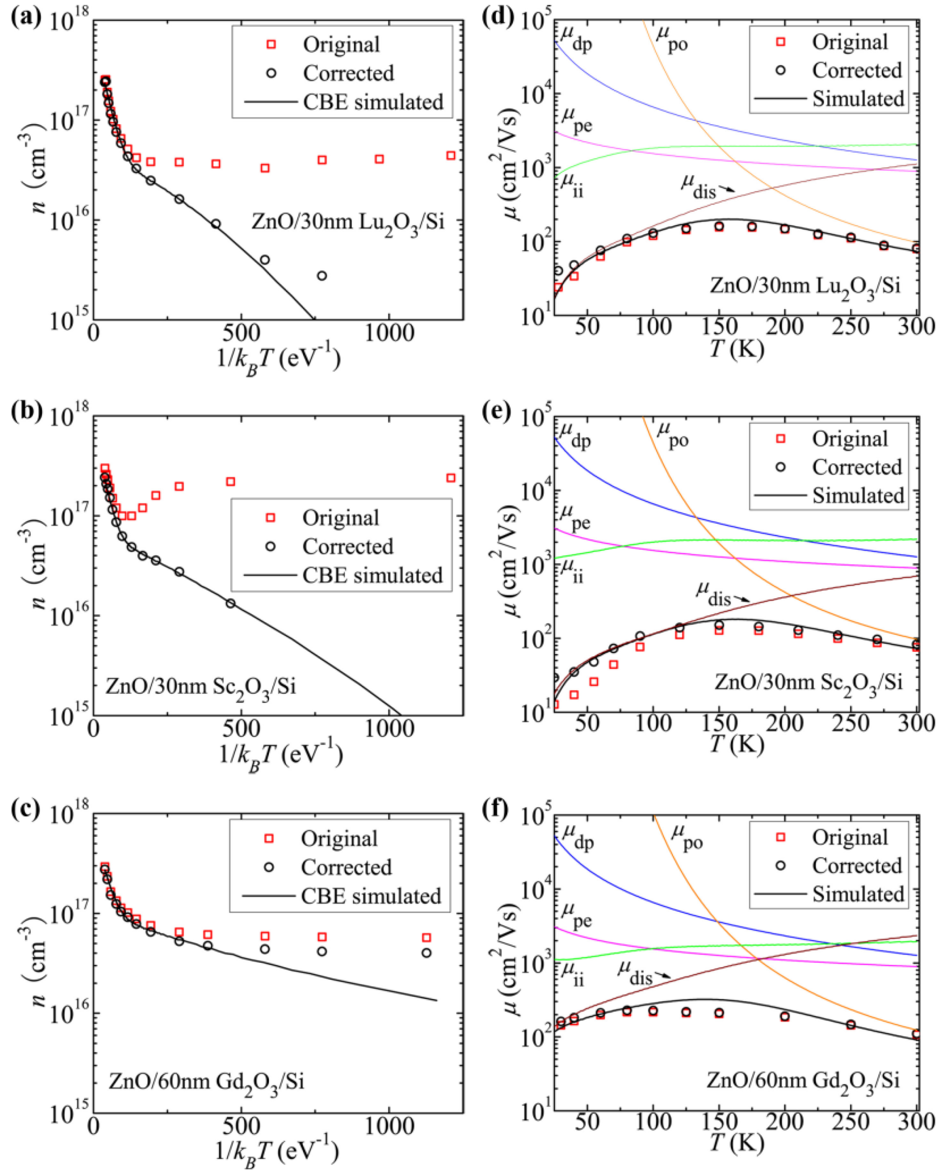


Figure 4.12 Temperature dependence of electron concentrations [(a), (b), (c)] and Hall mobilities [(d), (e), (f)] of ZnO films grown on $M_2O_3$/Si substrates. The red squares are uncorrected experimental data. The black circles and solid lines are corrected bulk electrical data and CBE fit after extraction of a degenerate interfacial layer. The mobilities are fitted by Matthiessen's rules including five different scattering mechanisms (color lines).

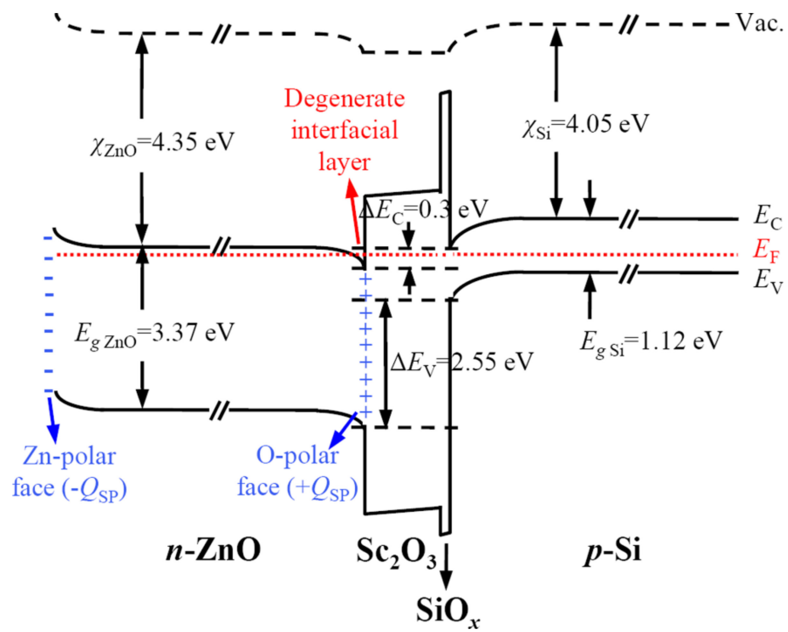


Figure 4.13 Schematic band diagram (drawn to scale) of the ZnO/30 nm $Sc_2O_3$/($SiO_x$)Si sample, indicating band down-bending at the ZnO/$Sc_2O_3$ interface.

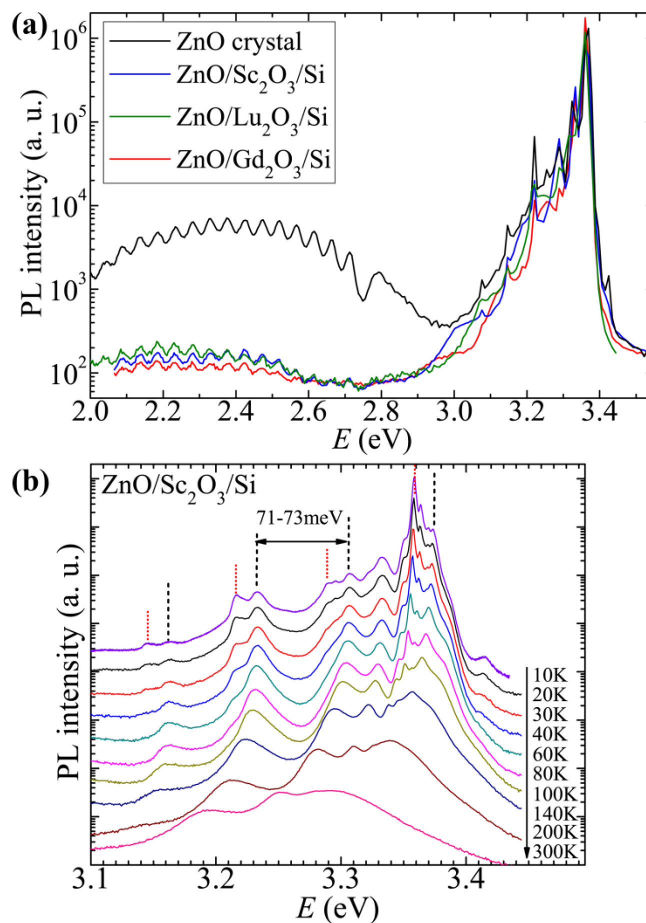


Figure 4.14 (a) Comparison of 10 K PL spectra of a (0001) ZnO single crystal (black line) with those of the ZnO films grown on $M_2O_3$/(111) Si substrates (color lines). (b) Temperature-dependent NBE spectra from 10 K to 300 K of $ZnO/Sc_2O_3/Si$. Spectra are in log scale. Spectra in (b) are vertically displaced for clarity.

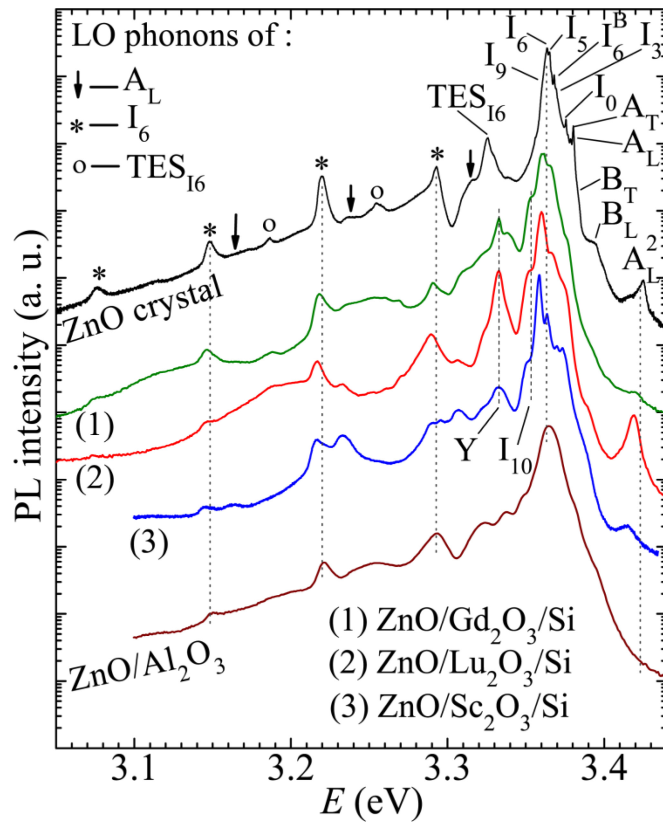


Figure 4.15 Comparison of 10 K NBE spectra of the ZnO single crystal, ZnO film grown on *c*-$Al_2O_3$, and ZnO films grown on $M_2O_3$/Si [(1)-(3)]. Spectra are in log scale and vertically displaced for clarity.

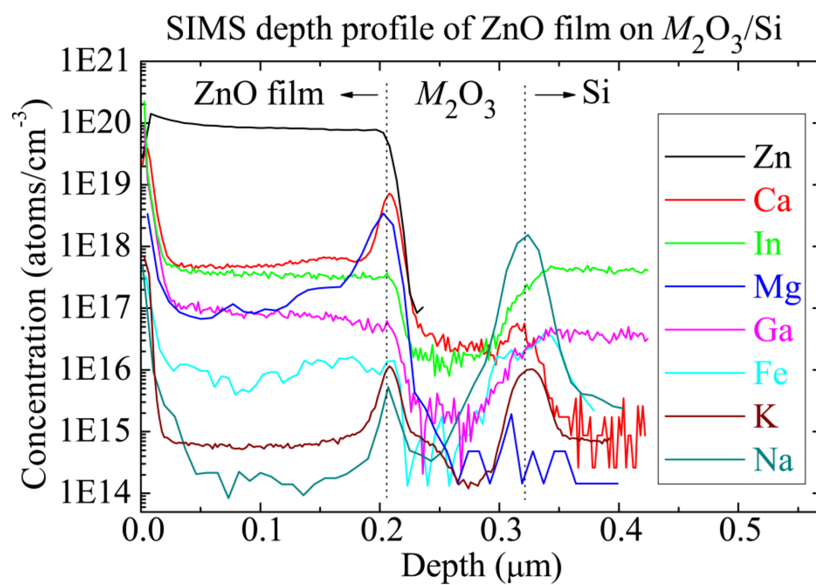


Figure 4.16 Typical SIMS depth profiles of impurities in ZnO/$M_2O_3$/Si thin films.

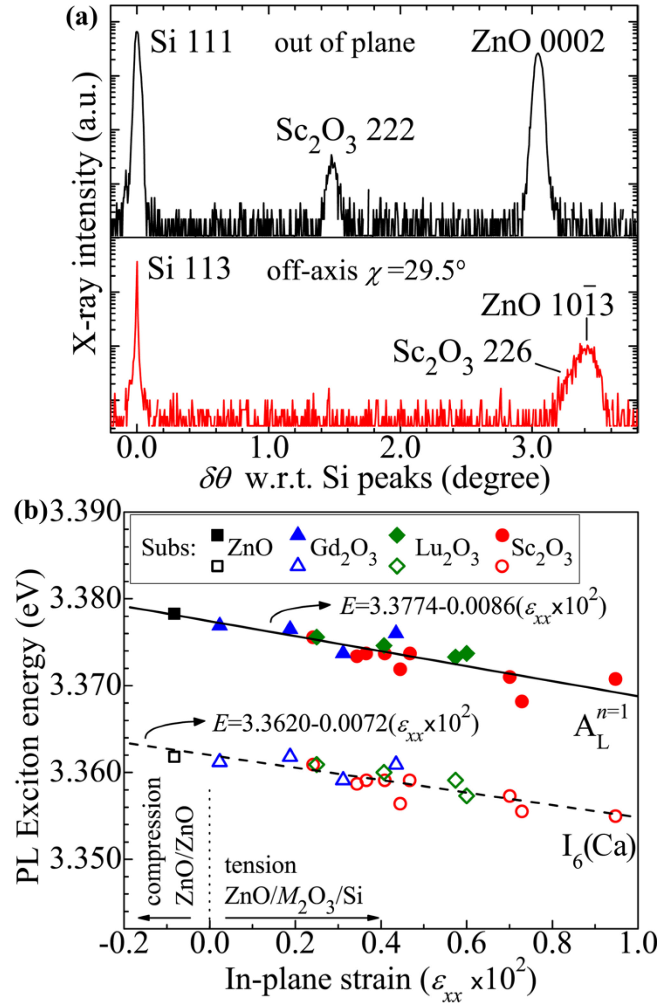


Figure 4.17 (a) High resolution $\theta$-2$\theta$ XRD scans on a ZnO/$Sc_2O_3$/Si film of ZnO 0002 and $10\bar{1}3$ reflections with respect to Si 111 and 113 reflections, respectively. (b) Exciton energies of free A exciton ($A_L^{n=1}$) and neutral Al donor bound exciton ($I_6$) as a function of the in-plane biaxial strain in ZnO/$M_2O_3$/Si films.

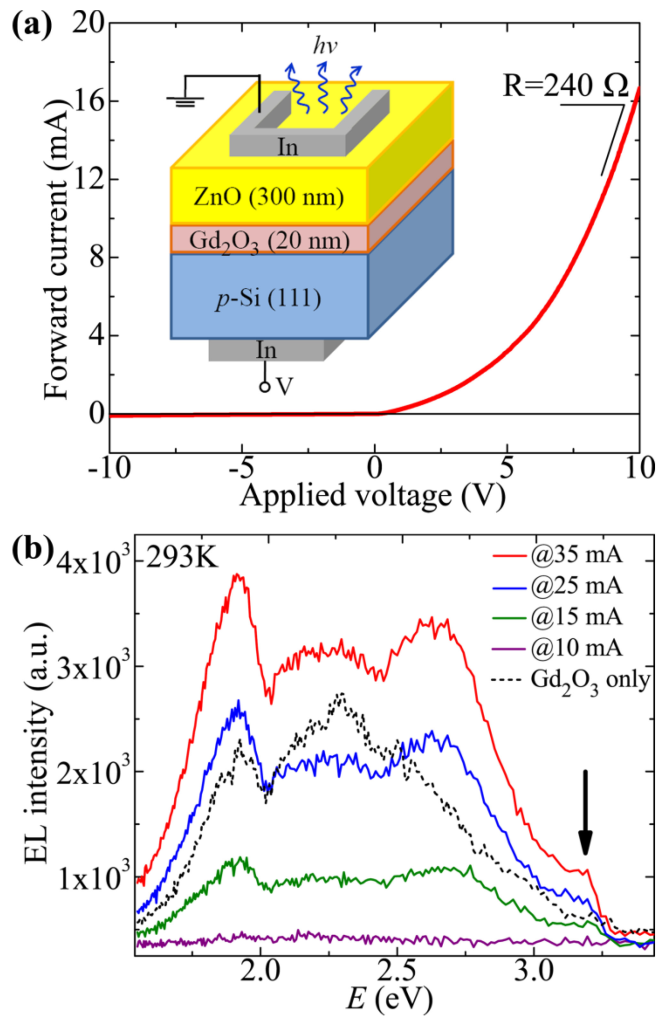


Figure 4.18 (a) I-V characteristics of the ZnO/$Gd_2O_3$/*p*-Si heterostructure. The inset is a schematic diagram of the device under forward bias. (b) EL spectra measured at room temperature from the device operated at different forward currents, showing a weak ZnO NBE emission. The black dashed line is an EL spectrum measured at forward current 100 mA from an ITO/$Gd_2O_3$/*p*-Si structure for comparison.

# Chapter 5

# Strain Engineering of Thick, Crack-free ZnO Films Grown on (111) Si Using Bixbyite Oxide Buffer Layers

As proposed in Section 2.2.2.2, the mismatch of thermal expansion coefficients between ZnO ($6.5\times10^{-6}$ $K^{-1}$) and Si ($2.6\times10^{-6}$ $K^{-1}$) induces inevitable planar tensile strain in the ZnO film during post-growth cooling. The planar tensile strain can result in catastrophic cracking in thick films, and consequently deteriorate device performance. In Section 4.4, we conclude that the cracking critical thicknesses are about 800 nm for the ZnO films grown on $Sc_2O_3$/Si and $Lu_2O_3$/Si, and about 1.4 μm for the films grown on $Gd_2O_3$/Si. In this chapter, the thick ZnO films grown on $Gd_2O_3$/Si are strain engineered to further increase the cracking critical thickness, by using a multi-step growth technique incorporated with insertion of a series of low-temperature grown ZnO interlayers.

## 5.1 Three structures of the ZnO films grown on $Gd_2O_3$/(111) Si

Figure 5.1 shows schematics of three structures of the films. For all three films, the $Gd_2O_3$ buffer layers have a thickness of 60 nm. The subsequent ZnO layers were grown either at a low temperature (LT) of 240 °C with a slow growth rate of 0.2 Å/sec, or at a high temperature (HT) of 600 °C with a growth rate of 1.6 Å/sec.

In structure *a*, a 1 μm thick ZnO film (referred to as the *HT ZnO layer*) was deposited at 600 °C on the $Gd_2O_3$ layer. In structure *b*, prior to the HT ZnO growth, a 10 nm thick LT ZnO layer was first nucleated (referred to as the *LT nucleation layer*) on the $Gd_2O_3$ layer at 240 °C. In structure *c*, after the LT nucleation ZnO and a 670 nm thick HT

ZnO were initially deposited on $Gd_2O_3$, another deposition of 10 nm thick ZnO (referred to as the *LT interlayer*) was performed at 240 °C, followed by a second HT ZnO growth. After this, the LT interlayer and HT ZnO growth was repeated once again, resulting in a periodic ZnO film with a total thickness of around 2 μm.

The crystalline quality and the residual strain of the ZnO films were measured by triple-axis, high-resolution XRD. Table 5.1 lists the FWHM values of the 0002 and $10\bar{1}2$ ZnO $\omega$–rocking curves, the *c*-type and *a*-type dislocation densities, and the compressive strain along the *c*-axis ($\varepsilon_{zz}$). Comparing structure *b* with structure *a*, the film crystallinity is significantly improved by employing the LT nucleation layer, in the way that the FWHM values are about 50% smaller and the dislocation densities are reduced 83%-89%. In addition, the residual strain is reduced by about half. Comparing structure *c* with structures *b* and *a*, the insertion of LT ZnO interlayers is effective in further mitigating the strain to ~20 times less than that of structure *a*, though the crystallinity of structure *c* is slightly degraded from that of structure *b* (dislocation density increases).

Figures 5.2(a) and (b) show the cross-sectional bright field TEM images of a 1.6 μm thick ZnO film with structure *b* and a 2 μm thick ZnO film with structure *c*. The top 200 nm region of the film with structure *b* contains small crack pits with surface opening about 30 nm wide, indicating a cracking critical thickness of about 1.4 μm. However, the 2 μm thick film with structure *c*, containing two LT ZnO interlayers, is crack-free.

### 5.2 Effect of the LT nucleation layer on dislocation reduction and strain relaxation

The effect of the LT nucleation layer is similar to that discussed in Section 2.2 for LT-ZnO buffer layer and in Section 4.2 for nu-ZnO layer. In view of the defect dynamics, the improvement of film crystallinity and the reduction of strain in structure *b* than in structure *a* are accomplished through dislocation gliding and interaction, such as that drawn in the schematic of Figures 5.3(a) and (b). Such process is initiated during the 3D growth of the LT ZnO nucleation layer, and is stimulated by the following temperature ramp-up and HT growth.

Initially, the LT deposition of ZnO 3D-islands on mismatched $Gd_2O_3$/Si substrate induces a strong inhomogeneous strain field,[213] which promotes the nucleation of misfit dislocations. As the lateral overgrowth occurs, this strain field becomes fully relaxed

through subsequent admission of dislocation threading and gliding. During the following temperature ramp-up and HT growth, the dislocations are stimulated to interact with each other or with planar defects, leading to dislocation annihilation near the LT nucleation layer. As indicated by yellow lines in the the schematic of Figure 5.3(b), and corroborated with the cross-sectional bright field TEM image of Figure 5.4(a), the dislocation annihilation results in the improvement of crystallinity (lower dislocation density) in structure *b*, and the observation of dislocation half loops in the interface vicinity. The arrows in Figure 5.4(a) indicate interaction between dislocations. According to such explanation, it is understandable for the observation in Table 5.1 of reduction of FWHM values by 50% and reduction of the dislocation densities by 83%-89% in structure *b* than in structure *a*.

On the other hand, since the strain field in the LT nucleation layer is fully relaxed, due to the thermal expansion mismatch between ZnO and Si, compressive planar strain can be built up in the nucleation layer upon temperature ramp-up, and then preserved in the coherent HT ZnO layer. This compressive strain, during later post-growth cooling, has a significant compensation effect on the tensile strain induced by cooling, thus leads to a smaller residual tensile strain in structure *b* than in structure *a*. The residual tensile strain after cooling in the films is denoted by different color at different thickness in Figure 5.3. Comparing the strain at the same film thickness for structure *a* and *b*, the strain is smaller in structure *b*, corroborating with that observed in Table 5.1. But because the film of structure *b* is much thicker, cracking is initiated at a critical thickness of about 1.4 μm.

Similar results of the effect of LT nucleation layer have also been reported by Amano *et al*.[214,215] regarding reduction of dislocation density in GaN epilayer using a LT GaN buffer layer, and by Han *et al*.[216] regarding strain relaxation in AlGaN epilayer using a LT AlGaN buffer layer.

### 5.3 Effect of the LT interlayer on further strain relaxation

By inserting periodic LT interlayers to the film in the multi-step growth, the film crystallinity degrades in general. Using cross-sectional TEM (not shown), we observed slightly higher dislocation density in structure *c* than in structure *b*, corroborating with the

XRD results in Table 5.1. However, the residual strain is substantially suppressed down to $\varepsilon_{zz}$=-0.01%, and the cracking critical thickness is improved to ≥2 μm. This is because the LT interlayer can modify local strain evolution by introducing additional planar defects and dislocations to the film, as shown in the dark field TEM images of Figures 5.4(b) and (c), where the diffraction vector was selected **g**=0002 (out of plane) and **g**= $20\bar{2}0$ (in plane), respectively. Figure 5.3 (c) also illustrates the additional defects induced by the LT interlayer.

In structure *c*, after the growth of the first (bottom) HT ZnO layer, the film is cooled down to LT. This cooling process induces planar tensile strain to the HT ZnO layer due to the thermal expansion mismatches between ZnO and Si. However, this tensile strain is insufficient to generate cracking due to a film thickness (670 nm) less than the cracking critical thickness (Figure 5.3 (c)). And this tensile strain is not coherently preserved in the subsequently grown LT interlayer, because the LT interlayer is fully strain-relaxed due to its high density of defects. Moreover, the LT interlayer becomes compressively-strained during the temperature ramp-up post to the LT interlayer growth. Consequently, it results in a smaller residual strain in the second coherent HT ZnO layer. As seen in Figure 5.3, the residual tensile strain at the same thickness in structure *c* is much smaller than in structures *a* and *b*, resulting in a nearly strain-free film as observed in Table 5.1. In short, the strain in the upper HT ZnO layer is decoupled from the lower HT ZnO layer by insertion of the LT interlayer, thus the accumulation of tensile in-plane strain in the film is mitigated, leading to an increase of the cracking critical thickness.

It is expected that with proper control of the HT ZnO thickness and the number of LT interlayers, the strain in the film can be kept at a minimum amount, and it is feasible to grow epitaxial ZnO film on the $M_2O_3$/(111) Si substrates to a significant thickness without cracking. Thus this work is important for developing thick-film devices based on epitaxial ZnO films on Si.

### 5.4 Defects introduced by the LT interlayer

The defects in structure *c* have been investigated by TEM based on **g·b** extinction criterion, i.e. the defect contrast is invisible in dark field TEM image if the Burgers vector **b** is perpendicular to the diffraction vector **g**.

It is seen from Figures 5.4(b) and (c) that the *a*-type dislocations with a **b** component of $<10\bar{1}0>$ are of higher density compared with the *c*-type dislocations with a **b** component of <0001>. This is in agreement with the dislocation densities obtained from XRD analyses (Table 5.1). One local region of structure *c* is compared in Figures 5.5(a)-(c) using different **g** of 0002, $20\bar{2}0$, and $10\bar{1}2$, respectively. Figure 5.5(d) is a schematic showing the interaction between several apparent dislocations and planar defects. The orange lines are visible in Figure 5.5(a) but not clearly seen in Figure 5.5(b). The blue lines only show in Figure 5.5(b) but not visible in Figure 5.5(a). We found that the orange threading dislocations are mixed-type dislocations, whose Burgers vector has a component along <0001>. The orange horizontal defects contain a high density of type $I_1$ stacking faults with **b**= $\frac{1}{6}<20\bar{2}3>$. And the blue dislocations of high density in Figure 5.5(d) are pure edge dislocations with Burgers vectors lying in the basal plane.

The defects particularly located in the LT interlayer have been identified by HRTEM studies to be type $I_1$ stacking faults with **b**= $\frac{1}{6}<20\bar{2}3>$. Figure 5.5(e) shows a long segment of such stacking faults in the LT interlayer, surrounded by high density of short segments of stacking faults. Whether these stacking faults are formed during the LT interlayer growth, or they are evolved from short segments of dislocations or high density of point defects, is unclear at current moment and needs detailed systematic study.

In summary, the thick ZnO films grown on $Gd_2O_3$/Si are strain engineered to further increase the cracking critical thickness by using a multi-step growth technique. Employing a LT ZnO nucleation layer provides substantial improvement of crystallinity as well as strain reduction in the film. Insertion of periodic LT ZnO interlayers is effective in further mitigating the planar tensile strain and extending the cracking critical thickness to $\geq 2$ μm. The major threading dislocations in the films are either mixed-type or pure edge dislocations. The defects within the LT ZnO interlayer are identified to be

type $I_1$ stacking faults. These results are important for strain engineering epitaxial ZnO films on Si, and represent a promising step towards the development of thick-film device based on epitaxial ZnO films on Si.

Table 5.1 Comparison of FWHM values of the 0002 and $10\bar{1}2$ ZnO $\omega$-rocking curves, dislocation densities ($N_c$ and $N_a$), and compressive strain along $c$-axis ($\varepsilon_{zz}$) of crack-free ZnO films grown on $Gd_2O_3$/Si with the three structures.

| Films grown on $Gd_2O_3$/Si | 0002 (°) | $10\bar{1}2$ (°) | $N_c$ ($cm^{-2}$) | $N_a$ ($cm^{-2}$) | $\varepsilon_{zz}$ (%) |
|---|---|---|---|---|---|
| (*a*) HT ZnO | 0.18 | 0.28 | $9.0\times10^8$ | $4.8\times10^9$ | -0.24 |
| (*b*) HT ZnO/nucleation ZnO | 0.11 | 0.13 | $1.5\times10^8$ | $5.4\times10^8$ | -0.11 |
| (*c*) (HT ZnO/interlayers)$_{\times2}$ /HT/nucleation | 0.11 | 0.19 | $8.1\times10^8$ | $2.2\times10^9$ | -0.01 |

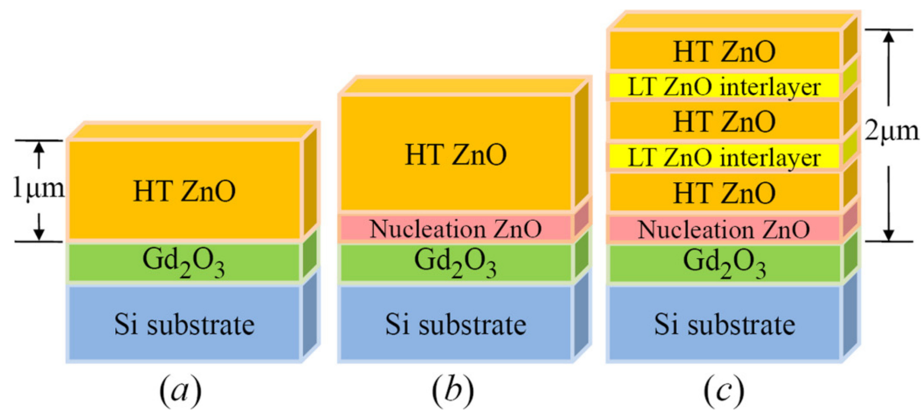


Figure 5.1 Structural schematics of the three ZnO film structures studied in this chapter (not drawn to scale): (*a*) HT ZnO film, (*b*) HT ZnO film grown on a 10 nm LT nucleation ZnO layer, (*c*) HT ZnO film grown on the nucleation layer and inserted with two 10 nm LT ZnO interlayers.

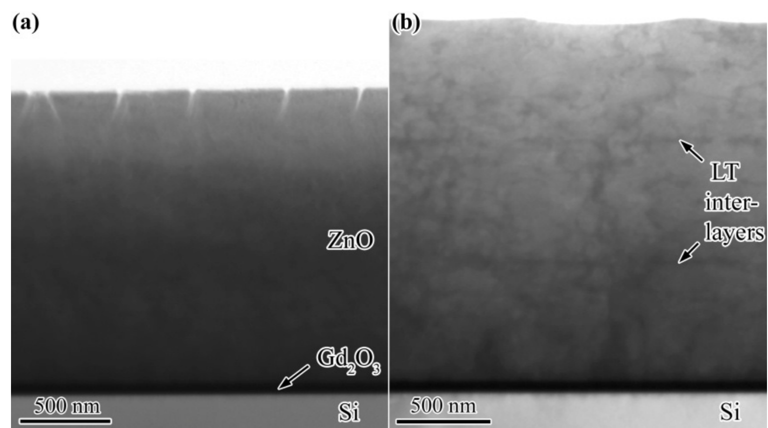


Figure 5.2 Cross-sectional bright field TEM images of the ZnO films on $Gd_2O_3$/Si with (a) structure *b* and (b) structure *c*.

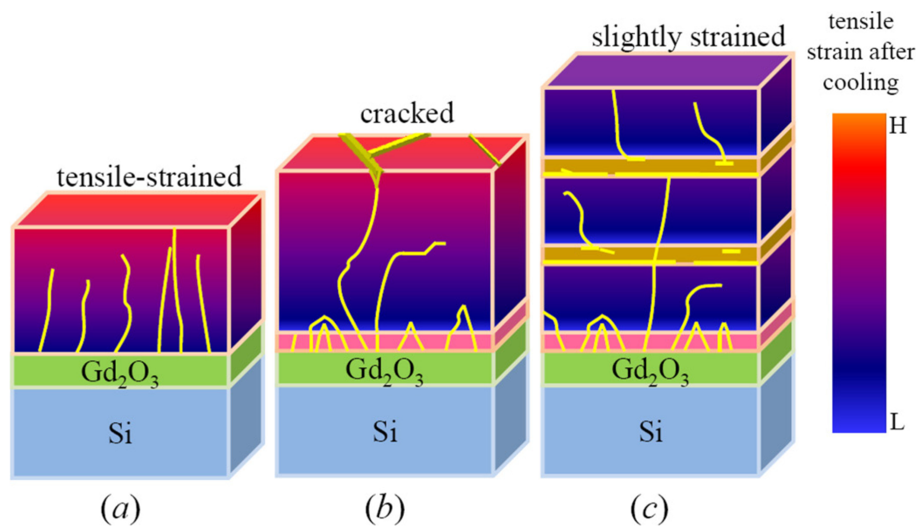


Figure 5.3 Schematic showing the dislocations and residual strain after post-growth cooling in the three ZnO films (not drawn to scale). The tensile strain intensify is denoted by different colors from high (H, red) to low (L, blue).

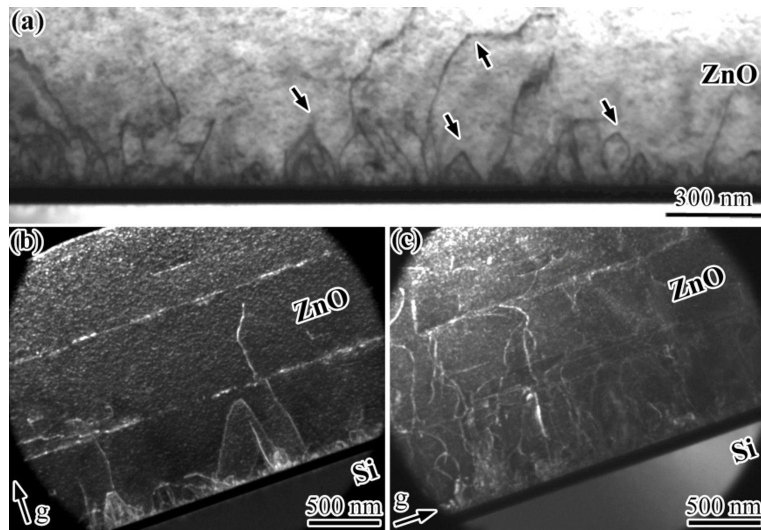


Figure 5.4 (a) Cross-sectional bright field TEM image of the interfacial region containing the LT nucleation layer. Cross-sectional dark field images of the film with structure *c*, with **g**=0002 in (b) and **g**= $20\bar{2}0$ in (c), respectively.

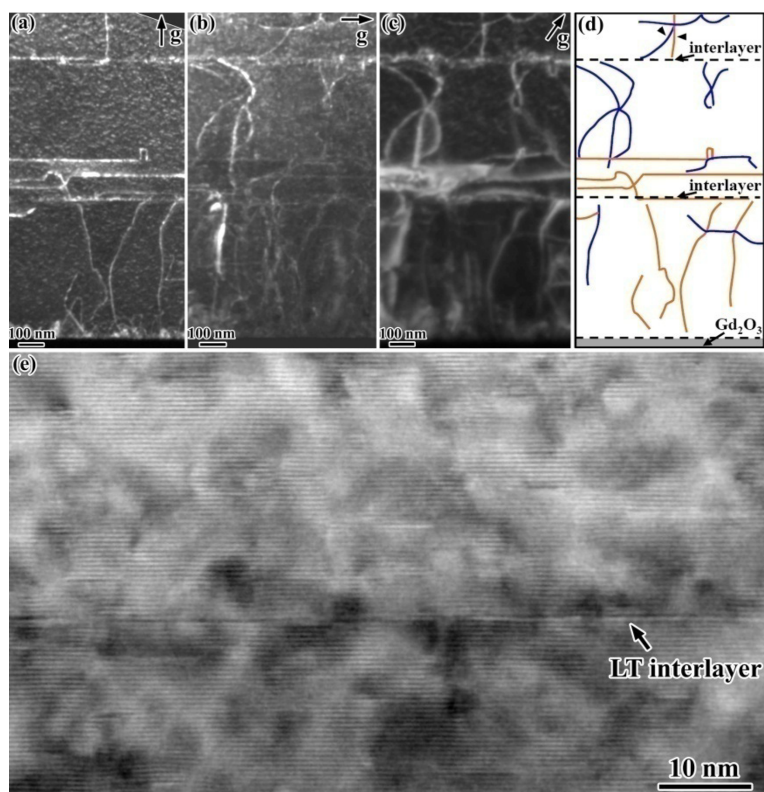


Figure 5.5 Cross-sectional dark field TEM images of a local region of structure *c* using different **g** of 0002 (a), $20\bar{2}0$ (b), and $10\bar{1}2$ (c), respectively. (d) is a corresponding schematic diagram, in which the orange lines are visible in (a) and the blue lines are shown in (b). (e) is an HRTEM image showing a long segment of stacking faults in the LT interlayer.

# Chapter 6

# *P*-type Doping of ZnO Films with Antimony

## 6.1 Introduction to *p*-type doping of ZnO

ZnO is a promising wide band gap semiconductor for short-wavelength and transparent optoelectronic applications. Unfortunately, similar to other wide band gap semiconductor such as GaN and AlN, ZnO suffers from a main obstacle to achieving these applications which is the common doping asymmetry problem. To realize these applications, both *n*- and *p*-type ZnO epilayers with high quality are essential to form the homojunction structure. However, ZnO is intrinsically *n*-type and very difficult to be doped *p*-type.

This doping asymmetry problem originates from the linear dependence of the formation energy of charged compensating defects on the energy position of the Fermi level ($E_F$), as shown in Figure 6.1.[217] Since ZnO has a low valence band maximum (VBM), when *p*-type doping moves $E_F$ close to $E_{VBM}$, the formation energy of charged donor defects drops concurrently and significantly, enhancing the possibility of donor defects formation. Furthermore, the low VBM also induces high ionization energy of these donor defects, leading to significant compensation of the acceptor dopants by the ionized donor defects. In addition to the spontaneous formation of compensating defects, there exist other problems, such as limited dopant solubility and deep level dopants, which can also hinder the *p*-type doping of ZnO.

Based on the understanding of the doping asymmetry problem, it is very challenging to achieve reliable *p*-type doping of ZnO under thermodynamic equilibrium conditions. For example, nitrogen, which has similar ionic radius as oxygen and is theoretically the best *p*-type dopant by substituting oxygen sites in ZnO, however is not

an effective *p*-type dopant. This is due to a low solubility[6] of nitrogen in ZnO, and a significant compensation by donor defects such as oxygen vacancies ($V_O^{2+}$), Zn-antisites-related defect complexes ($(N_O\text{-}Zn_O)^+$), $N_2$ molecules at oxygen sites ($(N_2)_O^{2+}$), and N-$N_2$ complexes ($[N_O-(N_2)_O]^+$).[218]

In the last decade, extensive research has been done to find possible solutions to overcome the *p*-type doping difficulty of ZnO. Promising dopants include P,[219-221] As,[222-224] and Sb,[225-228] which are large-size-mismatched elements and have been consistently reported to yield stable *p*-type doping of ZnO thin films. A theoretical model has been proposed by S. Limpijumnong *et al.*[229] to explain the observed *p*-type conductivity in ZnO doped with large-size-mismatched elements. According to this model, the large-size dopant (X: As or Sb) substitutes the zinc site ($X_{Zn}$) and form a complex with two Zn vacancies ($X_{Zn}$-2$V_{Zn}$). This $(X_{Zn}\text{-}2V_{Zn})^-$ complex acts as an acceptor and would have low formation and ionization energies under oxygen-rich conditions.

Previous to our study of *p*-doping of ZnO, Sb doping of ZnO has not been extensively studied. The feasibility of Sb doping for *p*-type ZnO was reported for a laser-assisted diffusion method between a Sb layer and a ZnO film.[225] Yet the reliability of the conductivity type has been questioned due to the excessively high ionization ratio, hole concentration (~$10^{20}$ $cm^{-3}$), and laser-induced surface damages. Mandalapu *et al.*[226] fabricated a Ga-ZnO/Sb-ZnO/*p*-Si homojunction by molecular-beam epitaxy following the work of Xiu *et al.*[227] who fabricated *p*-type Sb-ZnO on *n*-(100) Si. The low turn-on voltage of the junction (~2 V) is not understood, and the I-V characteristics may be affected by the diffusion of carriers between the *p*-Si substrate and the Sb-ZnO film. In addition, the *p*-type conductivity obtained after *in situ* annealing at 800 °C in vacuum remains questionable since the formation of donors such as zinc interstitials is favorable. Furthermore, the inevitable amorphous $SiO_x$ layer at the ZnO/Si interface and grain boundaries may also affect the electrical properties.

In short, these reports of *p*-type Sb-doped ZnO films grown either on (100) Si or glass substrates show polycrystalline microstructures, and the interpretation of the measured properties is complicated due to the existence of grain boundaries, interfacial secondary phases, dopant segregation, and interdiffusion across interfaces. Therefore, an

epitaxial thin film with well-controlled microstructure may provide significant insights to the conduction mechanism of Sb-doped ZnO. Based on these considerations, in this study we investigated epitaxial Sb-doped ZnO films grown on (0001) $Al_2O_3$ substrates. We also compared the Sb-doped ZnO films grown on (111) Si with the bixbyite oxide buffer layers and those grown on (100) Si substrates.

### 6.2 Sb-doped ZnO thin films grown on (0001) $Al_2O_3$ substrates

Sb-doped ZnO thin films with nominal thickness of 400 nm were grown in the Neocera PLD chamber at 400 °C and 600 °C. The ZnO targets, with nominal 0.2 at.% and 1 at.% Sb doping concentration, were homemade as described in section 3.1.4 and have high densities of 93-97%. During deposition, 50 mTorr $O_2$ was backfilled into the growth chamber.

Figures 6.2(a) and (b) show the RBS spectra of the Sb-doped ZnO films grown with 1 at.% and 0.2 at.% Sb-doped targets. The large flat steps are attributed to O, Zn, and Sb signals according to their energy positions. The RBS intensity correlates with the atomic concentration (stoichiometry) in the films. Figures 6.2(c) and (d) are the enlarged areas of interest in log scales, clearly showing the flat steps of Sb signals. The spectra were simulated by SIMNRA analysis,[149] giving approximate Sb doping concentrations of 0.1±0.03 at.% in films deposited using the 0.2 at.% Sb-doped target, and 0.95±0.03 at.% in films deposited using the 1.0 at.% Sb-doped target. The flat steps indicate uniform distribution of the Sb element in the films. The small peak appears at the high energy side of the Sb step in Figure 6.2(d) implies surface segregation of the Sb element.[230]

Figure 6.3(a) shows a $\theta$-$2\theta$ XRD pattern of a Sb-ZnO film deposited at 600°C, which is typical of all Sb-doped ZnO samples. The out-of-plane orientation relationship is $(0001)_{ZnO}||(0001)_{Al_2O_3}$. No extra ZnO or impurity peaks are detected. The ZnO $11\bar{2}4$ $\phi$-scan in Figure 6.3(b) clearly indicates the six-fold symmetry of ZnO and the 30° lattice rotation between ZnO and $Al_2O_3$. These studies show that the Sb-doped ZnO films grown on (0001) $Al_2O_3$ are epitaxially. For 1.0 at.% Sb-ZnO films, the full width at half-maximum (FWHM) value of the ZnO 0002 $\omega$-rocking curve is 0.79° for films grown at 600 °C and 1.3° for those grown at 400 °C. For 0.1 at.% Sb-ZnO films, the FWHM values narrow down to 0.5° (600 °C) and 1.0° (400 °C). These values are reasonable

considering the degradation of the film crystallinity caused by a large-size dopant and the high growth pressure.[231]

All Sb-doped ZnO films have an average optical transparency of 80-85% in the visible region as shown in the typical optical transmittance spectra (Figure 6.4). The sharp absorption edge redshifts when the Sb doping concentration increases. A Tauc plot[165] (inset of Figure 6.4) of the squared absorption coefficient ($\alpha^2$) as a function of the energy $h\nu$ yields a direct optical band gap energy of 3.30 eV, 3.28 eV and 3.26 eV for undoped, 0.1 at.% and 1.0 at.% Sb-ZnO respectively. The observed band gap reduction indicates the formation of Sb-related impurity states.

Table 6.1 compares the room temperature electrical properties of undoped and Sb-doped ZnO samples. The 0.1 at.% Sb-doped films show higher electron concentrations and lower resistivities than the undoped ones. This phenomenon can be explained as follows: (1) the acceptors introduced by 0.1 at.% Sb doping can not compensate the native donors in ZnO; and (2) Sb doping does introduce donor-like defects to minimize the buildup in strain energy.[229] However, when the Sb concentration is increased to 1.0 at.%, reliable *p*-type conductivity is confirmed. The film grown at 400 °C shows a resistivity of 63.6 Ω cm, a hole concentration of $2.2\times10^{17}$ $cm^{-3}$ and a mobility of 0.5 $cm^2$/V s. When the growth temperature increases to 600 °C, the mobility increases to 7.7 $cm^2$ while resistivity and hole concentration decrease to 4.2 Ω cm and $1.9\times10^{17}$ $cm^{-3}$ respectively.

The temperature dependence of the hole concentration of 1.0 at.% Sb-doped ZnO film deposited at 400 °C is shown in Figure 6.5. A similar result was obtained for the film deposited at 600 °C. The hole concentration exhibits a three orders of magnitude change above 100 K. This abrupt increase of hole concentration with the temperature indicates that above 100 K, Sb-induced acceptors are gradually activated. As shown in the inset of Figure 6.5, a least-squares fit to the Arrhenius plot of $p/T^{3/2}$ between 133 K and 300 K gives a thermal activation energy $E_A$=115±5 meV. More accurately, assuming an effective hole mass $m_p$=0.64$m_0$ and a relative static dielectric constant $\varepsilon_S$ =8.12,[156] a simulation of the data based on a single-donor/single-acceptor model of CBE equation (equation 3.20) gives rise to $N_D=5.5\times10^{17}$ $cm^{-3}$, $N_A=6\times10^{18}$ $cm^{-3}$ and $E_A$=120±5 meV.

The values of the activation energy $E_A$ obtained are close to the theoretical binding energy of a hydrogen-atom-like acceptor, 130~135 meV, in ZnO.[232,233]

For *p*-type semiconductors, the acceptor thermal activation energy $E_A$ is dependent on the hole concentration at high temperature. Similar to the discussion in section 4.6.1 the thermal activation energy $E_A$ and the acceptor optical ionization energy are related by $E_{A0}=E_A+\alpha N_A^{1/3}$.[234] From $E_A$=115±5 meV at 300 K, we derive an optical ionization energy of $E_{A0}$=158±7 meV for our *p*-type Sb-doped ZnO films. This value is in good agreement with the theoretical ionization energy of the complex acceptors ($Sb_{Zn}$-$2V_{Zn}$) predicted by first principles calculations (160 meV),[229] and with experimental results of PL measurements (140 meV).[235] From our optical transmittance and Hall-effect measurements, we conclude that Sb doping in ZnO forms an acceptor state of 158±7 meV above the valence band, and that in order to achieve *p*-type conductivity, the acceptor has to have sufficient ionization ratio to overcome the residual donor concentration in ZnO.

To understand *p*-type conduction mechanisms, the microstructures and crystal defects of the Sb-doped ZnO films were studied by high resolution XRD. The density of *c*-type dislocations (mostly screw dislocations and dislocation loops associated with stacking faults) and the density of *a*-type dislocations (mostly threading dislocations) calculated from the tilt and twist angles are compared in Table 6.2 for undoped, *n*-type and *p*-type Sb-doped ZnO films. The dislocation densities increase dramatically as the Sb concentration increases. Compared with undoped ZnO, the *p*-type 1.0 at.% Sb-doped film has a dislocation density 1-2 orders of magnitude higher. In other words, while degrading the film crystal quality, the high density of dislocations may enhance the solubility of Sb dopants by trapping Sb in the vicinity of dislocation lines.

The microstructures of both undoped ZnO and *p*-type Sb-doped films were also studied by TEM (Figures 6.6(a) and (b)). The results show a high density of threading dislocations originating from the film/substrate interface in *p*-type Sb-doped ZnO film. In addition to threading dislocations, there is a large number of partial dislocation loops associated with small stacking faults as shown in the HRTEM image of Figure 6.6(c). Figure 6.6(d) zooms in a marked area, showing the atomic detail of the partial dislocations and the stacking faults in the *p*-type Sb-doped film. According to our TEM

observations, we suggest that $Sb_{Zn}$ can bind with Zn vacancies near the dislocation cores and form $Sb_{Zn}$-$2V_{Zn}$ complex acceptors which lead to *p*-type conductivity.

The surface morphologies studied by AFM corroborate the result of TEM studies. Figure 6.7 shows the AFM images of 0.1 at.% and 1.0 at.% Sb-doped ZnO films grown at 400 °C and 600 °C, respectively. The rough surface and small particle sizes suggest a 3-D growth mode of the films, which is induced by the high growth pressure and Sb doping, and is consistent with the high density of threading dislocations observed by TEM.

In addition, the spectrum of XPS measurement (Figure 6.8) clearly shows two $Sb3d_{3/2}$ peaks located at 538.459eV and 536.827 eV, indicating Sb-O bonding with Sb valance states of $Sb^{5+}$ and $Sb^{3+}$ in the film. This result also supports that $Sb_{Zn}$-$2V_{Zn}$ is the most possible acceptor, because neither $Sb_2O_5$ nor $Sb_2O_3$ related phase was observed in XRD or TEM results. The deconvolution of the spectrum also show three O 1s peaks indicating different bonding with $Zn^{2+}$, $Sb^{5+}$, and $Sb^{3+}$. Note that the spectrum has a redshift of ~2 eV due to alignment in XPS measurement. We believe that, the oxygen-rich growth conditions play an important role to lower the formation energy of the complex acceptors, by accelerating the generation of Zn vacancies and their diffusion to the dislocation vicinity.

Figure 6.9 shows the temperature dependent PL spectra of a 0.1 at.% Sb-doped ZnO film grown at 600 °C. Due to the Sb doping and the degradation of the film crystallinity, instead of observing the characteristic fine lines of free exciton and bound exciton transitions at 11 K, we only observed an envelope spectrum consists of free excitons (FX), bound excitons (BX), TES, and LO phonon transitions. The spectra redshift about 16 meV from the PL spectrum of the ZnO single crystal (Table 4.5) possibly due to laser-stimulated high density free carriers, which can induce band gap renormalization[200] and/or Burstein-Moss effect[201]. Whether the BX transition includes excitons bound to donors (DX) or acceptors (AX) or both are inconclusive at the current stage.

In conclusion, we fabricated epitaxial *p*-type Sb-doped ZnO films by PLD under high oxygen pressure. High density of dislocations was revealed in the *p*-type films. The *p*-type conductivity results from conjugated effects of high oxygen pressure, adequate doping concentration, and dislocation-facilitated formation of complex acceptors. The *p*-

type films have a resistivity of 4.2-60 Ω cm, a Hall mobility of 0.5-7.7 $cm^2/V$ s, and a hole concentration of $(1.9\text{-}2.2)\times10^{17}$ $cm^{-3}$. The thermal activation energy of the Sb acceptor is 115±5 meV and its optical ionization energy is estimated 158±7 meV.

### 6.3 Sb-doped ZnO thin films grown on Si substrates

Sb-doped ZnO films with *p*-type conductivity were also achieved on (100) Si substrates. In order to eliminate the affection of the substrate conductivity to the electrical measurements of the ZnO films, the native amorphous $SiO_2$ layer (~600 nm thick) was preserved on the substrate prior to the growth. Oxygen plasma (power 150 W) was employed to ensure oxygen-rich conditions in the films, favoring the formation of Sb acceptor complexes. The backfilled oxygen pressure, however, was limited $6.7\times10^{-5}$ mbar (0.05 mTorr) for the benefit of the plasma source. The growth temperature was 550 °C. The Sb doping in the target was 0.2 at.%.

Hall effect measurements show that, a 200 nm thick Sb-doped ZnO film grown on (100) Si with native oxide exhibits *p*-type conductivity with a resistivity of 44.2 Ω cm, a Hall mobility of 4.3 $cm^2/V$ s, and a hole concentration of $3.2\times10^{16}$ $cm^{-3}$, as shown in Table 6.3. The film is polycrystalline with a rough surface (rms=16.9 nm). Table 6.3 also compares an epitaxial Sb-doped ZnO film grown under the same conditions on (111) Si substrate with epitaxial $Sc_2O_3$ buffer layers. It is *n*-type with a resistivity of 1.9 Ω cm, a Hall mobility of 13 $cm^2/V$ s, an electron concentration of $2.6\times10^{17}$ $cm^{-3}$, and a smooth surface (rms=2.0 nm). The *n*-type conductivity of epitaxial films on $Sc_2O_3$/(111) Si implies that the doping introduced acceptors in epitaxial ZnO films did not effectively compensate the native donors, possibly due to inadequate Sb doping amount or a higher formation energy of the acceptor complex caused by a lack of $V_{Zn}$. This also corroborates with the fact that threading dislocations, which are suggested to provide $V_{Zn}$, are much less in epitaxial ZnO films than in polycrystalline films.

Our work is consistent with others described in sections 2.1.1 and 2.2.1, in that it is fairly easy to realize *p*-type doping in polycrystalline ZnO films grown on (100) Si substrates. However, it is more challenging but essential to explore *p*-type doping of epitaxial ZnO films grown on (111) Si substrate with the bixbyite oxide buffer layers.

Table 6.1 Electrical properties at RT of undoped ZnO, 0.1 at.% and 1.0 at.% Sb-doped ZnO films grown on (0001) $Al_2O_3$.

| Sb doping (at. %) | Growth $T$ (°C) | Carrier type | $\rho$ (Ω cm) | $n$ ($cm^{-3}$) | $\mu$ ($cm^2$/V s) |
|---|---|---|---|---|---|
| Undoped | 400 | *n* | 0.8 | $2.7\times10^{17}$ | 29 |
| Undoped | 600 | *n* | 1.7 | $7.9\times10^{16}$ | 47 |
| 0.1 | 400 | *n* | 0.4 | $8.5\times10^{17}$ | 18 |
| 0.1 | 600 | *n* | 0.2 | $3.5\times10^{18}$ | 9 |
| 1.0 | 400 | *p* | 60 | $2.2\times10^{17}$ | 0.5 |
| 1.0 | 600 | *p* | 4.2 | $1.9\times10^{17}$ | 7.7 |

Table 6.2 Tilt, twist angles and calculated *c*- and *a*-type threading dislocation densities for 400 nm thick undoped, 0.1 at.% and 1.0 at.% Sb-doped ZnO films grown on (0001) $Al_2O_3$ at 600 °C.

| Sb doping (at. %) | $\alpha_\Omega$ (°) | $\alpha_\Phi$ (°) | $N_c$ (cm$^{-2}$) | $N_a$ (cm$^{-2}$) |
|---|---|---|---|---|
| Undoped | 0.22 | 0.24 | $1.2\times10^9$ | $3.2\times10^9$ |
| 0.1 (*n*-type) | 0.51 | 0.56 | $6.8\times10^9$ | $2.1\times10^{10}$ |
| 1.0 (*p*-type) | 0.97 | 1.29 | $2.4\times10^{10}$ | $1.1\times10^{11}$ |

Table 6.3 Comparison of electrical properties at room temperature of 0.1 at.% Sb-doped ZnO films grown on (100) Si and (111)Si with $Sc_2O_3$ buffer layer.

| Substrate | Film microstructure | Surface rms (nm) | Carrier type | $\rho$ (Ω cm) | $n$ ($cm^{-3}$) | $\mu$ ($cm^2$/V s) |
|---|---|---|---|---|---|---|
| $SiO_2$/ (100)Si | polycrystalline | 16.9 | *p* | 44.2 | $3.2\times10^{16}$ | 4.3 |
| 30 nm $Sc_2O_3$/ (111) Si | epitaxial | 2.0 | *n* | 1.9 | $2.6\times10^{17}$ | 13 |

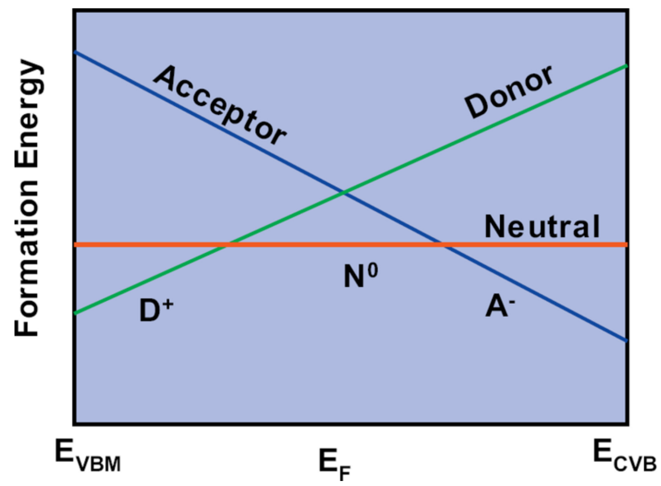


Figure 6.1 Schematic of formation energies of charged defects vs. the Fermi energy position of wide band gap semiconductors. (from Yan and Wei [217])

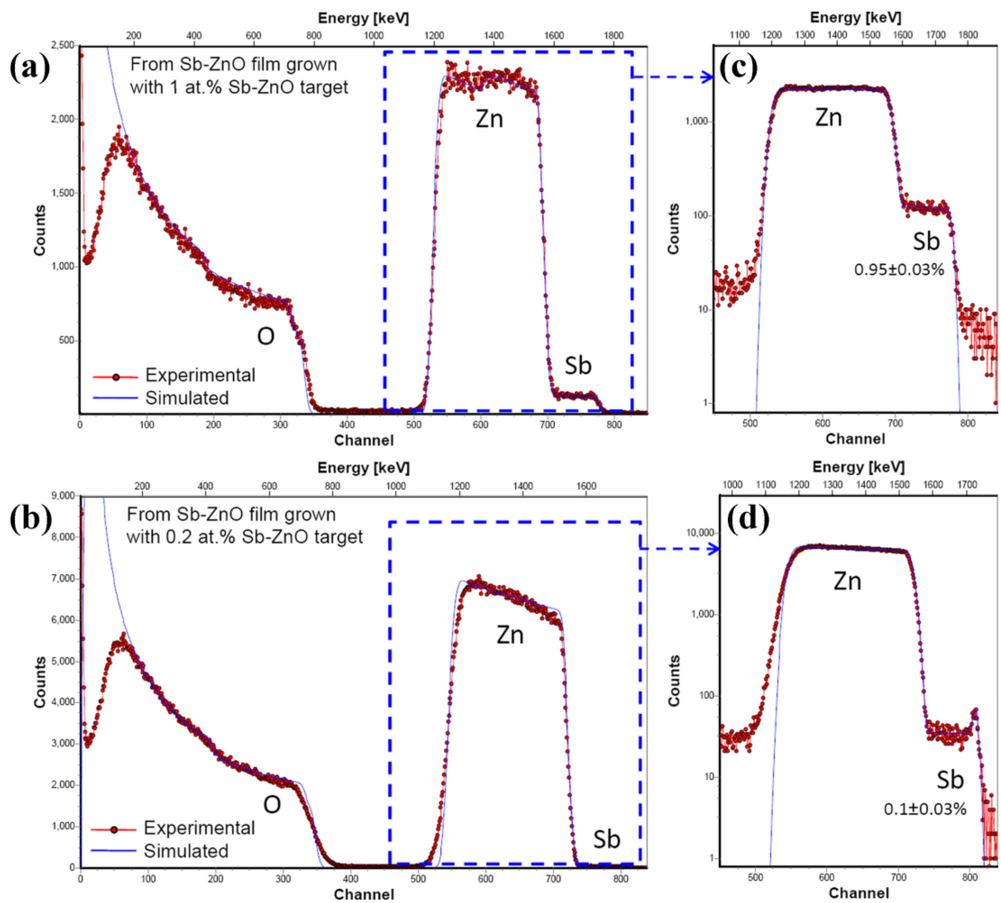


Figure 6.2 RBS spectra of the Sb-doped ZnO films on $Al_2O_3$ substrates. The Sb concentrations are estimated about 1.0 at.% and 0.1 at.% for the films grown with 1 at.% and 0.2 at.% Sb-doped ZnO targets, respectively.

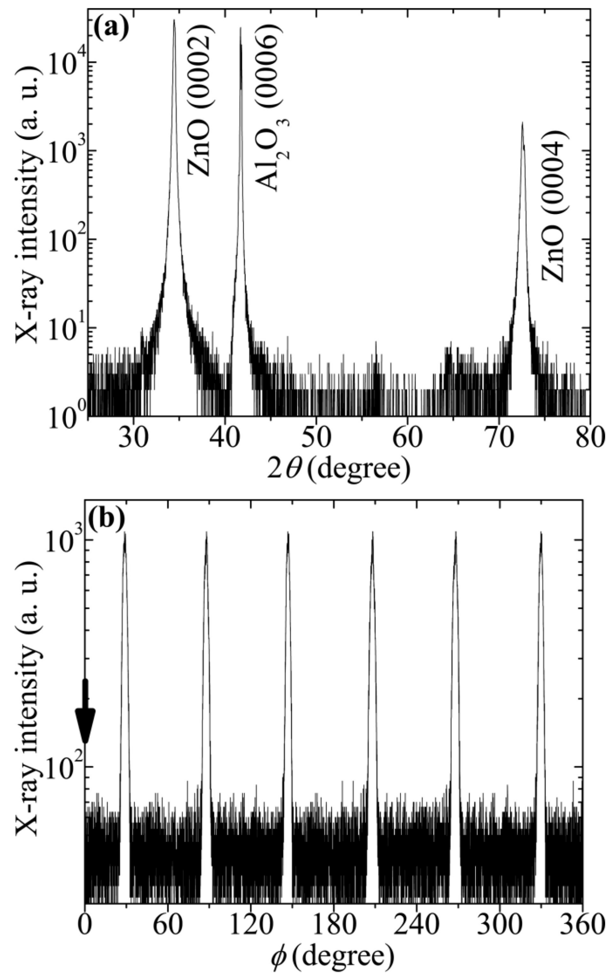


Figure 6.3 Typical XRD $\theta$-2$\theta$ (a) and $11\bar{2}4$ $\phi$ (b) scans of 1.0 at.% Sb-doped ZnO films grown at 600 °C. The arrow indicates the position of one of the $Al_2O_3$ $11\bar{2}4$ peak.

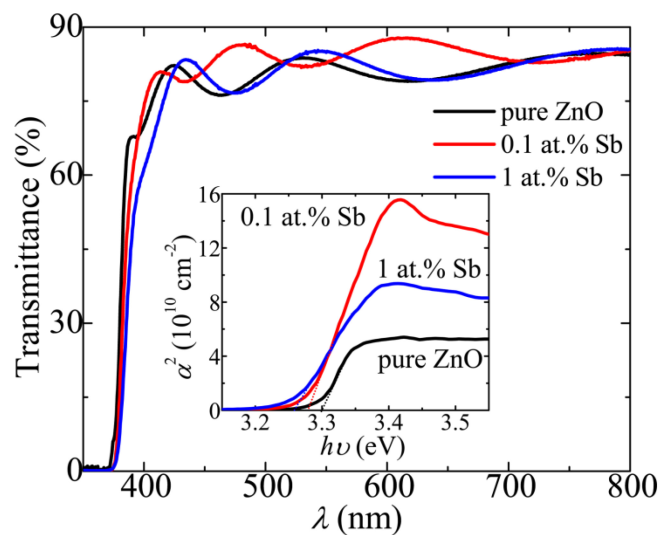


Figure 6.4 Optical transmittance spectra and Tauc plots (inset) of undoped ZnO, 0.1 at.% and 1.0 at.% Sb-doped ZnO films.

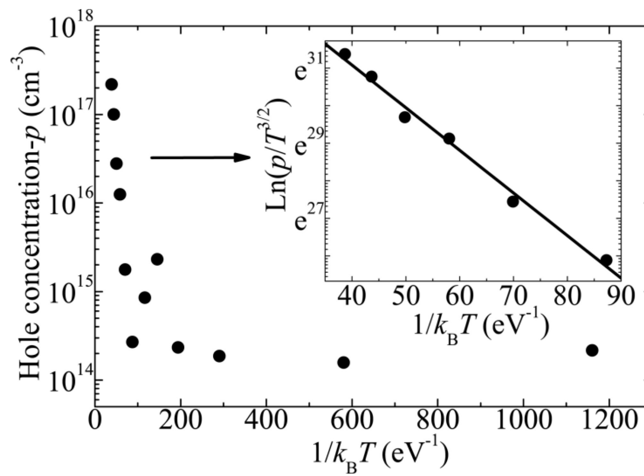


Figure 6.5 Temperature dependence of the hole concentration for 1.0 at.% Sb-doped ZnO films grown at 400 °C. The inset shows a plot of $\ln(p/T^{3/2}) \sim 1/k_B T$ from 133 K to 300 K. The slope gives a thermal activation energy of $115 \pm 5$ meV.

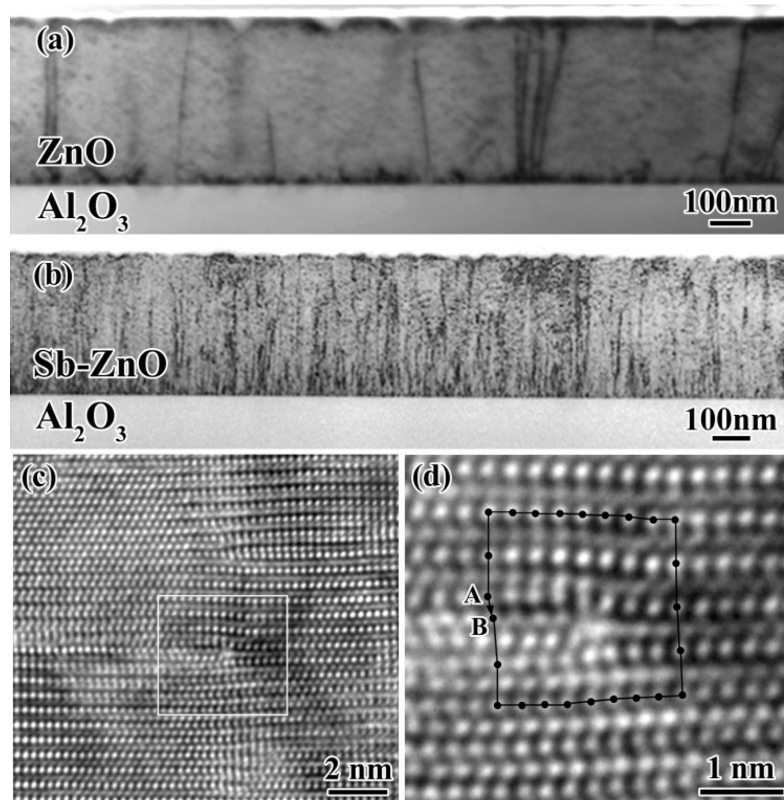


Figure 6.6 Cross-sectional TEM image of (a) undoped ZnO and (b) 1.0 at.% Sb-dope films. High resolution TEM images ((c) and (d)) of 1.0 at% Sb-ZnO film showing partial dislocations associated with stacking faults. The Burgers vector is $\frac{1}{6}[02\overline{2}\overline{3}]$.

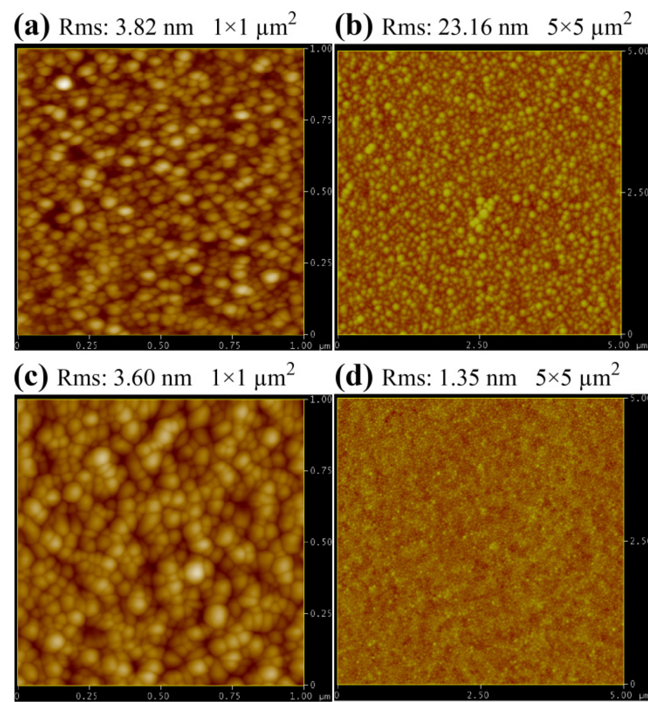


Figure 6.7 AFM images of 0.1 at.% Sb-doped films grown at (a) 400 °C and (b) 600 °C, and 1.0 at.% Sb-doped films grown at (c) 400 °C and (d) 600 °C. "Rms" denotes the root-mean-square roughness of the images.

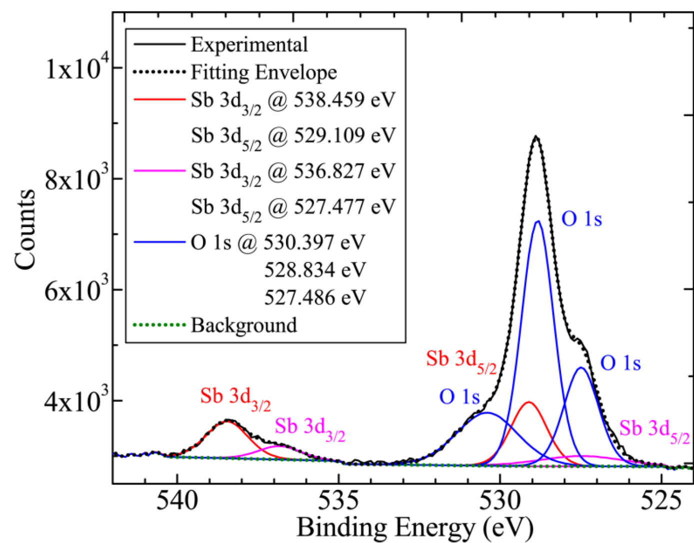


Figure 6.8 Typical XPS spectrum showing Sb-O bonding in 1.0 at.% Sb-doped ZnO films on $Al_2O_3$.

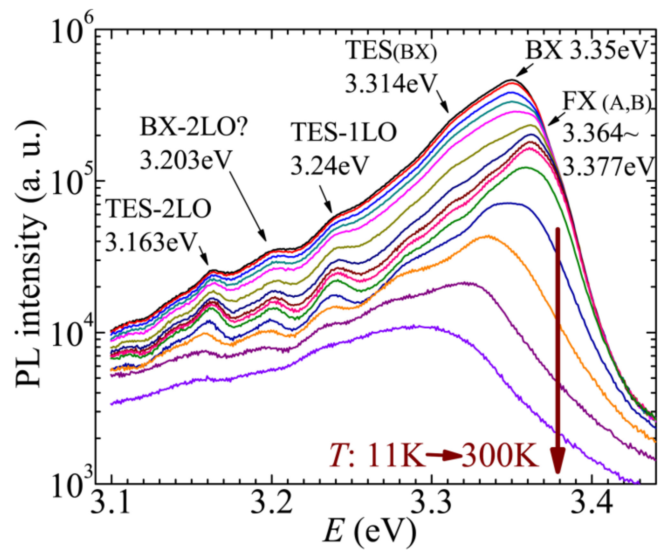


Figure 6.9 Typical temperature-dependent PL spectra of 0.1 at.% Sb-doped films grown at 600 °C on $Al_2O_3$. Spectra are displaced vertically for clarity.

# Chapter 7

# Thesis Conclusions

This thesis emphasize on synthesis, properties, strain engineering, and doping of high quality epitaxial ZnO films on Si substrates for the advantages of inexpensive large format wafers, mature device technologies, and multifunctional device integration on Si. The following conclusions have been drawn based on our experimental studies.

## 7.1 ZnO epitaxy on (111) Si using bixbyite oxide buffer layers

Single-crystalline ZnO films with superior quality were achieved on (111) Si substrates using epitaxial bixbyite oxide buffer layers ($M_2O_3$, $M$=Sc, Lu, Gd, etc.). The structural quality of the films is demonstrated by epitaxial out-of-plane and in-plane orientation relationships of $(0001)[10\bar{1}0]_{ZnO}\|(111)[\bar{1}\bar{1}2]_{M_2O_3}\|(111)[11\bar{2}]_{Si}$, small values of ZnO $\omega$-rocking curve FWHMs and tilt and twist angles, low densities of $c$-type and $a$-type dislocations, atomically smooth surface, and amorphous-free and atomically sharp interfaces.

The ZnO films exhibit intrinsic $n$-type electrical transport properties at room temperature, with resistivities of 0.2-0.3 Ω cm, electron concentrations of $2.5\text{-}3.5\times10^{17}$ $cm^{-3}$, and high Hall mobilities of 76-107 $cm^2/V$ s. The existence of a degenerate interfacial layer and two dominant hydrogenic-nature donors with thermal activation energies of 40-46 meV and 63-65 meV were recognized to affect the electrical transport. Besides mixed-type threading dislocations, intrinsic type $I_1$ stacking faults and prismatic dislocation loops are identified to be the dominant defects in the films and to correlate to the $n$-type conductivity.

The epitaxial ZnO films are of outstanding optical quality comparable to that of a ZnO single crystal. Studies on PL characteristics indicate two dominant neutral donors with optical ionization energies of 50.7 meV, and 69-73 meV. The optical ionization energies match the thermal activation energies considering the difference[199] between them. SIMS measurements imply that the two neutral donors are Ca and In impurities in the films. Due to thermally-induced planar tensile strain in the films, the PL spectra of the ZnO films redshift a couple of meV from that of the ZnO single crystal. The correlation between the tensile stress and the spectrum shift are quantified as: 1 GPa of biaxial stress results in a shift of 4.0±0.7 meV for the free exciton and 3.3±0.7 meV for donor-bound exciton transition lines, respectively.

The light emitting potential of these singlecrystalline ZnO films was demonstrated by ZnO near-band-edge and deep level emissions in EL spectra measured from prototype devices of ZnO/$M_2O_3$/$p$-Si heterostructure.

### 7.2 Strain engineering of thick, crack-free ZnO films

Thick ZnO films grown on $Gd_2O_3$/Si are strain engineered using a multi-step growth technique to further increase the cracking critical thickness to $\geq$2 μm.

Employing a LT ZnO nucleation layer provides substantial improvement of crystallinity as well as strain reduction in the film.

Insertion of periodic LT ZnO interlayers is effective in further mitigating the planar tensile strain and inceasing the cracking critical thickness but with a trade-off of crystallinity.

The major threading dislocations in the films are either mixed-type or pure edge dislocations. The defects within the LT ZnO interlayer are identified to be type $I_1$ stacking faults.

Strain engineering of thick, crack-free epitaxial ZnO films on Si is a promising step towards the development of thick-film device based on epitaxial ZnO films on Si.

### 7.3 *P*-type doping of ZnO thin films with antimony

Epitaxial and polycrystalline Sb-doped ZnO films exhibiting reliable *p*-type conductivities were achieved on (0001) $Al_2O_3$ and (100) Si substrates under high oxygen

pressure and oxygen plasma assisted growth conditions, respectively. The *p*-type conductivity of the epitaxial films results from the conjugated effects of the oxygen-rich conditions, adequate doping concentration, and dislocation-facilitated formation of complex acceptors. The thermal activation energy and the optical ionization energy of the complex acceptor are estimated 115±5 meV and 158±7 meV, respectively.

At room temperature, the epitaxial *p*-type ZnO films doped with 1.0 at.% Sb on (0001) $Al_2O_3$ have a resistivity of 4.2-60 Ω cm, a Hall mobility of 0.5-7.7 $cm^2$/V s, and a hole concentration of (1.9-2.2)×$10^{17}$ $cm^{-3}$; the polycrystalline *p*-type ZnO films doped with 0.1 at.% Sb on (100) Si have a resistivity of 44 Ω cm, a Hall mobility of 4.3 $cm^2$/V s, and a hole concentration of 3.2×$10^{16}$ $cm^{-3}$.

The epitaxial Sb-doped ZnO films grown on $Sc_2O_3$/(111) Si exhibit *n*-type conductivity possibly due to an inadequate doping amount or an increase of the formation energy of the complex acceptors induced by a lack of Zn vacancies.

### 7.4 Impact of this work

Originally employing the epitaxial bixbyite oxide buffer layers, we were able to fabricate single-crystalline ZnO films on (111) Si substrates with superior quality than all previous reports of ZnO growth on Si. These high quality films open up the possibilities of developing ZnO-based optoelectronic devices on inexpensive Si substrates, and of integrating ZnO-based multifunctional devices with Si electronics. Our systematic studies provide deep insight into the correlation between the optoelectronic properties, the defect microstructures, and the strain status of the ZnO films. Strain engineering of thick ZnO films successfully improve the cracking critical thickness to $\geq$2 μm. In addition, the key issues impeding the ZnO epitaxy on Si and the advantages of employing bixbyite oxide buffer layers were elaborated to direct the way for future research.

The experimental studies of Sb-doped ZnO films substantiates the theory of using large-size-mismatched elements for ZnO *p*-type doping, and helps to elucidate the origins of the *p*-type conductivity. This work also helps to increase the confidence of the ZnO research society to overcome the bottleneck of achieving reliable ZnO *p*-type doping for robust lighting.

# Chapter 8

# Future Work Recommendations

## 8.1 Improving NBE emissions in the heterojunction devices on Si

Although we have demonstrated in section 4.6.3 that the ZnO films grown on $M_2O_3$/(111)Si have the potential for light emitting devices, the prototype devices we constructed have apparent drawbacks. Those include weak NBE emission at 3.18 eV (390 nm), strong deep level emissions, and high device resistance, which may increase power consumptions, induce significant heating, and leads to device failure.

In order to effectively suppress the defect level emission, the physical nature of the defects in the devices, not only those in ZnO layers, must be studied and clearly understood. Based on our preliminary optical microscope studies of EL imaging of many individual ZnO/$M_2O_3$/Si devices, we have indicated that the defects that are responsible for the deep level emissions may exist in the $Gd_2O_3$ layers, at the $Gd_2O_3$/Si interfaces, or at sample edges. This suggests a future direction of defects investigation, include searching direct experimental evidence by HRTEM, corroborating with the measured electrical properties, and finding proper explanations with the Anderson model of energy-band diagrams. Imaging point defects close to atomic level by TEM is very challenging task, we hope to obtain a better understanding of the defects in ZnO-based devices in the near future, with the help of the newly-build JEOL 2100F $C_S$-corrected TEM in EMAL.

A simple method to reduce the device resistance is reducing the thickness of the $M_2O_3$ layer. Since the $M_2O_3$ layers adopted in this work is relatively thick (30-100 nm) and electrical insulating, it is difficult for hot holes to tunnel from the Si substrate through this thick barrier into the ZnO layer, and thus the efficiency of holes recombining with electrons in ZnO and generating photons is very low. In addition, electrons may travel

from the ZnO layers into the Si substrate, leading to non-radiative recombination in Si. These are the key elements limiting the NBE emission intensity from the prototype devices. We expected that after reducing the $M_2O_3$ layer thickness, the probability of holes tunneling through the $M_2O_3$ layer may increase substantially. Using conductive Si substrate should be another effective method to reduce the device resistance, increase hot carrier concentration, and reduce the power consumption and device heating. We have obtained preliminary data that, by using a conductive Si substrate (0.002 Ω cm) and an ultra thin $Sc_2O_3$ insulating layer of 1-5 nm thick, the bias voltage of the ZnO/$Sc_2O_3$/Si device can be reduced from 15-23 V (for the 30 nm $Sc_2O_3$ device) to 3-6 V at a forward current 100 mA. Thus the power consumption can be reduced 4-5 times and stronger NBE emissions are expected. However, new problems such as high leakage have caught our attentions.

In order to increase the EL intensity of the NBE emission, we must also consider the self-absorption[204] issue of ZnO. It is known that the wavelength of 390 nm corresponds to the absorption cut-off wavelength of ZnO. Thus the NBE emission from hole-electron recombination, mostly happened at the interfacial vicinity in the ZnO layer, would be re-absorbed by the top region of the ZnO layer and not detected out of the device. This obstacle can be overcome by carefully controlling the ZnO layer thickness, not to induce serious absorption, nor to decrease the crystallinity much.

Absorption of EL emissions by the Si substrate is another issue that should not be neglected. Although currently researchers do not take the Si substrate absorption into consideration, it is important to obtain detailed study and complete understanding in future.

Eventually, the EL intensity of the ZnO NBE emission from the ZnO/$M_2O_3$/Si devices can probably be enhanced if the defect level emission is suppressed, the device resistance is controlled, and the self-absorption issue is conquered.

### 8.2 Exploring high quality ZnO homojunctions grown on Si

The EL properties of the heterojunction *n*-ZnO/$M_2O_3$/(111) *p*-Si device demonstrated the lighting ability of the high quality single-crystalline ZnO films, yet the EL intensity was still low. If high quality homojunction structure of *p*-ZnO/*n*-ZnO can be

fabricated on Si substrates, the electron-hole recombination probability will be significantly enhanced, and much stronger luminescence intensities are expected. Using thicker $M_2O_3$ buffer layers (~100 nm) can block potential current leakage to the Si substrates. Controlling the thicknesses of ZnO layers should be feasible to avoid straining and cracking of the device.

The goal of achieving highly single-crystalline ZnO homojunction on Si leads us back to the major task in the research of ZnO optoelectronic applications - achieving stable *p*-type doping of epitaxial ZnO films on Si. Our work in section 6.3 indicates that 0.2 at.% Sb-doping in the ablated target is not sufficient to generate enough acceptors to compensate the native donors in the ZnO film. It is recommended to use higher Sb-doping concentration, or use other doping elements such as P in future work. Meantime, it is important to monitor the crystallinity evolution with the doping concentration.

### 8.3 Exploring different functionalities of the single-crystalline ZnO films on Si

ZnO thin films, as in the form of polycrystalline, have already been useful in many devices such as varistors, piezoelectric transducers, and TCO films, due to their excellent properties. The single-crystalline ZnO films on Si have diverse applications not only in the lighting-emitting devices, but also in UV photodetectors, transparent thin-film transistors (TTFT), and ferromagnetic applications. Most importantly, the films grown on Si have appealing advantages such as large-format production and multifunctional device integration on the same substrate.

With the high-$\kappa$ dielectric bixbyite oxide $M_2O_3$ layer incorporated, The ZnO/$M_2O_3$/Si structure is automatically a TTFT structure with $M_2O_3$ as the gate oxide (requiring conductive Si as back gate contact). The transistor properties of the ZnO/$M_2O_3$/Si structure are currently under test in our collaborating labs.

The research of ZnO thin films doped with magnetic elements such as Mn, Co… has risen rapidly in these years for potential magnetic data storage applications. So far, the doping with magnetic elements has not been explored in the single-crystalline ZnO films grown on Si, which is also a promising future direction.

# Appendix A

## High resolution XRD measurements and analyses

### A.1 Skew symmetric $\omega$-scan

Skew symmetric measurements are necessary in order to measure $\omega$-scans of the off-axis reflections (not parallel to the surface normal) in XRD, such as the reflection of $10\bar{1}2$ in (0002)-oriented ZnO.

Generally, the intersection angle $\chi$ between plane $\{hkil\}$ and plane $\{uvtw\}$ (where $i$=-$h$+$k$, $t$=-$u$+$v$) in hexagonal close-packed lattice is given by:

$$\cos(\chi) = \frac{hu + kv + \frac{1}{2}(hv + ku) + \frac{3}{4}lw\left(\frac{a_0}{c_0}\right)^2}{\sqrt{\left(h^2 + k^2 + hk + \frac{3}{4}l^2\left(\frac{a_0}{c_0}\right)^2\right)} \bullet \sqrt{\left(u^2 + v^2 + uv + \frac{3}{4}w^2\left(\frac{a_0}{c_0}\right)^2\right)}} \qquad \text{(A.1)}$$

where $a_0$ and $c_0$ are the lattice constants. For the angle between $\{hkil\}$ and (0002) in the (0002)-oriented ZnO, it can be simply determined from:

$$\tan(\chi) = \sqrt{\frac{4}{3}\frac{h^2 + k^2 + hk}{l^2}}\,\frac{c_{ZnO}}{a_{ZnO}} \qquad \text{(A.2)}$$

Here angle $\chi$ is the inclination angle of the substrate holder with respect to the X-axis, as indicated in Figure 3.5.

The standard $\theta_B$ ($\omega$), $2\theta_B$, and calculated $\chi$ angles for measuring skew symmetric $10\bar{1}2$ reflections in (0002)-oriented ZnO in this study are listed as follows:

| Reflections | sample $\omega$<br>$\theta_B$ (°) | detector $2\theta$<br>$2\theta_B$ (°) | inclination<br>$\chi$ (°) |
|---|---|---|---|
| ZnO $10\bar{1}2$ | 23.77 | 47.54 | 42.77 |

Note: On the BEDE instrument, a minus sign should be added to $\chi$ when inclining the sample holder.

Since the planes $\{10\bar{1}2\}$ in (0002)-oriented ZnO epilayer have six-fold symmetry with respect to the *c*-axis, as shown in Figure 3.6(b), the Bragg condition can not be satisfied unless the inclined sample is rotated an azimuthal angle $\phi_0$ to allow the $(10\bar{1}2)$ plane be parallel to the original sample surface. In the following, we summarize the procedure of using the BEDE diffractometer to run a skew symmetric $\omega$-scan in (0002)-oriented ZnO:

1. Set $\omega$ and $2\theta$ angles to the Bragg angles of the measured reflection $10\bar{1}2$.

2. Set the inclination angle $\chi$ to the intersection angle between (0002) and $(10\bar{1}2)$.

3. Slowly rotate the sample surrounding the $[10\bar{1}2]$ axis until the detector picks up high intensity above the noise level, stop. The rotated angle is $\phi_0$. The precise angle can be found by maximizing the detector intensity during a $\phi_0$ rocking-curve scan. Due to the six-fold symmetry, one of the six $\phi_0$ should be easily found within -30°~30°.

4. Optimize $\omega$, $\chi$, and $\phi_0$ one after another by maximizing the detector intensity when rocking one angle and fixing others.

5. Fix $\chi$ and $\phi_0$ and perform the $\omega$-scan.

### A.2 $\phi$-scan in the glancing incidence geometry

The ZnO $11\bar{2}4$ reflection, $Al_2O_3$ $11\bar{2}9$ reflection, and Si 440 reflection were selected to perform the 0°-360° $\phi$-scans to determine the orientation relationships in this study:

| Reflections | sample $\omega$<br>$\theta_B$- $\chi_0$ (°) | detector $2\theta$<br>$2\theta_B$ (°) | inclination<br>$\chi$ (°) |
|---|---|---|---|
| ZnO $11\bar{2}4$ | 10.61 | 98.61 | 0.0 |
| $Al_2O_3$ $11\bar{2}9$ | 7.35 | 77.23 | 0.0 |
| Si 440 | 18.10 | 106.72 | 0.0 |

### A.3 Determination of the twist angle

The FWHM values of symmetric reflection 0002 and skew symmetric reflections $10\bar{1}l$ ($l$=1-5) were measured to estimate the twist angle of the ZnO film. The skew symmetric measurements were performed according to the procedure of A.1.

| ZnO<br>Reflections | sample $\omega$<br>$\theta_B$ (°) | detector $2\theta$<br>$2\theta_B$ (°) | inclination<br>$\chi$ (°) |
|---|---|---|---|
| 0002 | 17.21 | 34.42 | 0.0 |
| $10\bar{1}5$ | 52.07 | 104.13 | 20.30 |
| $10\bar{1}4$ | 40.68 | 81.37 | 24.82 |
| $10\bar{1}3$ | 31.43 | 62.86 | 31.66 |
| $10\bar{1}2$ | 23.77 | 47.54 | 42.77 |
| $10\bar{1}1$ | 18.13 | 36.25 | 61.84 |

Note: On the BEDE instrument, a minus sign should be added to $\chi$ when operating inclination of the sample holder.

The plot of FWHM values of 0002 and $10\bar{1}l$ reflections vs. $\chi$ angles were fitted by inter-dependent Srikant analysis[142] using the following MATLAB code:

```
% Pseudo-Voigt simulation using inter-dependent Srikant method.
function y=omega(x,omega_z,omega_y,m)
% y is omega(resultant), x is Chi.
  omega_0_tilt=acos(cos(x).^2*cos(omega_y*pi/180)+sin(x).^2);
```

```
  omega_0_twist=acos(sin(x).^2*cos(omega_z*pi/180)+cos(x).^2);
  omega_eff_tilt=omega_0_tilt.*exp(-m*omega_0_twist/(omega_z*pi/180));
  omega_eff_twist=omega_0_twist.*exp(-m*omega_0_tilt/(omega_y*pi/180));
  n=1.25;
  y=(omega_eff_tilt.^n+omega_eff_twist.^n).^(1/n);
end

% Find twist angle from Pseudo-Voigt simulation of off-axis FWHMs.
for omega_z=0.01:0.02:1
  % Test twist angle (omega_z) from 0 to 1 degree for a best fitting.
  omega_y=0.09;   %Set omega_y to the FWHM value of 0002 reflection.
  m=0.1;          % Choose m between 0-1 for best fitting.
  x0=[0.,20.30,24.82,31.66,42.77,62.32]*pi/180; % x0 are Chi angles.
  y0=[0.09,0.231,0.264,0.296,0.364,0.434];
  % Set y0 the FWHMs of reflections of 002,105,104,103,102,101.
  x=[0:1:90]*pi/180;  %Chi is tested from 0 to 90 degrees.
  y=omega(x,omega_z,omega_y,m)*180/pi;  %Use the omega function.
  plot(x*180/pi,y,x0*180/pi,y0,'o');
  axis([0,90,0.01,0.5]);
  omega_z;   % Output tested omega_z, stop when fitting is best.
  omega0=omega(pi/2,omega_z,omega_y,m)*180/pi;
  pause; end
```

# Appendix B

# Temperature-dependent Hall effect fittings

## B.1 Three-band CBE simulation of *n*(*T*)

Plotting: $n(T)$ vs. $1/k_BT$.

Fitting parameters: $N_{D1}$, $N_{D2}$, $N_{D3}$, $E_{D1}$, $E_{D2}$, $E_{D3}$, and $N_A$.

MATLAB code:

```
function [n1,invT1,A]=n_mu(x,y)
% x and y are arrays of experimental data of 1/kBT and n
% Simulate temperature dependent electron concentration for n-type ZnO
Na=2e15;    % Acceptor concentration in cm-3, fitting parameter
Nd1=3.3e17; % Donor concentration in cm-3, fitting parameter
Ed1=0.065;  % Donor energy in eV, fitting parameter
gd1=1/2;    % Degeneracy factor for donor 2
Nd2=2e17;   % Donor 2 concentration in cm-3, fitting parameter
Ed2=0.042;  % Donor 2 energy in eV, fitting parameter
gd2=1/2;    % Degeneracy factor for donor 2
Nd3=1.4e17; % Donor 3 concentration in cm-3, fitting parameter
Ed3=0.001;  % Donor 3 energy in eV, fitting parameter
gd3=1/2;    % Degeneracy factor for donor 3
Ncprime=8.66e14; % Effective density of states at 1 K in cm-3
k=8.617e-5;      % Boltzmann constant in eV/K
tstart=10;       % start temperature in K
tend=300;        % end temperature in K
tpts=200;        % number of points for temperature simulation
nstart=10;       % exponent for start of sweep
                 % to solve transcendental equation
nfinish=19;      % exponent for end of sweep
npts=800;        % number of points
T=linspace(tstart,tend,tpts);
ntemp=logspace(nstart,nfinish,npts);
for i=1:tpts
    phid1(i)=gd1*Ncprime*T(i)^1.5*exp(-Ed1/k/T(i));
    phid2(i)=gd2*Ncprime*T(i)^1.5*exp(-Ed2/k/T(i));
    phid3(i)=gd3*Ncprime*T(i)^1.5*exp(-Ed3/k/T(i));
    pd1=phid1(i);
    pd2=phid2(i);
    pd3=phid3(i);
    temp=1e20;
```

```
    tempindex=0;
    for j=1:npts   % solve transcendental equation for n
        ls(j)=ntemp(j)+Na;
  rs(j)=Nd1/(1+ntemp(j)/pd1)+Nd2/(1+ntemp(j)/pd2)+Nd3/(1+ntemp(j)/pd3);
        if abs(ls(j)-rs(j))<temp
            temp=abs(ls(j)-rs(j));
            tempindex=j;
        end
    end
    n(i)=ntemp(tempindex);
    invT(i)=1/k/T(i);
end
figure(1)
semilogy(invT,n,x,y,'.')
axis([0,400,1e16,1e18]);
n1=n';
invT1=invT';
A=Na;
```

## B.2 Matthiessen's rule simulation of $\mu(T)$

Plotting: $\mu(T)$ and all five components vs. $T$.

Fitting parameters: $N_A$, $N_{dis}$, $\theta_D$.

MATLAB code:

```
function [T,mu,mu1,mu2,mu3,mu4,mu5]=mobility(x,y,x1,y1)
% x and y are arrays of experimental data of 1/kBT and n
% x1 and y1 are arrays of experimental data of T and mu
% Simulate temperature dependent mobility(mu) for n-type ZnO
m0=9.11e-31;   % Free electron mass in kg
me=0.318*m0;   % Electron effective mass of ZnO
h=1.055e-34;   % Plank (Dirac) constant in Js
k=1.38e-23;    % Boltzmann constant in m2 kg s-2 K-1
e=1.6e-19;     % Elementary charge in C
E1=15*e;       % Deformation potential in J
rho=6100;      % Mass density of ZnO in kg/m3
s=6.59e3;      % Sound speed in ZnO in m/s
e0=8.84e-12;   % Vacuum permittivity in C2/Jm
es=8.12;       % Relative static dielectric constant of ZnO
ei=3.72;       % Relative infinite dielectric constant of ZnO
cZnO=5.25e-10; % Lattice constant of ZnO in m
theta_D=920;   % Debye temperature of ZnO in K, fitting parameter
Ndis=2.e9*1e4; % Dislocation density in m-2, fitting parameter
c1=me*e*k*theta/e0/h/h*((1/ei)-(1/es));
               % Constant E0 in polar optical phonon scattering
c2=e*(h^4)*rho*(s^2)/3/E1/E1*sqrt(8*pi/(me^5)/(k^3));
               % Constant in deformation potential scattering
c3=4/3/c1*sqrt(2*k/pi/me);      %Constant in Polar phonon scattering
b1=24*me*es*e0*(k^2)/((e*h)^2); %Constant-1 in b in impurity scattering
c4=128*sqrt(2*pi/me)*((e0*es)^2)*(k^1.5)/(e^3);
                                 %Constant-2 in impurity scattering
b2=8*e0*es*me*(k^2)/e/e/h/h;     %Constant-1 in dislocation scattering
c5=(h^3)*e*((cZnO/me/k)^2)/Ndis; %Constant-2 in dislocation scattering
[n2,invT1,A]=n_mu(x,y); % Input CBE simulated n, invT, and Na
```

```
Na=A*1e6;       % Acceptor concentration in m-3, can also be a fitting
                % parameter here and return to n_mu for better n fitting
tstart=10;      % Start temperature in K
tend=300;       % End temperature in K
tpts=200;       % Number of points for temperature simulation
T=linspace(tstart,tend,tpts);
for i=1:tpts
n1(i)=n2(i)*1e6;  % Use carrier concentration in m-3
mu1(i)=160/(0.318^1.5)*sqrt(300/T(i));
                   % (1)Piezoelectric scattering in cm2/Vs
mu2(i)=1e4*c2/(T(i)^1.5); % (2)Deformation potential scattering
                           % also acoustic phonon scattering in cm2/Vs
z(i)=theta_D/T(i);
mu3(i)=1e4*c3*(T(i)^0.5)*(exp(z(i)-1));
                           % (3)Polar optical phonon scattering
b(i)=b1*(T(i)^2)/n1(i);
mu4(i)=1e4*c4/(2*Na+n1(i))*(T(i)^1.5)/(log(1+b(i))-(b(i)/(1+b(i))));
                           % (4)Ionized impurity scattering
mu5(i)=1e4*c5*((n1(i)/T(i))^2)*((1+(b2*(T(i)^2)/n1(i)))^1.5);
                           % (5)Dislocation scattering
mu(i)=1/(1/mu1(i)+1/mu2(i)+1/mu3(i)+1/mu4(i)+1/mu5(i));
                           % total mobility
end
semilogy (T,mu,'.',T,mu1,T,mu2,T,mu3,T,mu4,T,mu5,x1,y1,'o')
axis([10,300,10,1e6]);
legend   ('Total   mobility','Piezoelectric','Acoustic   phonon','Polar
optical phonon','Ionized impurity','Dislocation')
xlabel('Temperature(K)')
ylabel('mobility (cm^2/V.s)')
title ('Electron mobility vs Temperature in ZnO')
T=T';
mu=mu';
mu1=mu1';
mu2=mu2';
mu3=mu3';
mu4=mu4';
mu5=mu5';
%figure
%plot(T,mu,x1,y1,'-o');
%xlabel('Temperature(K)')
%ylabel('mobility (cm^2/V.s)')
%title ('Electron mobility vs Temperature in ZnO')
%grid;
```

# Bibliography


[1] W. W. Wenas, A. Yamada, K. Takahashi, M. Yoshino, and M. Konagai, J. Appl. Phys. **70**, 7119 (1991).

[2] Y. Ito, K. Kushida, K. Sugawara, and H. Takeuchi, IEEE Trans. Ultrason. Ferroelectr. Freq. Control **42**, 316 (1995).

[3] J. Wong, J. Appl. Phys. **51**, 4453 (1980).

[4] J. M. Hammer, D. J. Channin, M. T. Duffy, and C. C. Neil, IEEE J. Quantum Electron. **QE11**, 138 (1975).

[5] Q. Wan, Q. H. Li, Y. J. Chen, T. H. Wang, X. L. He, J. P. Li, and C. L. Lin, Appl. Phys. Lett. **84**, 3654 (2004).

[6] A. Tsukazaki, A. Ohtomo, T. Onuma, M. Ohtani, T. Makino, M. Sumiya, K. Ohtani, S. F. Chichibu, S. Fuke, Y. Segawa, H. Ohno, H. Koinuma, and M. Kawasaki, Nat. Mater. **4**, 42 (2005).

[7] D. M. Bagnall, Y. F. Chen, Z. Zhu, T. Yao, S. Koyama, M. Y. Shen, and T. Goto, Appl. Phys. Lett. **70**, 2230 (1997).

[8] D. C. Look, D. C. Reynolds, J. R. Sizelove, R. L. Jones, C. W. Litton, G. Cantwell, and W. C. Harsch, Solid State Commun. **105**, 399 (1998).

[9] J. D. Albrecht, P. P. Ruden, S. Limpijumnong, W. R. L. Lambrecht, and K. F. Brennan, J. Appl. Phys. **86**, 6864 (1999).

[10] D. C. Look, D. C. Reynolds, J. W. Hemsky, R. L. Jones, and J. R. Sizelove, Appl. Phys. Lett. **75**, 811 (1999).

[11] R. D. Vispute, V. Talyansky, S. Choopun, R. P. Sharma, T. Venkatesan, M. He, X. Tang, J. B. Halpern, M. G. Spencer, Y. X. Li, L. G. Salamanca-Riba, A. A. Iliadis, and K. A. Jones, Appl. Phys. Lett. **73**, 348 (1998).

[12] T. Matsuoka, N. Yoshimoto, T. Sasaki, and A. Katsui, J. Electron. Mater. **21**, 157 (1992).

[13] A. Ohtomo, K. Tamura, K. Saikusa, K. Takahashi, T. Makino, Y. Segawa, H. Koinuma, and M. Kawasaki, Appl. Phys. Lett. **75**, 2635 (1999).

[14] A. B. M. A. Ashrafi, N. T. Binh, B. P. Zhang, and Y. Segawa, Appl. Phys. Lett. **84**, 2814 (2004).

[15] M. M. C. Chou, L. W. Chang, H. Y. Chung, T. H. Huang, J. J. Wu, and C. W. Chen, J. Cryst. Growth **308**, 412 (2007).

[16] Y. C. Chao, C. W. Lin, D. J. Ke, Y. H. Wu, H. G. Chen, L. Chang, Y. T. Ho, and M. H. Liang, J. Cryst. Growth **298**, 461 (2007).

[17] T. Matsumoto, K. Nishimura, Y. Nabetani, and T. Kato, Phys. Status Solidi B **241**, 591 (2003).

[18] Y. F. Chen, H. J. Ko, S. K. Hong, T. Yao, and Y. Segawa, J. Cryst. Growth **214/215**, 87 (2000).

[19] K. Wasa, T. Hada, and S. Hayakawa, Jpn. J. Appl. Phys. **10**, 1732 (1971).

[20] K. J. Hubbard and D. G. Schlom, J. Mater. Res. **11**, 2757 (1996).

[21] A. Ashrafi and C. Jagadish, J. Appl. Phys. **102**, 071101 (2007).

[22] H. Karzel, W. Potzel, M. Kofferlein, W. Schiessl, M. Steiner, U. Hiller, G. M. Kalvius, D. W. Mitchell, T. P. Das, P. Blaha, K. Schwarz, and M. P. Pasternak, Phys. Rev. B **53**, 11425 (1996).

[23] C. F. Klingshirn, *Semiconductor Optics*. (Springer-Verlag Berlin Heidelberg, Berlin, 2007), 252.

[24] F. T. J. Smith, Appl. Phys. Lett. **43**, 1108 (1983).

[25] Th. Kaufmann, G. Fuchs, and M. Webert, Cryst. Res. Technol. **23**, 635 (1988).

[26] Y. J. Kim and H. J. Kim, Mater. Lett. **21**, 351 (1994).

[27] Z. C. Zhang, B. B. Huang, Y. Q. Yu, and D. L. Cui, Mater. Sci. Eng. B-Solid State Mater. Adv. Technol. **86**, 109 (2001).

[28] B. S. Li, Y. C. Liu, D. Z. Shen, Y. M. Lu, J. Y. Zhang, X. G. Kong, X. W. Fan, and Z. Z. Zhi, J. Vac. Sci. Technol. A-Vac. Surf. Films **20**, 265 (2002).

[29] B. S. Li, Y. C. Liu, D. Z. Shen, J. Y. Zhang, Y. M. Lu, and X. W. Fan, J. Cryst. Growth **249**, 179 (2003).

[30] Z. Z. Zhi, Y. C. Liu, B. S. Li, X. T. Zhang, Y. M. Lu, D. Z. Shen, and X. W. Fan, J. Phys. D: Appl. Phys. **36**, 719 (2003).

[31] Y. T. Zhang, G. T. Du, X. Q. Wang, W. C. Li, X. T. Yang, Y. Ma, B. J. Zhao, H. J. Yang, D. L. Liu, and S. R. Yang, J. Cryst. Growth **252**, 180 (2003).

[32] B. H. Kong, S. K. Mohanta, D. C. Kim, and H. K. Cho, Physica B **401**, 399 (2007).

[33] X. P. Li, B. L. Zhang, H. C. Zhu, X. Dong, X. C. Xia, Y. G. Cui, K. Huang, and G. T. Du, Appl. Surf. Sci. **254**, 2081 (2008).

[34] X. P. Li, B. L. Zhang, H. C. Zhu, X. Dong, X. C. Xia, Y. G. Cui, Y. Ma, and G. T. Du, J. Phys. D-Appl. Phys. **41**, 35101 (2008).

[35] V. Khranovskyy, A. Ulyashin, G. Lashkarev, B. G. Svensson, and R. Yakimova, Thin Solid Films **516**, 1396 (2008).

[36] V. Khranovskyy, G. R. Yazdi, G. Lashkarev, A. Ulyashin, and R. Yakimova, Phys. Status Solidi A **205**, 144 (2008).

[37] S. T. Tan, X. W. Sun, J. L. Zhao, S. Iwan, Z. H. Cen, T. P. Chen, J. D. Ye, G. Q. Lo, D. L. Kwong, and K. L. Teo, Appl. Phys. Lett. **93**, 13506 (2008).

[38] V. Craciun, J. Elders, J. G. E. Gardeniers, and W. Boyd Ian, Appl. Phys. Lett. **65**, 2963 (1994).

[39] M. Joseph, H. Tabata, and T. Kawai, Appl. Phys. Lett. **74**, 2534 (1999).

[40] J. H. Choi, H. Tabata, and T. Kawai, J. Cryst. Growth **226**, 493 (2001).

[41] Y. B. Zhang, Q. Liu, T. Sritharan, C. L. Gan, and S. Li, Appl. Phys. Lett. **89**, 042510 (2006).

[42] L. Han, F. Mei, C. Liu, C. Pedro, and E. Alves, Physica E **40**, 699 (2008).

[43] Y. F. Yang, H. Long, G. Yang, N. L. Dai, Q. G. Zheng, and P. X. Lu, J. Cryst. Growth **310**, 551 (2008).

[44] S. Harako, S. Yokoyama, K. Ide, X. Zhao, and S. Komoro, Phys. Status Solidi A **205**, 19 (2008).

[45] S. Masuda, K. Kitamura, Y. Okumura, S. Miyatake, H. Tabata, and T. Kawai, J. Appl. Phys. **93**, 1624 (2003).

[46] R. S. Ajimsha, M. K. Jayaraj, and L. M. Kukreja, J. Electron. Mater. **37**, 770 (2008).

[47] F. C. M. Vandepol, F. R. Blom, and T. J. A. Popma, Thin Solid Films **204**, 349 (1991).

[48] Y. T. Zhang, G. T. Du, D. L. Liu, X. Q. Wang, Y. Ma, J. Z. Wang, J. Z. Yin, X. T. Yang, X. K. Hou, and S. R. Yang, J. Cryst. Growth **243**, 439 (2002).

[49] S. Y. Chu, W. Water, and J. T. Liaw, J. Euro. Cer. Soc. **23**, 1593 (2003).

[50] P. F. Carcia, R. S. McLean, M. H. Reilly, and G. Nunes, Appl. Phys. Lett. **82**, 1117 (2003).

[51] S. H. Jeong, B. S. Kim, and B. T. Lee, Appl. Phys. Lett. **82**, 2625 (2003).

[52] S. H. Jeong, J. K. Kim, and B. T. Lee, J. Phys. D: Appl. Phys. **36**, 2017 (2003).

[53] J. W. Shin, J. Y. Lee, Y. S. No, T. W. Kim, and W. K. Choi, Appl. Phys. Lett. **89**, 101904 (2006).

[54] Z. W. Liu, C. W. Sun, J. F. Gu, and Q. Y. Zhang, Appl. Phys. Lett. **88**, 251911 (2006).

[55] S. Kim, D. K. Lee, S. H. Hong, S. H. Eom, H. T. Oh, S. H. Choi, H. N. Hwang, and C. C. Hwang, J. Appl. Phys. **103**, 023514 (2008).

[56] D. Y. Song and B. Z. Guo, J. Phys. D-Appl. Phys. **42**, 25103 (2009).

[57] P. L. Chen, X. Y. Ma, and D. R. Yang, Appl. Phys. Lett. **89**, 111112 (2006).

[58] P. L. Chen, X. Y. Ma, D. S. Li, Y. Y. Zhang, and D. R. Yang, Appl. Phys. Lett. **90**, 251115 (2007).

[59] X. Y. Ma, P. L. Chen, D. S. Li, Y. Y. Zhang, and D. R. Yang, Appl. Phys. Lett. **91**, 251109 (2007).

[60] P. L. Chen, X. Y. Ma, and D. R. Yang, J. Appl. Phys. **101**, 53103 (2007).

[61] H. Z. Wu, K. M. He, D. J. Qiu, and D. M. Huang, J. Cryst. Growth **217**, 131 (2000).

[62] L. J. Mandalapu, F. X. Xiu, Z. Yang, D. T. Zhao, and J. L. Liu, Appl. Phys. Lett. **88**, 112108 (2006).

[63] J. M. Yuk, J. Y. Lee, J. H. Jung, T. W. Kim, D. I. Son, and W. K. Choi, Appl. Phys. Lett. **90**, 31907 (2007).

[64] X. D. Chen, C. C. Ling, S. Fung, C. D. Beling, Y. F. Mei, R. K. Y. Fu, G. G. Siu, and P. K. Chu, Appl. Phys. Lett. **88**, 132104 (2006).

[65] Y. Z. Yoo, Y. Osaka, T. Fukumura, Z. Jin, M. Kawasaki, H. Koinuma, T. Chikyow, P. Ahmet, A. Setoguchi, and S. F. Chichibu, Appl. Phys. Lett. **78**, 616 (2001).

[66] P. L. Chen, X. Y. Ma, D. S. Li, Y. Y. Zhang, and D. R. Yang, Appl. Phys. Lett. **94**, 61110 (2009).

[67] J. L. Zhao, X. W. Sun, S. T. Tan, G. Q. Lo, D. L. Kwong, and Z. H. Cen, Appl. Phys. Lett. **91**, 263501 (2007).

[68] H. D. Li, S. F. Yu, A. P. Abiyasa, C. Yuen, S. P. Lau, H. Y. Yang, and E. S. P. Leong, Appl. Phys. Lett. **86**, 261111 (2005).

[69] Y. Ohya, T. Niwa, T. Ban, and Y. Takahashi, Jpn. J. Appl. Phys. **40**, 297 (2001).

[70] Y. Z. Yoo, T. Sekiguchi, T. Chikyow, M. Kawasaki, T. Onuma, S. F. Chichibu, J. H. Song, and H. Koinuma, Appl. Phys. Lett. **84**, 502 (2004).

[71] X. M. Fan, J. S. Lian, Z. X. Guo, and H. J. Lu, Appl. Surf. Sci. **239**, 176 (2005).

[72] A. Miyake, H. Kominami, H. Tatsuoka, H. Kuwabara, Y. Nakanishi, and Y. Hatanaka, Jpn. J. Appl. Phys. **39**, L1186 (2000).

[73] L. Wang, Y. C. Liu, C. S. Xu, Y. Q. Qiu, L. Zhao, and X. M. Rong, J. Phys. D-Appl. Phys. **42**, 35307 (2009).

[74] J. Zhao, L. Z. Hu, W. F. Liu, and Z. Y. Wang, Appl. Surf. Sci. **253**, 6255 (2007).

[75] J. Ye, S. Gu, S. Zhu, T. Chen, W. Liu, F. Qin, L. Hu, R. Zhang, Y. Shi, and Y. Zheng, J. Vac. Sci. Technol. A **21**, 979 (2003).

[76] P. Wang, N. F. Chen, and Z. G. Yin, Appl. Phys. Lett. **88**, 152102 (2006).

[77] H. W. Liang, Q. J. Feng, J. C. Sun, J. Z. Zhao, J. M. Bian, L. Z. Hu, H. Q. Zhang, Y. M. Luo, and G. T. Du, Semicond. Sci. Technol. **23**, 25014 (2008).

[78] Z. X. Fu, B. X. Lin, G. H. Liao, and Z. Q. Wu, J. Cryst. Growth **193**, 316 (1998).

[79] B. X. Lin, Z. X. Fu, and Y. B. Jia, Appl. Phys. Lett. **79**, 943 (2001).

[80] F. X. Xiu, Z. Yang, D. T. Zhao, J. L. Liu, K. A. Alim, A. A. Balandin, M. E. Itkis, and R. C. Haddon, J. Cryst. Growth **286**, 61 (2006).

[81] W. Zheng, Y. Liao, L. Li, Q. X. Yu, G. Z. Wang, Y. P. Li, and Z. X. Fu, Appl. Surf. Sci. **253**, 2765 (2006).

[82] L. J. Mandalapu, Z. Yang, S. Chu, and J. L. Liu, Appl. Phys. Lett. **92**, 122101 (2008).

[83] J. Y. Huang, Z. Z. Ye, H. M. Lu, L. Wang, B. H. Zhao, and X. H. Li, J. Phys. D-Appl. Phys. **40**, 4882 (2007).

[84] E. Kasper, K. Lyutovich, M. Bauer, and M. Oehme, Thin Solid Films **336**, 319 (1998).

[85] S. P. Chang, S. J. Chang, Y. Z. Chiou, C. Y. Lu, T. K. Lin, C. F. Kuo, H. M. Chang, and U. H. Liaw, J. Cryst. Growth **310**, 290 (2008).

[86] X. Z. Cui, T. C. Zhang, Z. X. Mei, Z. L. Liu, Y. P. Liu, Y. Guo, Q. K. Xue, and X. L. Du, J. Cryst. Growth **310**, 5428 (2008).

[87] J. Y. Kong, S. Chu, M. Olmedo, L. Li, Z. Yang, and J. L. Liu, Appl. Phys. Lett. **93**, 132113 (2008).

[88] S. Chu, M. Olmedo, Z. Yang, J. Y. Kong, and J. L. Liu, Appl. Phys. Lett. **93**, 181106 (2008).

[89] J. Narayan, A. K. Sharma, A. Kvit, C. Jin, J. F. Muth, and O. W. Holland, Solid State Commun. **121**, 9 (2002).

[90] E. R. Segnit and A. E. Holland, J. Am. Ceram. Soc. **48**, 409 (1965).

[91] M. Fujita, N. Kawamoto, T. Tatsumi, K. Yamagishi, and Y. Horikoshi, Jpn. J. Appl. Phys. **42**, 67 (2003).

[92] A. Tiwari, M. Park, C. Jin, H. Wang, D. Kumar, and J. Narayan, J. Mater. Res. **17**, 2480 (2002).

[93] A. Nahhas, H. K. Kim, and J. Blachere, Appl. Phys. Lett. **78**, 1511 (2001).

[94] N. Oleynik, A. Dadgar, J. Blasing, M. Adam, A. Krtschil, D. Forster, F. Bertram, A. Diez, M. Seip, A. Greiling, J. Christen, and A. Krost, Jpn. J. Appl. Phys. **42**, 7474 (2003).

[95] M. Kumar, R. M. Mehra, A. Wakahara, M. Ishida, and A. Yoshida, J. Appl. Phys. **93**, 3837 (2003).

[96] A. Miyake, H. Kominami, H. Tatsuoka, H. Kuwabara, Y. Nakanishi, and Y. Hatanaka, J. Cryst. Growth **214/215**, 294 (2000).

[97] T. Onuma, S. F. Chichibu, A. Uedono, Y. Z. Yoo, T. Chikyow, T. Sota, M. Kawasaki, and H. Koinuma, Appl. Phys. Lett. **85**, 5586 (2004).

[98] K. Iwata, P. Fons, S. Niki, A. Yamada, K. Matsubara, K. Nakahara, T. Tanabe, and H. Takasu, J. Cryst. Growth **214**, 50 (2000).

[99] K. Haga, T. Suzuki, Y. Kashiwaba, H. Watanabe, B. P. Zhang, and Y. Segawa, Thin Solid Films **433**, 131 (2003).

[100] S. H. Jeong, S. I. Kim, J. K. Kim, and B. T. Lee, J. Cryst. Growth **264**, 327 (2004).

[101] D. Y. Lee, C. H. Choi, and S. H. Kim, J. Cryst. Growth **268**, 184 (2004).

[102] J. F. Yan, Y. M. Lu, Y. C. Liu, and H. W. Liang, J. Cryst. Growth **266**, 505 (2004).

[103] J. F. Yan, Y. M. Lu, H. W. Liang, Y. C. Liu, B. H. Li, X. W. Fan, and J. M. Zhou, J. Cryst. Growth **280**, 206 (2005).

[104] J. Zhao, L. Z. Hu, Z. Y. Wang, Z. J. Wang, H. Q. Zhang, Y. Zhao, and X. P. Liang, J. Cryst. Growth **280**, 455 (2005).

[105] C. C. Lin, S. Y. Chen, S. Y. Cheng, and H. Y. Lee, Appl. Phys. Lett. **84**, 5040 (2004).

[106] J. J. Zhu, B. X. Lin, X. K. Sun, R. Yao, C. S. Shi, and Z. X. Fu, Thin Solid Films **478**, 218 (2005).

[107] Y. Zhang, H. W. Zheng, J. F. Su, B. X. Lin, and Z. X. Fu, J. Lumines. **124**, 252 (2007).

[108] W. Guo, A. Allenic, Y. B. Chen, X. Q. Pan, W. Tian, C. Adamo, and D. G. Schlom, Appl. Phys. Lett. **92**, 072101 (2008).

[109] W. Guo, M. B. Katz, C. T. Nelson, T. Heeg, D. G. Schlom, B. Liu, Y. Che, and X. Q. Pan, Appl. Phys. Lett. **94**, 122107 (2009).

[110] W. Guo, Y. Zhang, C. T. Nelson, M. B. Katz, T. Heeg, D. G. Schlom, B. Liu, Y. Che, and X. Q. Pan, (unpublished, 2009).

[111] W. R. Liu, Y. H. Li, W. F. Hsieh, C. H. Hsu, W. C. Lee, Y. J. Lee, M. Hong, and J. Kwo, Cryst. Growth Des. **9**, 239 (2009).

[112] N. Kawamoto, M. Fujita, T. Tatsumi, and Y. Horikoshi, Jpn. J. Appl. Phys. **42**, 7209 (2003).

[113] Y. F. Chen, F. Y. Jiang, L. Wang, C. D. Zheng, J. N. Dai, Y. Pu, and W. Q. Fang, J. Cryst. Growth **275**, 486 (2005).

[114] L. Wang, Y. Pu, Y. F. Chen, C. L. Mo, W. Q. Fang, C. B. Xiong, J. N. Dai, and F. Y. Jiang, J. Cryst. Growth **284**, 459 (2005).

[115] F. Y. Jiang, C. D. Zheng, L. Wang, W. Q. Fang, Y. Pu, and H. N. Dai, J. Lumin. **122-123**, 905 (2007).

[116] X. N. Wang, Y. Wang, Z. X. Mei, J. Dong, Z. Q. Zeng, H. T. Yuan, T. C. Zhang, X. L. Du, J. F. Jia, Q. K. Xue, X. N. Zhang, Z. Zhang, Z. F. Li, and W. Lu, Appl. Phys. Lett. **90**, 151912 (2007).

[117] X. W. Sun, J. L. Zhao, S. T. Tan, L. H. Tan, C. H. Tung, G. Q. Lo, D. L. Kwong, Y. W. Zhang, X. M. Li, and K. L. Teo, Appl. Phys. Lett. **92**, 111113 (2008).

[118] Y. W. Zhang, X. M. Li, W. D. Yu, X. D. Gao, Y. F. Gu, C. Yang, J. L. Zhao, X. W. Sun, S. T. Tan, J. F. Kong, and W. Z. Shen, J. Phys. D-Appl. Phys. **41**, 205105 (2008).

[119] R. A. Robie and B. S. Hemingway, U.S. Geol. Survey Bull. **2131**, 17, 18 (1995).

[120] A. Usui, H. Sunakawa, A. Sakai, and A. A. Yamaguchi, Jpn. J. Appl. Phys. **36**, L899 (1997).

[121] A. Dadgar, J. Blasing, A. Diez, A. Alam, M. Heuken, and A. Krost, Jpn. J. Appl. Phys. **39**, L1183 (2000).

[122] C. W. Ong, D. G. Zong, M. Aravind, C. L. Choy, and D. R. Lu, J. Mater. Res. **18**, 2464 (2003).

[123] A. Krost, A. Dadgar, G. Strassburger, and R. Clos, Phys. Status Solidi A **200**, 26 (2003).

[124] Y. Okada and Y. Tokumaru, J. Appl. Phys. **56**, 314 (1984).

[125] W. Qian, M. Skowronski, and G. R. Rohrer, Mater. Res. Soc. Symp. Proc. **423**, 475 (1996).

[126] S. Stecura and W. J. Campbell, U. S. Bur. Mines. Rep. Invest. **5847**, 14, 32, 40 & 43 (1961).

[127] H. P. Maruska and J. J. Tietjen, Appl. Phys. Lett. **15**, 327 (1969).

[128] J. Albertsson, S. C. Abrahams, and A. Kvick, Acta Crystallogr., Sect. B: Struct. Sci. **45**, 34 (1989).

[129] S. Q. Wang, Appl. Phys. Lett. **88**, 61902 (2006).

[130] W. Y. Ching, L. Z. Ouyang, P. Rulis, and H. Z. Yao, Phys. Rev. B **78**, 14106 (2008).

[131] J. S. Browder and S. S. Ballard, Appl. Optics **8**, 793 (1969).

[132] H. Karl and B. Stritzker, Phys. Rev. Lett. **69**, 2939 (1992).

[133] D. Lubben, S. A. Barnett, K. Suzuki, S. Gorbatkin, and J. E. Greene, J. Vac. Sci. Technol. B **3**, 968 (1985).

[134] C. M. Cotell and K. S. Grabowski, MRS Bull. **17**, 44 (1992).

[135] D. B. Chrisey and G. K. Hubler, *Pulsed Laser Deposition of Thin Films*. (J. Wiley, New York, 1994), §4.3 & §7.4

[136] R. K. Singh and J. Narayan, Phys. Rev. B **41**, 8843 (1990).

[137] T. P. Hughes and Nicholso.Mb, J. Phys. A **1**, 588 (1968).

[138] A. Kar and J. Mazumder, Phys. Rev. E **49**, 410 (1994).

[139] *Landolt-Börnstein - Group III Condensed Matter* (Springer-Verlag, 1999), Vol. 41B, pp. 1-12.

[140] G. K. Williamson and W. H. Hall, Acta Metall. **1**, 22 (1953).

[141] T. Metzger, R. Hopler, E. Born, O. Ambacher, M. Stutzmann, R. Stommer, M. Schuster, H. Gobel, S. Christiansen, M. Albrecht, and H. P. Strunk, Philos. Mag. A **77**, 1013 (1998).

[142] V. Srikant, J. S. Speck, and D. R. Clarke, J. Appl. Phys. **82**, 4286 (1997).

[143] P. Gay, P. B. Hirsch, and A. Kelly, Acta Metall. **1**, 315 (1953).

[144] C. G. Dunn and E. F. Koch, Acta. Metall. **5**, 548 (1957).

[145] T. Gruber, G. M. Prinz, C. Kirchner, R. Kling, F. Reuss, W. Limmer, and A. Waag, J. Appl. Phys. **96**, 289 (2004).

[146] I. B. Kobiakov, Solid State Commun. **35**, 305 (1980).

[147] C. Kisielowski, J. Kruger, S. Ruvimov, T. Suski, J. W. Ager, E. Jones, Z. LilientalWeber, M. Rubin, E. R. Weber, M. D. Bremser, and R. F. Davis, Phys. Rev. B **54**, 17745 (1996).

[148] H. P. Sun, *Ph.D. Thesis*. (University of Michigan, Ann Arbor, 2005).

[149] M Mayer, *SIMNRA User's Guide 6.0*. (http://www.rzg.mpg.de/~mam/, Max-Planck-Institut für Plasmaphysik, Garching, Germany, 2008).

[150] L. J. van der Pauw, Philips Res. Repts. **13**, 1 (1958).

[151] *Hall effect measurements*. (http://www.eeel.nist.gov/812/hall.html, National Institute of Standards and Technology, 2005).

[152] E. H. Putley, *The Hall Effect and Related Phenomena*. (Butterworth & Co, 1960).

[153] L. J. van der Pauw, Philips Tech. Rev. **20**, 220 (1958).

[154] D. C. Look and R. J. Molnar, Appl. Phys. Lett. **70**, 3377 (1997).

[155] D. C. Look, *Electrical Characterization of GaAs Materials and Devices (Design and Measurement in Electronic Engineering)* (John Wiley & Sons, New Jersey, 1989), pp. 75-91, 115.

[156] D. C. Look, Semicond. Sci. Technol. **20**, S55 (2005).

[157] A. R. Hutson, J. Appl. Phys. **32**, 2287 (1961).

[158] C. Hammar and B. Magnusson, Phys. Scr. **6**, 206 (1972).

[159] K. Iwata, P. Fons, S. Niki, A. Yamada, K. Matsubara, K. Nakahara, and H. Takasu, Phys. Status Solidi A **180**, 287 (2000).

[160] Y. S. Jung, O. V. Kononenko, and W. K. Choi, Solid State Commun. **137**, 474 (2006).

[161] E. Conwell and V. F. Weisskopf, Phys. Rev. **77**, 388 (1950).

[162] X. C. Yang, C. C. Xu, and N. C. Giles, J. Appl. Phys. **104**, 073727 (2008).

[163] N. G. Weimann, L. F. Eastman, D. Doppalapudi, H. M. Ng, and T. D. Moustakas, J. Appl. Phys. **83**, 3656 (1998).

[164] D. C. Look and J. R. Sizelove, Phys. Rev. Lett. **82**, 1237 (1999).

[165] J. Tauc, Grigorov.R, and A. Vancu, Phys. Status Solidi **15**, 627 (1966).

[166] A. Teke, U. Ozgur, S. Dogan, X. Gu, H. Morkoc, B. Nemeth, J. Nause, and H. O. Everitt, Phys. Rev. B **70**, 195207 (2004).

[167] B. K. Meyer, H. Alves, D. M. Hofmann, W. Kriegseis, D. Forster, F. Bertram, J. Christen, A. Hoffmann, M. Strassburg, M. Dworzak, U. Haboeck, and A. V. Rodina, Phys. Status Solidi B **241**, 231 (2004).

[168] D. C. Reynolds, C. W. Litton, and T. C. Collins, Phys. Rev. **140**, 1726 (1965).

[169] C. A. Arguello, D. L. Rousseau, and S. P. S. Porto, Phys. Rev. **181**, 1351 (1969).

[170] A. Allenic, *Ph.D. Thesis*. (University of Michigan, Ann Arbor, 2008).

[171] C. P. Chen, M. Hong, J. Kwo, H. M. Cheng, Y. L. Huang, S. Y. Lin, J. Chi, H. Y. Lee, Y. F. Hsieh, and J. P. Mannaerts, J. Cryst. Growth **278**, 638 (2005).

[172] D. O. Klenov, L. F. Edge, D. G. Schlom, and S. Stemmer, Appl. Phys. Lett. **86**, 051901 (2005).

[173] H. Kiessig, Ann. Phys.-Berlin **10**, 769 (1931).

[174] C. Stampfl and C. G. Van de Walle, Phys. Rev. B **57**, R15052 (1998).

[175] D. Hull and D. J. Bacon, *Introduction to dislocations*. (Oxford, Boston, 2001), 107.

[176] K. Dovidenko, S. Oktyabrsky, and J. Narayan, J. Appl. Phys. **82**, 4296 (1997).

[177] H. P. Sun, X. Q. Pan, X. L. Du, Z. X. Mei, Z. Q. Zeng, and Q. K. Xue, Appl. Phys. Lett. **85**, 4385 (2004).

[178] D. Gerthsen, D. Litvinov, T. Gruber, C. Kirchner, and A. Waag, Appl. Phys. Lett. **81**, 3972 (2002).

[179] A. F. Kohan, G. Ceder, D. Morgan, and C. G. Van de Walle, Phys. Rev. B **61**, 15019 (2000).

[180] D. B. Basler and M. F. Berard, J. Am. Ceram. Soc. **57**, 447 (1974).

[181] O. I. Get'man, V. V. Panichkina, and V. V. Skorokhod, Powder Metall. Met. Ceram. **43**, 236 (2004).

[182] H. Sasaki, S. Kato, T. Matsuda, Y. Sato, M. Iwami, and S. Yoshida, Jpn. J. Appl. Phys. **45**, 2531 (2006).

[183] M. S. Hu, M. D. Thouless, and A. G. Evans, Acta. Metall. **36**, 1301 (1988).

[184] L. N. Demyanets, N. L. Sizova, and L. E. Li, Crystallogr. Rep. **50**, 698 (2005).

[185] A. K. Mukhopadhyay, M. R. Chaudhuri, A. Seal, S. K. Dalui, M. Banerjee, and K. K. Phani, Bull. Mat. Sci. **24**, 125 (2001).

[186] E. M. Kaidashev, M. Lorenz, H. von Wenckstern, A. Rahm, H. C. Semmelhack, K. H. Han, G. Benndorf, C. Bundesmann, H. Hochmuth, and M. Grundmann, Appl. Phys. Lett. **82**, 3901 (2003).

[187] H. Kato, M. Sano, K. Miyamoto, and T. Yao, Jpn. J. Appl. Phys. **42**, 2241 (2003).

[188] D. C. Look, J. W. Hemsky, and J. R. Sizelove, Phys. Rev. Lett. **82**, 2552 (1999).

[189] B. K. Meyer, S. Lautenschlager, S. Graubner, C. Neumann, and J. Sann, Mater. Res. Soc. Symp. Proc. **891**, 339 (2006).

[190] A. Janotti and C. G. Van de Walle, Appl. Phys. Lett. **87**, 122102 (2005).

[191] D. C. Look, Mater. Sci. Eng. B-Solid State Mater. Adv. Technol. **50**, 50 (1997).

[192] M. W. Allen, P. Miller, J. B. Metson, R. J. Reeves, M. M. Alkaisi, and S. M. Durbin, Mater. Res. Soc. Symp. Proc. **957**, 149 (2007).

[193] W. Cai, S. E. Stone, J. P. Pelz, L. F. Edge, and D. G. Schlom, Appl. Phys. Lett. **91**, 042901 (2007).

[194] S. J. Pearton, C. R. Abernathy, and F. Ren, *Gallium nitride processing for electronics, sensors and spintronics*. (Springer, London, 2006), P317.

[195] D. C. Look, H. L. Mosbacker, Y. M. Strzhemechny, and L. J. Brillson, Superlattices Microstruct. **38**, 406 (2005).

[196] T. Edahiro, N. Fujimura, and T. Ito, J. Appl. Phys. **93**, 7673 (2003).

[197] D. C. Reynolds, D. C. Look, B. Jogai, C. W. Litton, G. Cantwell, and W. C. Harsch, Phys. Rev. B **60**, 2340 (1999).

[198] D. C. Reynolds, D. C. Look, B. Jogai, and T. C. Collins, Appl. Phys. Lett. **79**, 3794 (2001).

[199] W. Siegel, G. Kuhnel, H. Koi, and W. Gerlach, Phys. Status Solidi A **95**, 309 (1986).

[200] D. C. Reynolds, D. C. Look, and B. Jogai, J. Appl. Phys. **88**, 5760 (2000).

[201] H. Teisseyre, P. Perlin, T. Suski, I. Grzegory, S. Porowski, J. Jun, A. Pietraszko, and T. D. Moustakas, J. Appl. Phys. **76**, 2429 (1994).

[202] V. Y. Davydov, N. S. Averkiev, I. N. Goncharuk, D. K. Nelson, I. P. Nikitina, A. S. Polkovnikov, A. N. Smirnov, M. A. Jacobsen, and O. K. Semchinova, J. Appl. Phys. **82**, 5097 (1997).

[203] B. Gil, Phys. Rev. B **64**, 201310 (2001).

[204] A. Tsukazaki, M. Kubota, A. Ohtomo, T. Onuma, K. Ohtani, H. Ohno, S. F. Chichibu, and M. Kawasaki, Jpn. J. Appl. Phys. **44**, L643 (2005).

[205] J. A. Dean, *Lange's handbook of chemistry*, 15th ed. (McGraw-Hill, New York, 1999), 92,100,111.

[206] T. Schleid and G. Meyer, J. Less-Common Met. **149**, 73 (1989).

[207] A. V. Shevchenko, L. M. Lopato, and I. E. Kiryakova, Inorg. Mater. **20**, 1731 (1984).

[208] L. Smrcok, Cryst. Res. Technol. **24**, 607 (1989).

[209] D. H. Templeton and C. H. Dauben, J. Am. Chem. Soc. **76**, 5237 (1954).

[210] S. Geller, P. Romo, and J. P. Remeika, Z. Kristallogr. **124**, 136 (1967).

[211] L. Marsella and V. Fiorentini, Phys. Rev. B **69**, 172103 (2004).

[212] A. M. Pires, M. R. Davolos, C. O. Paiva-Santos, E. B. Stucchi, and J. Flor, J. Solid State Chem. **171**, 420 (2003).

[213] S. J. Hearne, J. Han, S. R. Lee, J. A. Floro, D. M. Follstaedt, E. Chason, and I. S. T. Tsong, Appl. Phys. Lett. **76**, 1534 (2000).

[214] H. Amano, M. Iwaya, T. Kashima, M. Katsuragawa, I. Akasaki, J. Han, S. Hearne, J. A. Floro, E. Chason, and J. Figiel, Jpn. J. Appl. Phys. **37**, 1540 (1998).

[215] M. Iwaya, T. Takeuchi, S. Yamaguchi, C. Wetzel, H. Amano, and I. Akasaki, Jpn. J. Appl. Phys. Part 2 - Lett. **37**, L316 (1998).

[216] J. Han, K. E. Waldrip, S. R. Lee, J. J. Figiel, S. J. Hearne, G. A. Petersen, and S. M. Myers, Appl. Phys. Lett. **78**, 67 (2001).

[217] Y. Yan and S. H. Wei, Phys. Status Solidi B **245**, 641 (2008).

[218] E. C. Lee, Y. S. Kim, Y. G. Jin, and K. J. Chang, Phys. Rev. B **64**, 85120 (2001).

[219] K. K. Kim, H. S. Kim, D. K. Hwang, J. H. Lim, and S. J. Park, Appl. Phys. Lett. **83**, 63 (2003).

[220] F. X. Xiu, Z. Yang, L. J. Mandalapu, J. L. Liu, and W. P. Beyermann, Appl. Phys. Lett. **88**, 52106 (2006).

[221] A. Allenic, W. Guo, Y. Chen, M. B. Katz, G. Y. Zhao, Y. Che, Z. D. Hu, B. Liu, S. B. Zhang, and X. Q. Pan, Adv. Mater. **19**, 3333 (2007).

[222] Y. R. Ryu, T. S. Lee, and H. W. White, Appl. Phys. Lett. **83**, 87 (2003).

[223] D. C. Look, G. M. Renlund, R. H. Burgener, and J. R. Sizelove, Appl. Phys. Lett. **85**, 5269 (2004).

[224] V. Vaithianathan, B. T. Lee, and S. S. Kim, Appl. Phys. Lett. **86**, 062101 (2005).

[225] T. Aoki, Y. Shimizu, A. Miyake, A. Nakamura, Y. Nakanishi, and Y. Hatanaka, Phys. Status Solidi B **229**, 911 (2002).

[226] L. J. Mandalapu, Z. Yang, F. X. Xiu, D. T. Zhao, and J. L. Liu, Appl. Phys. Lett. **88**, 092103 (2006).

[227] F. X. Xiu, Z. Yang, L. J. Mandalapu, D. T. Zhao, J. L. Liu, and W. P. Beyermann, Appl. Phys. Lett. **87**, 152101 (2005).

[228] W. Guo, A. Allenic, Y. B. Chen, X. Q. Pan, Y. Che, Z. D. Hu, and B. Liu, Appl. Phys. Lett. **90**, 242108 (2007).

[229] S. Limpijumnong, S. B. Zhang, S. H. Wei, and C. H. Park, Phys. Rev. Lett. **92**, 155504 (2004).

[230] J. A. Roger, M. G. Blanchin, B. Canut, V. S. Teodorescu, S. Letant, and J. C. Vial, Semicond. Sci. Technol. **14**, L29 (1999).

[231] S. Choopun, R. D. Vispute, W. Noch, A. Balsamo, R. P. Sharma, T. Venkatesan, A. Iliadis, and D. C. Look, Appl. Phys. Lett. **75**, 3947 (1999).

[232] Y. R. Ryu, S. Zhu, D. C. Look, J. M. Wrobel, H. M. Jeong, and H. W. White, J. Cryst. Growth **216**, 330 (2000).

[233] B. Claflin, D. C. Look, S. J. Park, and G. Cantwell, J. Cryst. Growth **287**, 16 (2006).

[234] B. Pödör, Proc. SPIE **4412**, 299 (2001).

[235] F. X. Xiu, Z. Yang, L. J. Mandalapu, D. T. Zhao, and J. L. Liu, Appl. Phys. Lett. **87**, 252102 (2005).